**University of Alberta**

# Fabrication and Characterization of ZnO Thin Films

by

Piotr Kursa

A thesis submitted to the Faculty of Graduate Studies and Research
in partial fulfillment of the requirements for the degree of

Master of Science

Department of Electrical and Computer Engineering

Edmonton, Alberta
Fall, 2007

Reproduced with permission of the copyright owner. Further reproduction prohibited without permission.

Library and Archives Canada

Published Heritage Branch

395 Wellington Street
Ottawa ON K1A 0N4
Canada

Bibliothèque et Archives Canada

Direction du Patrimoine de l'édition

395, rue Wellington
Ottawa ON K1A 0N4
Canada

*Your file Votre référence*
*ISBN: 978-0-494-33287-0*
*Our file Notre référence*
*ISBN: 978-0-494-33287-0*

NOTICE:
The author has granted a non-exclusive license allowing Library and Archives Canada to reproduce, publish, archive, preserve, conserve, communicate to the public by telecommunication or on the Internet, loan, distribute and sell theses worldwide, for commercial or non-commercial purposes, in microform, paper, electronic and/or any other formats.

AVIS:
L'auteur a accordé une licence non exclusive permettant à la Bibliothèque et Archives Canada de reproduire, publier, archiver, sauvegarder, conserver, transmettre au public par télécommunication ou par l'Internet, prêter, distribuer et vendre des thèses partout dans le monde, à des fins commerciales ou autres, sur support microforme, papier, électronique et/ou autres formats.

The author retains copyright ownership and moral rights in this thesis. Neither the thesis nor substantial extracts from it may be printed or otherwise reproduced without the author's permission.

L'auteur conserve la propriété du droit d'auteur et des droits moraux qui protège cette thèse. Ni la thèse ni des extraits substantiels de celle-ci ne doivent être imprimés ou autrement reproduits sans son autorisation.

In compliance with the Canadian Privacy Act some supporting forms may have been removed from this thesis.

Conformément à la loi canadienne sur la protection de la vie privée, quelques formulaires secondaires ont été enlevés de cette thèse.

While these forms may be included in the document page count, their removal does not represent any loss of content from the thesis.

Bien que ces formulaires aient inclus dans la pagination, il n'y aura aucun contenu manquant.

Reproduced with permission of the copyright owner. Further reproduction prohibited without permission.

*To my family*

Reproduced with permission of the copyright owner. Further reproduction prohibited without permission.

# *Abstract*

In this thesis work, ZnO thin films were deposited using pulsed laser deposition and sol-gel methods and their optical and luminescence properties were characterized. Pulsed laser deposited films were realized using a 15 ns pulse krypton fluoride laser operating at 248 nm. Sol-gel films were fabricated using sol consisting of polyvinyl alcohol, zinc acetate dihydrate and distilled water spun at 1000 rpm for 10 minutes per layer. Films in both methods were deposited on fused silica, silicon, Si/$SiO_2$, and Si/ZnO substrates. Single layer films of thicknesses ranging from 100 nm to 250 nm were produced, and they exhibited a characteristic photoluminescence peak of 390 nm for annealed films. The effects of annealing method, various substrates, single and multiple layer depositions, and different sol constituent concentrations on the optical characteristics of the films, thickness, surface morphology, and room temperature photoluminescence emission spectra were studied.

Reproduced with permission of the copyright owner. Further reproduction prohibited without permission.

# *Acknowledgment*

I would like to thank Dr. Ray DeCorby and Dr. Ying Ying Tsui for their help and support in completing this thesis. I want to express my gratitude to Hue Nguyen for the countless hours she spent with me in the NanoFab. I want to thank all of my colleagues and peers at TRLabs for their help and friendship.

Reproduced with permission of the copyright owner. Further reproduction prohibited without permission.

CHAPTER 1 *Introduction* **1**

Motivation **1**
ZnO material properties and applications **1**
Deposition techniques **4**
Outline of this thesis **6**

CHAPTER 2 *Background and Theory* *7*

Piezoelectric effect and SAW devices **7**
Photoelastic effect **20**
Thin film characterization methods. **23**
*2.3.1 Variable angle spectroscopic ellipsometry* ***23***
*2.3.2 Scanning electron microscope (SEM)* ***24***
*2.3.3 Electron microprobe analysis* ***25***
*2.3.4 Room temperature photoluminescence* ***26***
*2.3.5 Prism coupler measurements.* ***28***

CHAPTER 3 *ZnO Films by PLD* ***30***

Background on PLD technique **30**
*3.1.1 Equipment* ***31***
*3.1.2 Thin Film Nucleation and Growth* ***35***
*2.2.3 Background Gases* ***38***
Pulsed Laser Deposition Setup **40**
*3.1.1 Energy and plasma monitoring* ***42***
PLD films on quartz. **45**
PLD films on silicon **48**

CHAPTER 4 *ZnO Films by Sol-gel* ***59***

Background on Sol-gel **59**
ZnO films deposited using sol-gel method. **63**

CHAPTER 5 *Summary, Conclusion, and Future Work* ***81***

References ***84***

Reproduced with permission of the copyright owner. Further reproduction prohibited without permission.

*List of Tables*

**Table 1.1** Properties of wurtzite ZnO[9]. 4
**Table 2.1** Design parameters for SAW filter on quartz substrate. 15
**Table 3.1** Excimer laser types and their corresponding wavelengths[45]. 33
**Table 3.2** Transmittance ranges for various lens and window materials[44]. 34
**Table 3.3** Summary of PLD films deposited on Si substrates. * See discussion below. 49
**Table 4.1** Commonly used ligands for sol-gel synthesis. Dot indicates bonding site, parenthesis indicate atom with available bond, n indicates linear chain, sec - secondary, tert - tertiary[54]. 61
**Table 4.2** Summary of sol-gel deposited. '1' in "Sol" column refers to the 'standard' ratio of PVA and zinc acetate dihydrate used as per Zhang et al., '2' to double ratios of PVA and zinc acetate dihydrate while keeping amount of distilled water the same as in '1'. '3' refers to recipes where amount of PVA in the solution was adjusted to reflect the fact that PVA used for work in this thesis was of higher molecular weight than that used by Zhang et al.[56] '4' refers to even further reduction of PVA concentration as per suggestions from Dr. Zhang. Under column "Annealed Between Sol Spins" and "Final Annealed", hot plate refers to annealing done on the same hot plate as drying in between layer applications, furnace to the air furnace that was used to anneal PLD films. 64

Reproduced with permission of the copyright owner. Further reproduction prohibited without permission.

# *List of Figures*

**Fig. 1.1** Room temperature band diagram for ZnO, a direct bandgap semiconductor[8]. 2
**Fig. 1.2** Wurtzite structure of ZnO[8]. 3
**Fig. 1.3** Planar RF sputtering system for ZnO deposition[14]. 5
**Fig. 2.1** Rayleigh wave[18]. 9
**Fig. 2.2** Love wave[18]. 9
**Fig. 2.3** SAW filter utilizing IDTs as input and output transducers[19]. 10
**Fig. 2.4** Experimental setup for measuring electromechanical coupling coefficient by measuring SAW velocities with and without a highly conductive metal film. Ex, Ey are the components fo electric field parallel to the surface, and is the electric potential at the (ground) surface metal film[20]. 11
**Fig. 2.5** SAW delay line showing configuration of an IDT[21]. 12
**Fig. 2.6** Parallel (a) and series (b) equivalent circuits for an interdigital transducer [21] 13
**Fig. 2.7** Lift-off process visualization[31]. 16
**Fig. 2.8** An IDT visible under 100X magnification. 16
**Fig. 2.9** Microwave station setup using Picoprobe microwave probes. 17
**Fig. 2.10** Frequency response of a SAW IDT filter on a quartz substrate. 18
**Fig. 2.11** Matching network for 400MHz quartz filter. 18
**Fig. 2.12** Frequency response of a 400MHz commercially available SAW filter. 19
**Fig. 2.13** An SEM image of an IDT transducer. 20
**Fig. 2.14** Guided wave control by acoustooptic Bragg diffraction. is the incident wave vector and is the deflected wave vector[35]. 22
**Fig. 2.15** Schematic of geometry of an ellipsometry experiment[37]. 24
**Fig. 2.16** Thin film model. SiO2_jaw is the fused silica wafer substrate, cauchy represents the thin film grown, and srough is the surface roughness represented as 50% air void due to surface roughness and film porosity[39]. 24
**Fig. 2.17** SEM images of ZnO on GaN. (a) top view, (b) 60 degree tilt, (c) side view[8]. 25
**Fig. 2.18** Photoluminescence measurement setup[8]. 26
**Fig. 2.19** Photoluminescence signal raw data. 27
**Fig. 2.20** Post-processed photoluminescence signals. 28

Reproduced with permission of the copyright owner. Further reproduction prohibited without permission.

**Fig. 2.21** Metricon 2010 prism coupler measurement setup[43]. 29
**Fig. 2.22** Intensity of reflected light vs angle of incidence[43]. 29
**Fig. 3.1** Schematic of a basic PLD setup[44]. 32
**Fig. 3.2** Beam profile of a 248 nm Atlex laser[46]. 33
**Fig. 3.3** First four stages of island formation. Clockwise from top left; (1) nucleation, (2) nuclei growth, (3) island formation, and (4) coalescence[48]. 36
**Fig. 3.4** Diagram illustrating nucleus formation and shadowing effect[8]. 37
**Fig. 3.5** Movchan-Demchishim structure zone model of thin film growth based on substrate temperature[49]. 38
**Fig. 3.6** Plasma plume observed in 100mTorr of [8]. 39
**Fig. 3.7** Plasma plume observed in vacuum[8]. 39
**Fig. 3.8** PLD setup during deposition 41
**Fig. 3.9** PLD stage setup with Langmuir probe for plasma plume characterization. 41
**Fig. 3.10** Energy parameter measurement setup 42
**Fig. 3.11** Typical Langmuir probe signature at the beginning of a deposition run with 100 mTorr oxygen background. 43
**Fig. 3.12** Typical Langmuir probe reading at the end of the deposition run with 100 mTorr oxygen background. This particular run yielded 91,200 shots in 76 minutes. 44
**Fig. 3.13** Langmuir probe signal corresponding to low oxygen pressure in the chamber. 44
**Fig. 3.14** Plume position on the holder with respect to the substrates. 46
**Fig. 3.15** Fit of model to experimental values of . Note that the model agrees very well with the fit past 300 nm (they are on top of each other). 47
**Fig. 3.16** Experimentally extracted results for of n and k of a ZnO film on fused silica. 47
**Fig. 3.17** Comparison of experimentally obtained values of n with those calculated using dispersion formulas shown in Eq. 3.1 and Eq. 3.2.[50] 48
**Fig. 3.18** Plume is centered on the sample. 49
**Fig. 3.19** Side SEM image of PLD 1-1 on the thicker side of the sample. 50
**Fig. 3.20** Side SEM image of PLD 1-1 on thinner side of the sample. 51
**Fig. 3.21** Angle SEM image of PLD 1-1 showing crystal sizes on the order of 60 nm. 51
**Fig. 3.22** Side SEM image of PLD 1-2. 52
**Fig. 3.23** Top SEM image of PLD 1-2. Crystal sizes in this sample were on the order of 20-30 nm. 52
**Fig. 3.24** Side SEM image of PLD 3. 54
**Fig. 3.25** Angle SEM image of PLD 3 surface. 54
**Fig. 3.26** Side SEM image of PLD 4. 55
**Fig. 3.27** Top SEM image of PLD 4 surface. 55
**Fig. 3.28** Room temperature PL spectrum of PLD 3. 56
**Fig. 3.29** RT PL spectrum of PLD 4. 56
**Fig. 3.30** RT PL spectrum of PLD 5. 57
**Fig. 3.31** RT PL spectrum of another portion of PLD 5 sample. 57
**Fig. 3.32** Depiction of the effects of film defects on RT PL spectrum. 58
**Fig. 4.1** Typical schematic illustration of ZnO crystal growth in thinner and thicker coating films[11]. 62
**Fig. 4.2** Edge SEM of sol-gel 1. 65
**Fig. 4.3** Edge SEM of sol-gel 2. 65
**Fig. 4.4** Angle SEM image of sol-gel 2. 66

Reproduced with permission of the copyright owner. Further reproduction prohibited without permission.

**Fig. 4.5** RT PL spectrum of sol-gel 2 with very distinct peak at about 390 nm. 66
**Fig. 4.6** Edge SEM image of sol-gel 4 sample annealed in a furnace. 68
**Fig. 4.7** Edge SEM image of sol-gel 5 sample annealed in a furnace. 69
**Fig. 4.8** RT PL spectrum for sol-gel 4-2. 69
**Fig. 4.9** RT PL spectrum of sol-gel 5-2. 70
**Fig. 4.10** RT PL spectrum of sol-gel 4-1 with visible additional luminescence peaks. 70
**Fig. 4.11** Edge SEM image of sol-gel 6-1. 72
**Fig. 4.12** Edge SEM image of sol-gel 6-2 with distinct boundary between the two layers associated with the 2 sol spinning steps. 72
**Fig. 4.13** RT PL spectrum of sol-gel 6-1. 73
**Fig. 4.14** Edge SEM image of PLD 6-1. 74
**Fig. 4.15** Top SEM surface image of PLD 6-1. 74
**Fig. 4.16** RT PL spectrum of PLD 6-1. 75
**Fig. 4.17** Edge SEM image of sol-gel 7-2. 77
**Fig. 4.18** Top SEM image of the surface of sol-gel 7-2. 77
**Fig. 4.19** RT PL spectrum of sol-gel 7-2. 78
**Fig. 4.20** Edge SEM image of sol-gel 8. 79
**Fig. 4.21** Surface SEM image of sol-gel 8. 79
**Fig. 4.22** RT PL spectrum of sol-gel 8. 80

Reproduced with permission of the copyright owner. Further reproduction prohibited without permission.

*List of Symbols*

$\lambda$
Wavelength

$\upsilon$
Acoustic phase velocity

$\varepsilon$
Permittivity

$\Phi$
Electric potential

$\eta$
Optical impermeability

$\rho$
Density

$\Psi$
Real part of a reflection angle

$\Delta$
Imaginary part of a reflection angle

$\mathbf{A}$
Area

$\mathbf{a_o}$
Lattice constant

$\mathbf{B_a}$
Susceptance

$\mathbf{c}$
Elastic Stiffness Coefficient

$\mathbf{C_o}$
Static capacitance per unit length of interdigital transducer

$\mathbf{c_o}$
Lattice constant

Reproduced with permission of the copyright owner. Further reproduction prohibited without permission.

**$C_s$**

Static capacitance per section of interdigital transducer

**e**

Piezoelectric constant

**E**

Electric field

**$E_g$**

Band gap energy

**f**

Frequency

**$G_a$**

Conductance

**k, k'**

Elliptic integral moduli with mutual dependence

**K, K'**

Elliptic integral coefficients

**$k^2$**

Electromechanical coupling coefficient

**L**

Section of interdigital transducer equal to one wavelength

**M, $M_2$**

Acousto-optic figure of merit

**n**

Index of refraction

**N**

Number of sections in interdigital transducer

**p**

Photoelastic coefficient

**P**

Power of an acoustic wave

**$p_{ijkl}$**

Strain-optic tensor

**$R_a$**

Resistance

**$R_p$**

Fresnel reflection coefficient

**$R_s$**

Fresnel reflection coefficient

**S**

Strain

**W**

Width of transducer

Reproduced with permission of the copyright owner. Further reproduction prohibited without permission.

## *List of Abbreviations*

**EMPA**
Electron Microprobe Analysis

**IDT**
Interdigital Transducer

**MEA**
Methoxyethanol-monoethanolamine

**MOCVD**
Metal-organic Chemical Vapour Deposition

**PCB**
Printed Circuit Board

**PLD**
Pulsed Laser Deposition

**PVA**
Polyvinyl Alcohol

**RF**
Radio Frequency

**RT PL**
Room Temperature Photoluminescence

**SAW**
Surface Acoustic Wave

**SEM**
Scanning Electron Microscope

**SH**
Shear Horizontal

**UV**
Ultraviolet

**VASE**
Variable Angle Spectroscopic Ellipsometry

Reproduced with permission of the copyright owner. Further reproduction prohibited without permission.

**ZAD**

Zinc Acetate Dihydrate

Reproduced with permission of the copyright owner. Further reproduction prohibited without permission.

CHAPTER 1

# Introduction

## 1.1. Motivation

The motivation for this thesis work was the production, characterization, and comparison of ZnO thin films by pulsed laser deposition (PLD) and sol-gel techniques. Thin films were characterized mainly for their optical properties. This in turn was motivated by the interesting acousto-optical properties of ZnO thin films.

## 1.2. ZnO material properties and applications

Zinc oxide is a direct gap, II-IV semiconductor with a bandgap $E_g = 3.37$ eV as illustrated in Fig. 1.1. The bandgap is tunable by doping. For example, Cd doping can reduce the gap to about 3eV and addition of Mg can increase $E_g$ to about 4eV[1]. ZnO is a very attractive material as applications to UV light emitters[2], solar cells[3], piezoelectric transducers[4], gas sensors[5], transparent electronics[6], waveguides[7], and surface acoustic wave (SAW) devices[8,9,10].



Reproduced with permission of the copyright owner. Further reproduction prohibited without permission.

ZnO normally forms a hexagonal or wurtzite crystal structure as illustrated in Fig. 1.2, with lattice constants $a = 3.25\text{Å}$, and $c = 5.12\text{Å}$. The Zn atoms are tetrahedrally coordinated with four oxygen atoms. Zn d-electrons hybridize with O p-electrons forming predominantly covalent bonding with significant contribution from ionic bonding. Layers of zinc atoms alternate with layers occupied by oxygen atoms. Room temperature UV luminescence of photons with nearly bandgap energy is attributed largely to an exciton state that has a binding energy of 60 meV. Emission centered around 500 nm involves self-activated centers formed by doubly ionized zinc vacancies and ionized interstitial $Zn^+$, donor-acceptor pair recombination that involves impurity acceptor, oxygen vacancies, and interstitial oxygen. Broad orange-red band photoluminescence observed at about 1.9eV has been observed and is also attributed to defect states.

The electron Hall mobility of ZnO is around 200 $cm^2/V/s$ at room temperature and is slightly lower than that of GaN, its main competitor as a wide bandgap UV emitting semiconductor. Advantages of ZnO over GaN include availability of ZnO in bulk, single crystal form, and its larger exciton binding energy, which is an energy that is needed to take apart the bound state of an electron and an electron hole. ZnO is also lattice matched to InGaN at an In composition of about 22%, making the integration of those two materials possible, and providing the potential for on-chip integration[9].

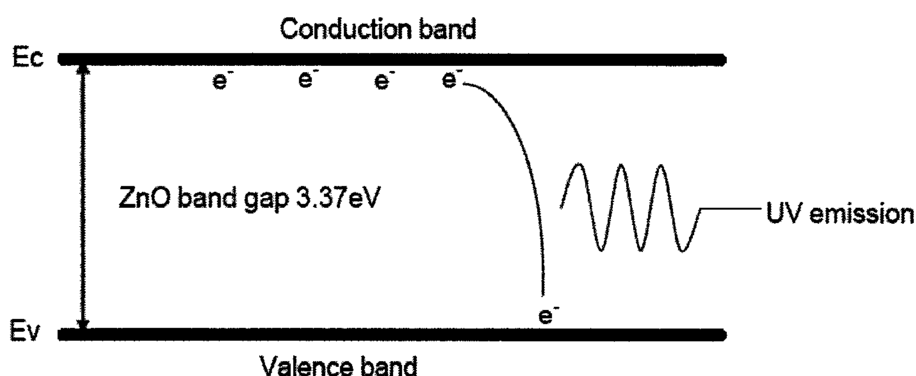


**Figure 1.1.** Room temperature band diagram for ZnO, a direct bandgap semiconductor[8].



Reproduced with permission of the copyright owner. Further reproduction prohibited without permission.

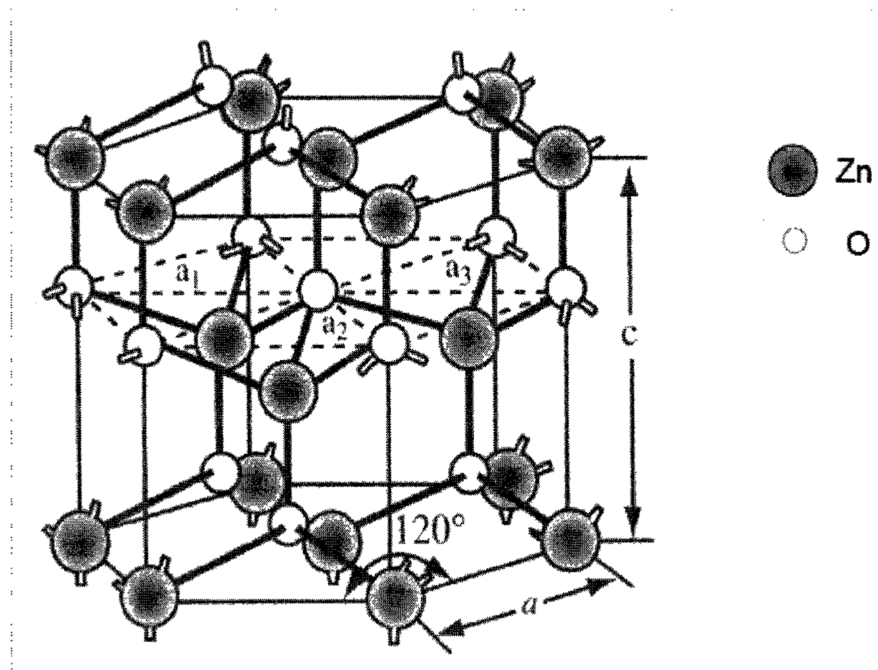


**Figure 1.2.** Wurtzite structure of ZnO[8].

In Rayleigh mode surface acoustic wave (SAW) devices, ST-cut quartz is the best temperature stabilized material[11]. However, its usefulness is limited by a relatively low electromechanical coupling coefficient. On the other hand, $LiNbO_3$ has much higher electromechanical coupling coefficient, but its temperature stability is very poor. ZnO is an excellent candidate for piezoelectric applications with high electromechanical coupling coefficient and good temperature stability compared to quartz and $LiNbO_3$ respectively[11].

The natural crystalline form of ZnO is very rare and is known as zincite[12]. ZnO is insoluble in water, but dissolves in many alkalis and acids, and in its crystalline form it exhibits piezoelectric and thermochromic (change of color when heated) effects[13]. The thermochromic effect in ZnO comes from various lattice defects that are created when the material is heated[9]. A list of some other properties of ZnO is given in Table 1.1[1].



Reproduced with permission of the copyright owner. Further reproduction prohibited without permission.

| Property | Value |
|---|---|
| Lattice parameters at 300 K | |
| $a_0$ | 0.324 95 nm |
| $c_0$ | 0.520 69 nm |
| $a_0/c_0$ | 1.602 (ideal hexagonal structure shows 1.633) |
| Density | 5.606 g cm$^{-3}$ |
| Stable phase at 300 K | Wurtzite |
| Melting point | 1975 °C |
| Thermal conductivity | 0.6, 1–1.2 |
| Linear expansion coefficient (/C) | $a_0$: 6.5 × 10$^{-6}$ |
| | $c_0$: 3.0 × 10$^{-6}$ |
| Static dielectric constant | 8.656 |
| Refractive index | 2.008, 2.029 |
| Energy gap | 3.4 eV, direct |
| Intrinsic carrier concentration | <10$^{6}$ cm$^{-3}$ |
| Exciton binding energy | 60 meV |
| Electron effective mass | 0.24 |
| Electron Hall mobility at 300 K for low n-type conductivity | 200 cm$^2$ V$^{-1}$ s$^{-1}$ |
| Hole effective mass | 0.59 |
| Hole Hall mobility at 300 K for low p-type conductivity | 5–50 cm$^2$ V$^{-1}$ s$^{-1}$ |

**Table 1.1.** Properties of wurtzite ZnO[9].

## *1.3. Deposition techniques*

PLD and sol-gel have been explored in this thesis work as candidates for thin film deposition methods. PLD was performed using a 248 nm wavelength KrF laser and it will be discussed in more detail in Chapter 3. Sol-gel depositions were explored using sols prepared using different concentrations of zinc acetate dihydrate, polyvinyl alcohol, and distilled water. An in-depth discussion of sol-gel deposition method will be provided in Chapter 4.

Besides PLD and sol-gel, several other techniques have been used for the deposition of ZnO films. One of the most prominent is sputtering. RF sputtering systems are the most commonly used for the deposition of polycrystalline ZnO thin films[14]. A typical sputtering system is shown in Fig. 1.3. Polycrystalline ZnO films of (001) orientation (c-axis is normal to the film surface) can be deposited on a glass surface from a Zn metal target in Ar and $O_2$ atmosphere. The c-axis oriented films are used in the making of thin film



Reproduced with permission of the copyright owner. Further reproduction prohibited without permission.

SAW devices. It should be noted that the crystallographic and piezoelectric properties of films obtained using this method can be influenced by the sputtering parameters like deposition rate, substrate temperature, film thickness, target chemical composition, target configuration, sputtering gas composition, sputtering gas pressure, and substrate position [14].

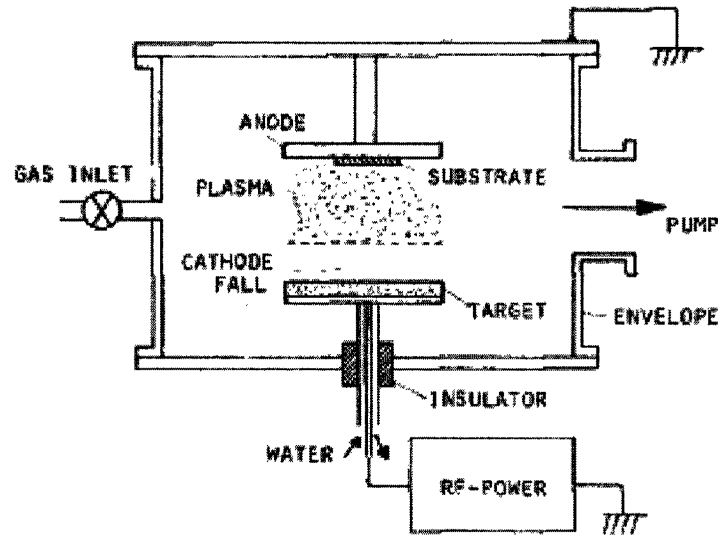


**Figure 1.3.** Planar RF sputtering system for ZnO deposition[14].

Another attractive method of ZnO thin film deposition is metalorganic chemical vapour deposition or MOCVD. This is a very popular method of growing compound semiconductors from surface reactions of metalorganics and metal hydrides that contain the required chemical elements. The formation of the epitaxial layer occurs by final pyrolysis of the chemicals that constitute the compound at the substrate surface[15].

The typical chemical reaction for the deposition of ZnO is:

$$Zn(CH_3COO)_2(g) + H_2O(g) \rightarrow ZnO(s) + 2CH_3COOH(g) \text{ [16]}. \quad \text{(EQ 1.1)}$$



Reproduced with permission of the copyright owner. Further reproduction prohibited without permission.

## *1.4. Outline of this thesis*

This thesis is divided into five chapters. Chapter 1 provides an introduction to the properties of zinc oxide and some discussion of alternate deposition methods. Chapter 2 describes piezoelectric, acoustooptic, and photoelastic effects and their applications in ZnO thin films. Work done on designing a SAW filter will also be presented in Chapter 2. In Chapter 3, background information and experimental results on the PLD method are presented and discussed. Chapter 4 is devoted to discussion of the sol-gel deposition method and films obtained using this method. Chapter 5 concludes this thesis with a summary of work completed and suggestions for future work.



Reproduced with permission of the copyright owner. Further reproduction prohibited without permission.

# CHAPTER 2 *Background and Theory*

The purpose of this chapter is to provide a brief introduction into the background theory on piezoelectric effects, SAW devices, and photoelastic effects. Utilization of SAW devices to aid acoustooptic interactions in the material for the purpose of acoustooptic device applications as well as initial design and implementation using quartz substrate is also discussed. The last part of this chapter will provide some insight into the methods used in characterizing thin films produced by PLD and sol-gel.

## *2.1. Piezoelectric effect and SAW devices*

SAW devices are an inexpensive, rugged, and versatile solution for sensing. They can be used for differentiating changes in physical and chemical parameters of an adjacent medium, such as mass, strain, liquid density, viscosity, permittivity, and conductivity. The anisotropic nature of piezoelectric crystals permits various angles of cuts, each with different properties. The detection mechanism depends upon the transduction of a SAW device; i.e. conversion of a mechanical signal such as waves in solids to electrical signals. A particularly useful characteristic of SAW devices is that a relatively small change in mechan-



Reproduced with permission of the copyright owner. Further reproduction prohibited without permission.

ical properties brings about a large change in the electromagnetic domain[17]. In other words, SAW devices can be highly sensitive.

A simple explanation of the piezoelectric effect is that when certain non-conducting crystalline materials come under external stress, the atoms in their crystal lattice are displaced such that electrical dipoles are induced within the crystal. In piezoelectric materials, these dipoles combine and produce a net macroscopic electrical polarization. This effect is always accompanied by its inverse, i.e. when the same material is polarized by an external electric field, it will become strained. These two effects are known as the direct piezoelectric and the inverse piezoelectric effects, respectively. A SAW transducer can be used to convert a strain wave of some frequency to an electrical signal of the same frequency. This signal can be transmitted over some distance by conventional means and then converted back to a strain (mechanical) wave by another transducer[17].

There are a number of possibilities when it comes to generating acoustic waves. The type of wave that will be generated depends on the substrate material properties, the crystal cut, and the structure of electrodes that are used to generate the SAW. The most common types of waves that are used in sensors and devices are the Rayleigh and shear horizontal (SH) surface acoustic wave, and the Love wave mode[17].

SAWs were first described by Lord Rayleigh, and so-called Rayleigh waves are the most used type of SAWs. The propagation of a Rayleigh wave is analogous to the propagation of ripples caused by a disturbance of calm water. A representation of a Rayleigh wave is shown in Fig. 2.1. Rayleigh wave motion produces particle displacement in an elliptical pattern, with one component in the direction normal to the surface and another parallel to the direction of wave propagation. The component normal to the surface is larger; this is intuitive since the crystal is more capable of moving in the unbound direction. Also illustrated in Fig. 2.1 is confinement of the energy of the wave to a surface region that is only a few acoustic wavelengths deep. This is somewhat analogous to the concept of electromagnetic skin depth (depth of penetration of electromagnetic wave into a conductor)[17].



Reproduced with permission of the copyright owner. Further reproduction prohibited without permission.

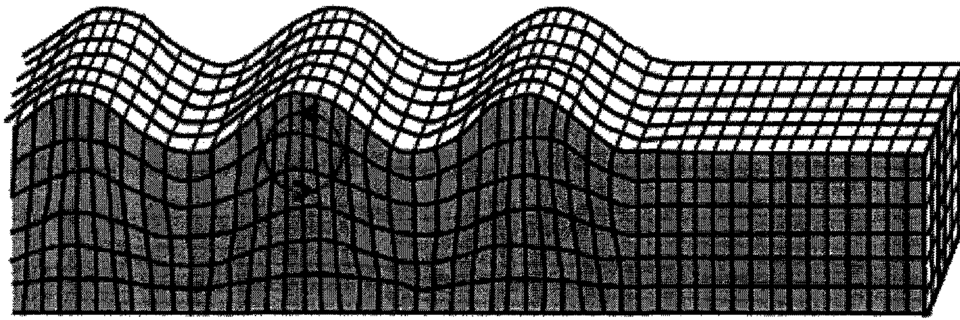

**Figure 2.1.** Rayleigh wave[18].

Another type of SAW is the so-called Love wave, which is shown in Fig. 2.2[17]. The plane of motion of this wave is perpendicular to that of a Rayleigh wave.

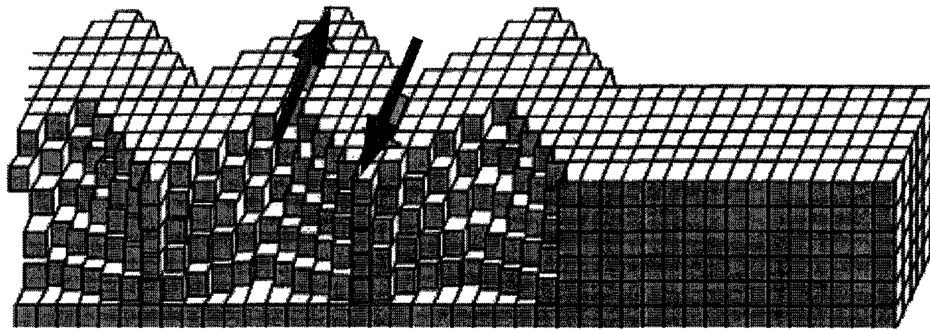

**Figure 2.2.** Love wave[18].

The simplest way of generating as well as transducing SAWs into electrical signals is through the use of an interdigital transducer (IDT). Fig. 2.3 illustrates a pair of IDTs on a piezoelectric substrate; the combination acts as a simple filter.



Reproduced with permission of the copyright owner. Further reproduction prohibited without permission.

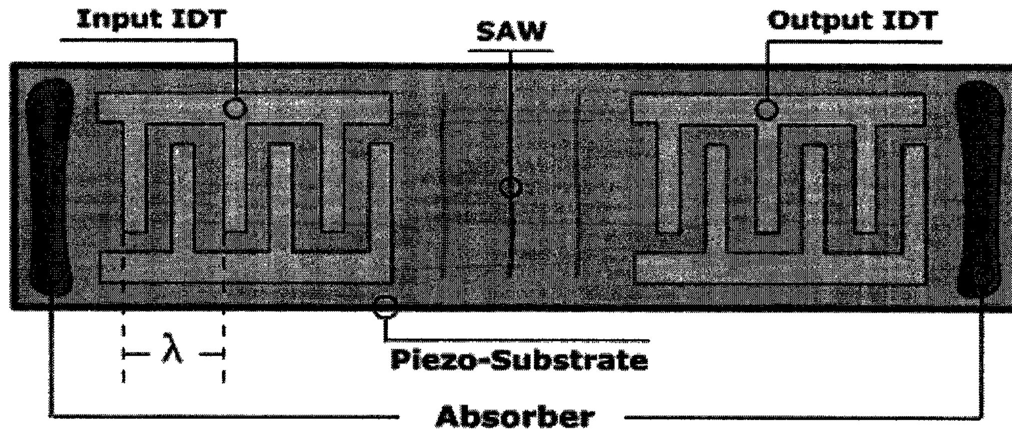


**Figure 2.3.** SAW filter utilizing IDTs as input and output transducers[19].

The spacing between the fingers is dictated by the wavelength of a SAW, $\lambda$, which is defined by:

$$\lambda = \frac{v_0}{f_0}, \qquad \text{(EQ 2.1)}$$

where $v_0$ is the SAW velocity of the free surface and $f_0$ is the frequency of the SAW as well as the centre frequency of the filter depicted in Fig. 2.3 [17].

The measure of conversion efficiency between electrical and mechanical energy is called the electromechanical coupling coefficient $k^2$. This value is usually small, and it is typically expressed as a percentage. It can be expressed as a relationship between piezoelectric constant, $e$, elastic stiffness coefficient, $c$, and permittivity, $\varepsilon$ of a given piezoelectric material, as follows:

$$k^2 = \frac{e^2}{c\varepsilon}. \qquad \text{(EQ 2.2)}$$

The piezoelectric constant, elastic stiffness coefficients, and permittivity are dependent on both crystal cut and the propagation direction of the surface acoustic wave. $k^2$ can also be obtained experimentally through the relationship[20]:



Reproduced with permission of the copyright owner. Further reproduction prohibited without permission.

$$k^2 = \frac{2|\Delta\upsilon|}{\nu},$$ (EQ 2.3)

where $|\Delta\upsilon|$ is the absolute difference in the surface acoustic wave velocities between the wave travelling on free piezoelectric surface and the wave travelling on the same surface covered by a highly conducting metallic film. The oscillating electric field associated with the SAW will cause the metal surface to accumulate charge. When the SAW circuit is modelled using a transmission line model, this charge accumulation will cause increase in capacitance, resulting in decrease in electromagnetic wave velocity. The experimental setup for measuring $k^2$ is shown in Fig. 2.4 below[20].

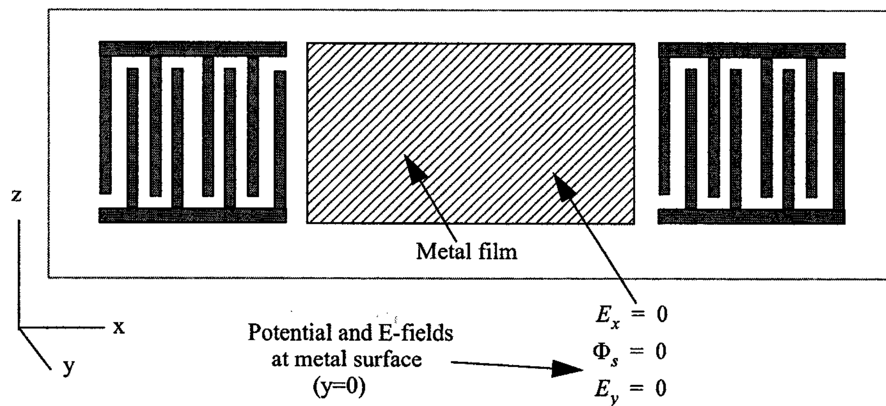


**Figure 2.4.** Experimental setup for measuring electromechanical coupling coefficient by measuring SAW velocities with and without a highly conductive metal film. $E_x$, $E_y$ are the components fo electric field parallel to the surface, and $\Phi_s$ is the electric potential at the (ground) surface metal film[20].

### 2.1.1 SAW Interdigital Transducer (IDT) Design

As stated before, depending on the direction of propagation, there can exist many different surface wave modes from Rayleigh, to SH, to Love mode in one single material. The following discussion on the design will make use of an assumption that only a single mode of propagation is involved by a proper choice of crystal cut[21].

The interdigital transducer is comprised of a series of interleaved electrodes made from a conductor that is deposited on top of a piezoelectric substrate as shown in Fig. 2.5



Reproduced with permission of the copyright owner. Further reproduction prohibited without permission.

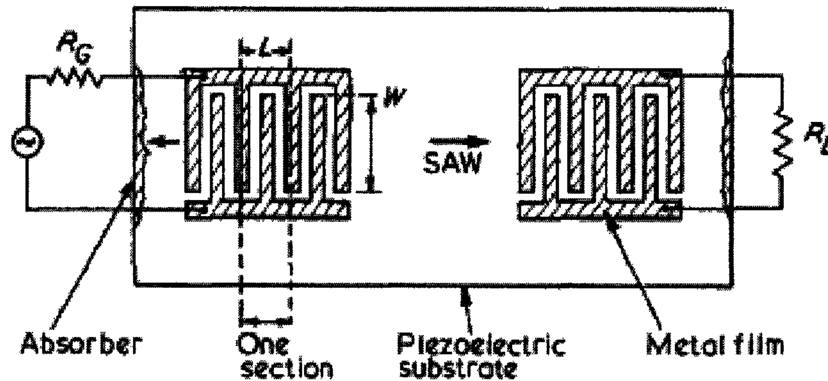


**Figure 2.5.** SAW delay line showing configuration of an IDT[21].

The width of an electrode is equal to the spacing between the electrodes and the wavelength of acoustic wave will be equal to *L*. The applied voltage will produce a stress pattern that will be launched in both directions from the transducer. The unwanted waves can be suppressed by the use of absorbers that are present on both ends of the structure. The output transducer will have an identical design as the input transducer. The effective width of the transducer is called an aperture (*W*)[21].

The exact behaviour of the anisotropic piezoelectric substrate is very complex; an approximate simplified theory considers the transducer as an array of sources, each being a piezoelectric plate transducer for launching bulk waves. This theory makes use of the cross-field model which assumes that the acoustic sources do not interact[22,23]. The transducer will have $2N+1$ number of electrodes or $N$ sections and each of the sections will be assigned an equivalent circuit in which the electromechanical coupling coefficient $k^2$ will be that for a surface wave particular to the chosen crystal cut. The equivalent circuit will be formed by cascading the individual sections. The parameters that are necessary for the complete design of an IDT are number of sections ($N$), frequency of an electrical signal ($f_o$)or wavelength of SAW wave ($\lambda$) which will determine the length of each of the sec-



Reproduced with permission of the copyright owner. Further reproduction prohibited without permission.

tions, the static capacity per section ($C_s$) or per finger per unit length ($C_o$), and the piezoelectric coupling coefficient ($k^2$).[21] Total capacity of the transducer ($C_T$) is given by:

$$C_T = NC_S = C_o(n-1)W, \quad \text{(EQ 2.4)}$$

where $N$ is the total number of fingers.

Piezoelectric coupling coefficient may be evaluated by measuring the velocities of SAW over a piezoelectric substrate and subsequently over the same substrate covered by a thin layer of highly conductive metallic film and then related by Eq. 2.3. The setup for this experiment is shown in Fig. 2.4[21]. For the most part, $k^2$ values that will be used in designing IDT transducers in later chapters were derived already by the manufacturers of wafers utilized by our group[24] and by other publications[25,26,27].

The equivalent circuit for the transducer can be represented as either series or parallel as shown in Fig. 2.6.

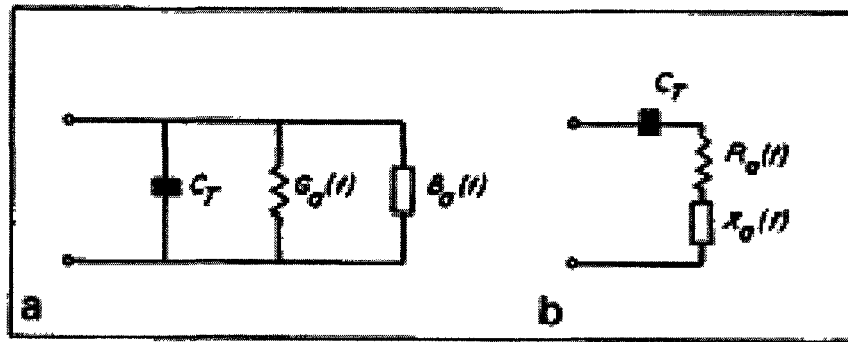


**Figure 2.6.** Parallel (a) and series (b) equivalent circuits for an interdigital transducer [21]

Using cross-field model and Hilbert transform[28], we can relate conductance $G_a(f)$ and susceptance $B_a(f)$. $G_a(f)$ has a maximum value at $f=f_o$ that can be calculated by using the relation:



Reproduced with permission of the copyright owner. Further reproduction prohibited without permission.

$$G_a = \widehat{G}_a\left(\frac{\sin x}{x}\right), \tag{EQ 2.5}$$

where

$$\widehat{G}_a = G_a(f_0) = \left(\frac{4k^2N}{\pi}\right)2\pi f_o C_T \tag{EQ 2.6}$$

and the resistance $R_a(f_o)$ is given by:

$$R_a(f_o) \approx \widehat{R}_a \equiv \frac{2k^2}{\pi^2 f_o C_S} = \frac{\widehat{G}_a}{(2\pi f_o C_T)} = \frac{2k^2 N}{\pi^2 f_o C_T} \tag{EQ 2.7}$$

In order to get a maximum power transfer out of the generator, $R_a(f_o)$ will be set to $50\Omega$. Combining Eq. 2.7 and Eq. 2.4, we can design transducer aperture, $W$ using[21]

$$W = \frac{k^2}{\pi^2 f_o C_o(50\Omega)}. \tag{EQ 2.8}$$

Number of sections, $N$, is picked for maximum bandwidth $\Delta f$ and is shown in:

$$N_{opt} \approx \frac{\sqrt{\pi}}{2k} \tag{EQ 2.9}$$

Capacitance between neighbouring electrodes, $C_o$, can be calculated using:

$$C_o = \frac{\varepsilon_o(1+\varepsilon_r)K}{K'}, \tag{EQ 2.10}$$

[29]

$K$ and $K'$ are complete elliptical integrals defined as:

$$K = K(k) \equiv \int_0^{\pi/2} \frac{1}{\sqrt{1-(k\sin\Phi)^2}} d\Phi, \tag{EQ 2.11}$$

where $\Phi$ is the voltage of the enclosed element, and

$$K' = K(k'). \tag{EQ 2.12}$$



Reproduced with permission of the copyright owner. Further reproduction prohibited without permission.

Both $K$ and $K'$ can be calculated using tabulated elliptic integral functions. Fortunately, Hilberg developed an approximation where the ratio $\frac{K}{K'}$ can by calculated using first order approximation as shown below[30].

$$\frac{K}{K'} = \frac{\frac{\pi}{2}}{\ln\left(2\sqrt{\frac{1+k'}{1-k'}}\right)} \text{ for } 0 \le k \le \frac{1}{\sqrt{2}} \qquad \text{(EQ 2.13)}$$

and

$$k = \tan\left(\frac{\pi}{4}\frac{w}{w+L}\right), \qquad \text{(EQ 2.14)}$$

and

$$k' = \sqrt{1-k^2}. \qquad \text{(EQ 2.15)}$$

Now, we have all the pieces to design a simple transducer. Note that the same design can be used for both input and output transducers.

A simple SAW filter was designed on quartz, using an IDT as both input and output device. Silicon Valley Microelectronics[24] 42.75° Y-cut quartz wafers were used as substrate. Using equations described in the previous section, the number of fingers per IDT ($N$), and aperture width ($W$) were designed based on the smallest feature size dictated by the limitation of the fabrication facility. In this case, the finger width was the limiting factor and it was set at 2 μm, corresponding to SAW wavelength of 8 μm. Table 2.1 summarizes the design of the SAW filter.

| **Parameter** | **Value** |
|---|---|
| $\upsilon$ [m/s] | 3158.8 |
| $f_o$ [MHz] | 394.85 |
| Cut type | Y-cut 42.75° |
| $k^2$ | 0.00116 |
| $\varepsilon_r$ [F/m] | 4.5 |



Reproduced with permission of the copyright owner. Further reproduction prohibited without permission.

| Parameter | Value |
|---|---|
| $N_{opt}$ | 26 |
| W [μ m] | 244.8 |

**Table 2.1.** Design parameters for SAW filter on quartz substrate.

The fabrication process was done using a lift-off technique[31] and it is shown in Fig. 2.7, where the substrate was initially cleaned by a Piranha (mixture of sulfuric acid and hydrogen peroxide). Photoresist was then spread, spun, and baked (step a). Such prepared substrate was then patterned using a UV developing apparatus (step b). Al was then sputtered onto the substrate for 30 minutes producing about 0.5 μ m thick layer of metal. The lift-off process was then carried out using an ultrasonic agitation in an acetone bath.

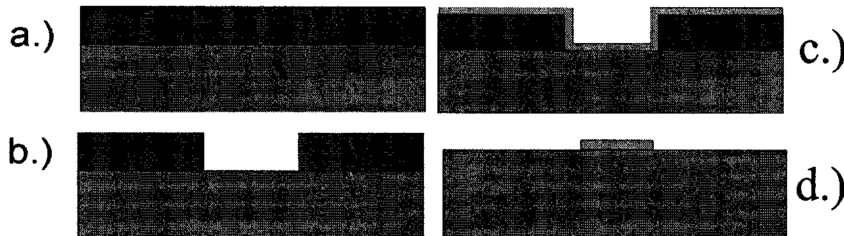


**Figure 2.7.** Lift-off process visualization[31].

The resulting IDT is shown in Fig. 2.8.



Reproduced with permission of the copyright owner. Further reproduction prohibited without permission.

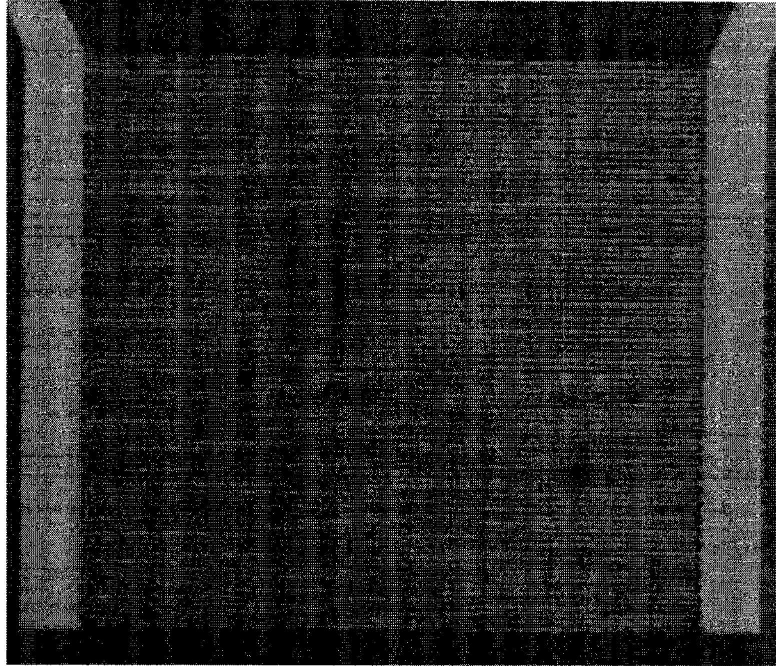

**Figure 2.8.** An IDT visible under 100X magnification.

The obtained filter was then characterized using a microwave probing station utilizing Picoprobe 40A-GS-250-P[32] probes as seen in Fig. 2.9.



Reproduced with permission of the copyright owner. Further reproduction prohibited without permission.

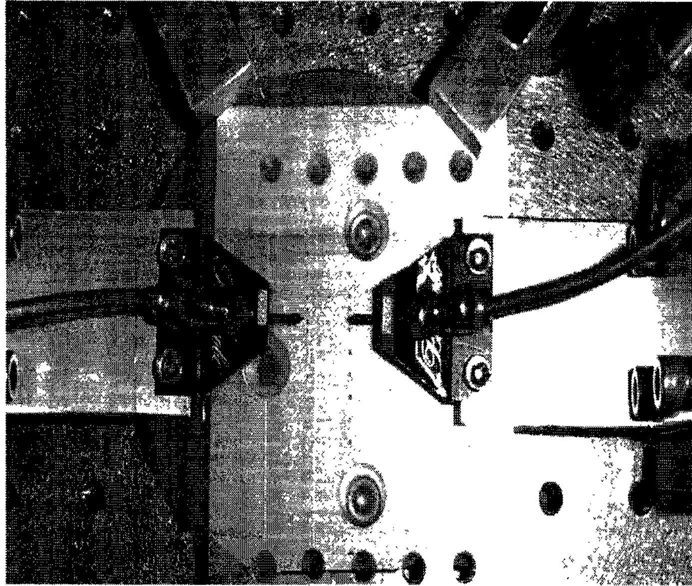

**Figure 2.9.** Microwave station setup using Picoprobe microwave probes.

The SAW IDT filter was then connected to the Agilent 8510C Network Analyzer to obtain the characteristics of the filter. The filter response is shown in Fig. 2.10

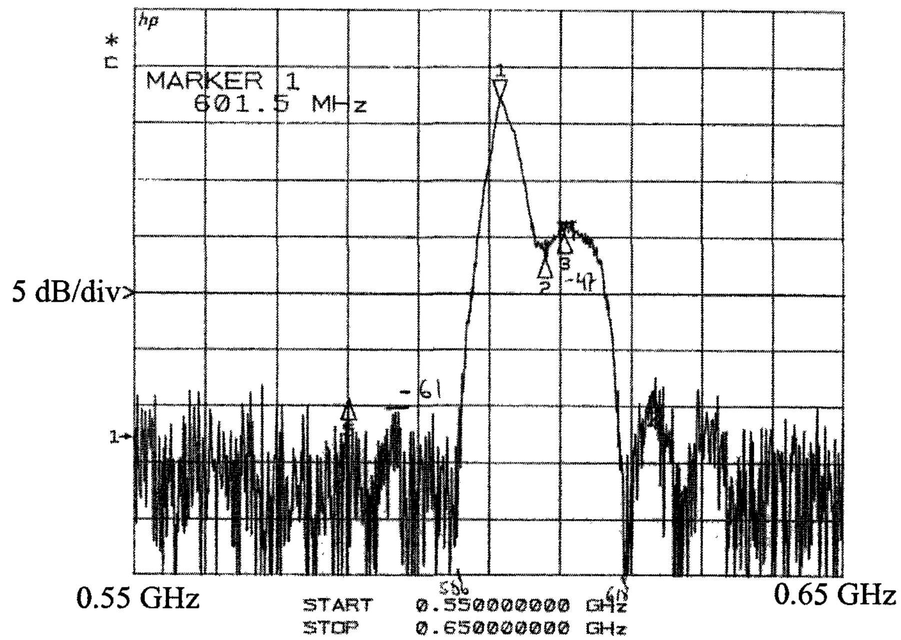


**Figure 2.10.** Frequency response of a SAW IDT filter on a quartz substrate.



Reproduced with permission of the copyright owner. Further reproduction prohibited without permission.

For comparison, a commercially available SAW quartz filter from ECS Inc. operating at 400MHz was purchased and mounted on a PCB with matched network (Fig. 2.11).

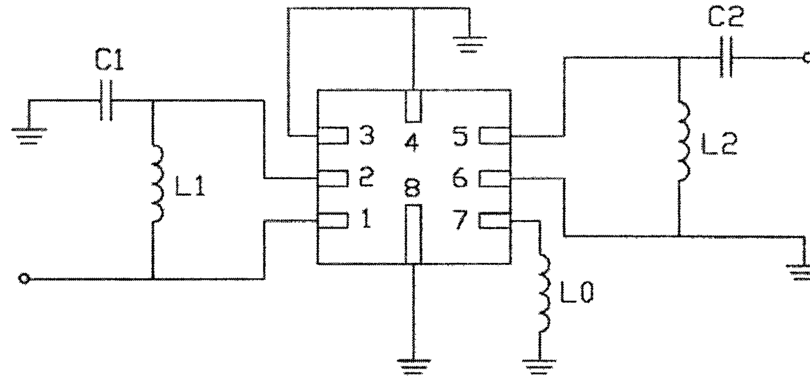


**C1=C2=2.7pF; L1=L2=27nH; L0=47nH**

**Figure 2.11.** Matching network for 400MHz quartz filter.

The frequency response of the filter is shown in Fig. 2.12.

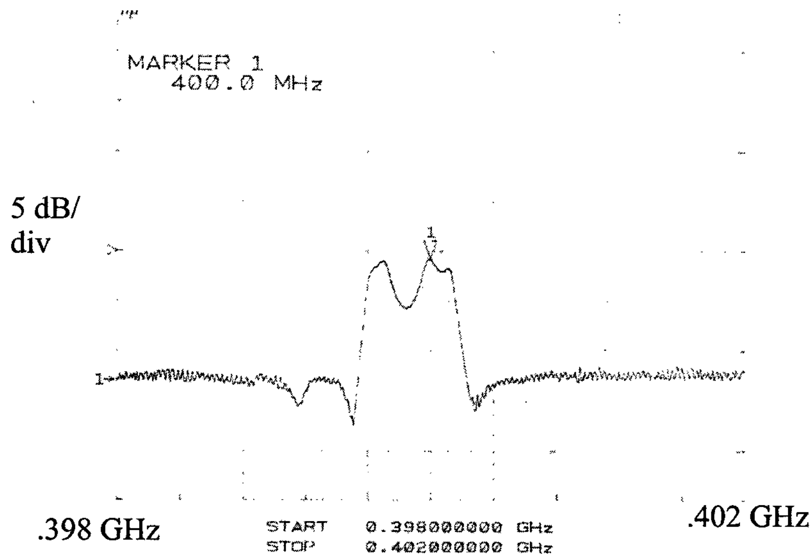


**Figure 2.12.** Frequency response of a 400MHz commercially available SAW filter.



Reproduced with permission of the copyright owner. Further reproduction prohibited without permission.

Comparison between Fig. 2.10 and Fig. 2.12 shows that the filter obtained through this design is not an ideal filter as the commercially available filter has a flatter response in a passband. Also, our filter has shifted the frequency of operation from the designed 394 MHz to the 600 MHz region. Eq. 2.1 specifies the relationship between the phase velocity, frequency of operations and wavelength. Our initial design called for a finger width and inter-finger spacing of 2 $\mu$m. The measurements of finger widths and inter-finger spacing using an SEM image shown in Fig. 2.13 shows the fingers to be narrower by 5-7% and spacings 10-15% narrower than the design. Calculating from that image, the effective wavelength would be 7.223 $\mu$m instead of 8 $\mu$m (assuming that the rest of the IDT is similar to the region which was captured in this SEM image). This would result in a shift of the center frequency to about 437 MHz; a significant shift of about 10%. We were unable to account for the rest of the shift in the centre frequency.

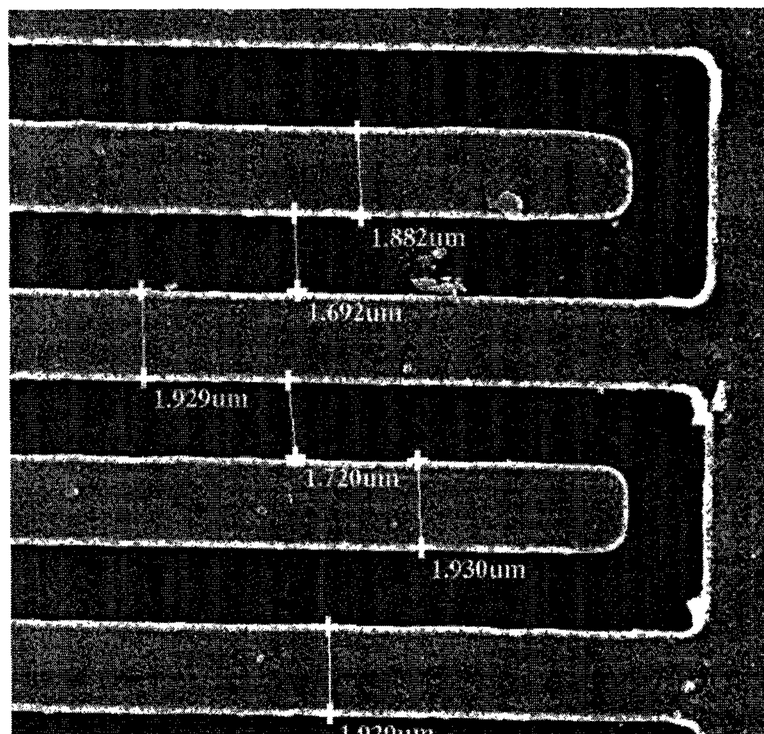


**Figure 2.13.** An SEM image of an IDT transducer.



Reproduced with permission of the copyright owner. Further reproduction prohibited without permission.

## 2.2. Photoelastic effect

The photoelastic effect couples the mechanical strain to the index of refraction. Mechanical stress causes changes to both the refractive index and birefringence. It occurs in all states of matter and is described by

$$\Delta\eta_{ij} = \Delta\left(\frac{1}{n^2}\right)_{ij} = p_{ijkl}S_{kl}, \qquad \text{(EQ 2.16)}$$

where $\Delta\eta_{ij}$ is the tensor describing the change in the optical impermeability, $S_{kl}$ is the strain tensor, and $p_{ijkl}$ is the strain-optic tensor[33]. Associated with the photoelastic effect is an acoustooptic figure of merit, which represents the relative change in index of refraction produced by an elastic wave of constant power. It is given by

$$M_2 = n^6 p^2/(\rho v^3), \qquad \text{(EQ 2.17)}$$

where $M_2$ is the figure of merit, $p$ is the photoelastic coefficient, n is the index of refraction, $\rho$ is the mass density of the propagation medium, and $v$ is the acoustic velocity of the substrate[34]. The change of the index of refraction is approximately given as

$$\Delta n \cong \sqrt{\frac{MP_{const}}{2A}}, \qquad \text{(EQ 2.18)}$$

where $A$ is the cross-sectional area and $M$ has units of $[M^2/W]$.

Bulk devices, including acoustooptic deflectors and modulators, utilize acoustooptic diffraction of light beams by an acoustic wave that is propagating through the bulk of the medium. In waveguide devices, surface acoustic waves are used as the source of acoustic perturbations that enable the photoelastic effect to be exploited[35].

In SAW devices that are used to induce acoustooptic interactions, a number of effects can take place due to index modulation. Modulation, deflection, and mode conversion are amongst the main guided-wave control mechanisms. Due to the small magnitude of the change of index of refraction, guided mode to radiation mode coupling is typically very



Reproduced with permission of the copyright owner. Further reproduction prohibited without permission.

weak, making mode conversion inefficient. Deflection is one the most useful effects exploited by SAW acoustooptic devices. An example is shown in Fig. 2.14.

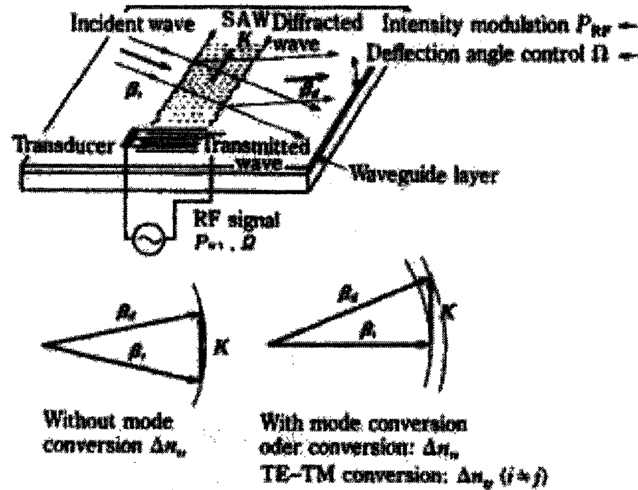


**Figure 2.14.** Guided wave control by acoustooptic Bragg diffraction. $\beta_i$ is the incident wave vector and $\beta_d$ is the deflected wave vector[35].

Interaction of an optical guided wave and a SAW is most efficient when the Bragg condition is satisfied by the wave vectors as seen in Fig. 2.14. The output deflected light has a a Doppler shift that will depend on the SAW velocity and the order of the deflection (since the grating is a travelling wave)[35].

The wave diffraction is dependent on the effects of surface corrugation from SAW propagation (as seen in the depiction of a SAW in previous sections), index modulation from the photoelastic effect, and for some crystals (including ferroelectrics and doped semiconductors) the electrooptic effect induced by the piezoelectric field. The contribution of the surface corrugation (relief effect) is usually small in bulk materials and can be neglected, but in the case of SAW and guided-mode waves it cannot be neglected. Depending on crystal orientation, SAW propagation direction, and the direction and polarization of guided



Reproduced with permission of the copyright owner. Further reproduction prohibited without permission.

waves, both of the effects vary in magnitude. In the case of TE-guided modes by a Y propagating SAW in Y-cut LiNbO3, the electrooptic effect can create a larger contribution than the photoelastic effect[35]. ZnO, being a semiconductor, behaves in a similar fashion; the more conductive the film sample is, the higher the contribution of the photoelastic effect relative to the electrooptic effect. This is the result of free carriers screening the contribution of the piezoelectricity to the total acoustooptic effect[36]. The errors that may arise from omitting the electrooptic contribution in design calculations can be corrected by changing the power of the SAW. When choosing a material combination for an acoustooptic device, a number of requirements must be met. These include the possibility for fabrication of high quality optical waveguides, a high efficiency of acoustooptic interactions, and small SAW propagation losses[35].

## 2.3. *Thin film characterization methods.*

### 2.3.1 Variable angle spectroscopic ellipsometry

Variable angle spectroscopic ellipsometry (VASE) measures the change in polarization state of light reflected from a sample. The extracted parameters are typically labelled $\Psi$ and $\Delta$. These parameters are related to the ratio of Fresnel reflection coefficients $R_p$ and $R_s$ according to Eq. 2.19.

$$\tan(\Psi)e^{i\Delta} = \frac{R_p}{R_s}. \qquad \text{(EQ 2.19)}$$

The typical VASE setup is shown in Fig. 2.15, where linearly polarized incident light is converted to elliptically polarized reflected light[37].

The model used with initial samples is shown in Fig. 2.16. The si02_jaw model describes the material and optical properties of the silica layer that was used as a substrate for film growth during the initial experiments. Values for silicon were obtained from the University of Alberta database and from Herzinger et.al[38]. The Cauchy layer model was used to



Reproduced with permission of the copyright owner. Further reproduction prohibited without permission.

describe the body of the dense PLD film and it assumes a standard Cauchy dispersion relation (commonly used for dielectric materials). The top layer of the film is modeled using srough, which represents a Bruggemann effective medium approximation[37] composed of 50% of the previous layer and 50% air void.

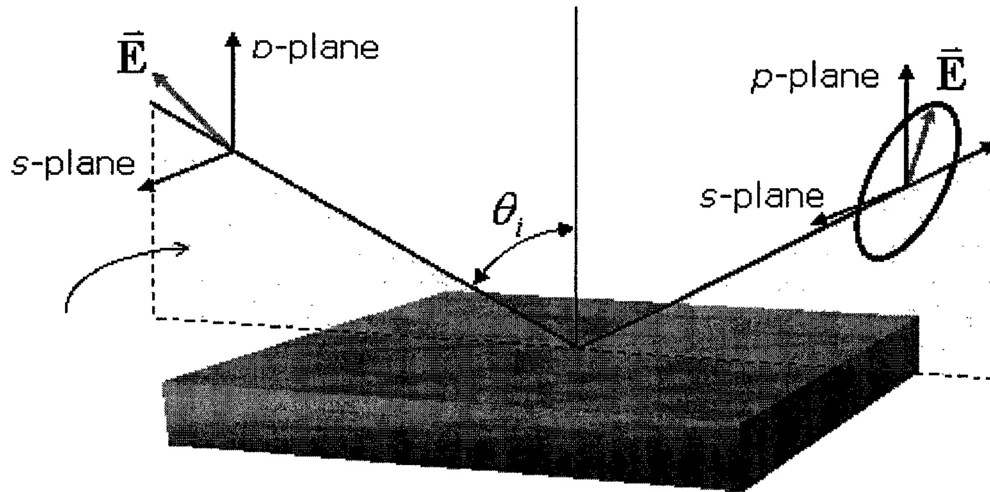


**Figure 2.15.** Schematic of geometry of an ellipsometry experiment[37].

| 2 srough |
| --- |
| 1 cauchy |
| 0 si02_jaw |

**Figure 2.16.** Thin film model. SiO2_jaw is the fused silica wafer substrate, cauchy represents the thin film grown, and srough is the surface roughness represented as 50% air void due to surface roughness and film porosity[39].

The spectrometer setup used to obtain the reflection data is a Woolham variable angle spectroscopic ellipsometer; it can measure refractive index and absorption coefficient from 240 nm to 1550 nm; and it can be fully automated to measure over a wide range of incidence angles[40].



Reproduced with permission of the copyright owner. Further reproduction prohibited without permission.

### 2.3.2 Scanning electron microscope (SEM)

The morphology, thickness, surface features, and crystal size of the films were characterized using a scanning electron microscope (SEM) by JOEL (model number JSM6301FXV). Images are produced by a beam of electrons accelerated by a voltage of 5kV, producing images ranging in magnification from 1000x to 100,000x. In a typical SEM, electrons are emitted via field emission and interact with the sample resulting in generation of secondary electrons and electromagnetic radiation, which are collected and used to produce images as those shown in Fig. 2.17[41]. Secondary electrons are electrons liberated from the inner orbit by a beam electron. These former orbital electrons, once freed, leave a vacancy that an electron from a higher energy level fills as it radiates photons with x-ray wavelength. Secondary electrons have low energy; therefore, only the electrons that are created within a short distance to the surface can escape. This effect makes secondary electrons very sensitive to surface topology[42]. The penetration depth and area size of the primary beam of electrons into the sample depend on the value of the excitation voltage and atomic number and density of the specimen, and it ranges from 100nm to 5$\mu$m

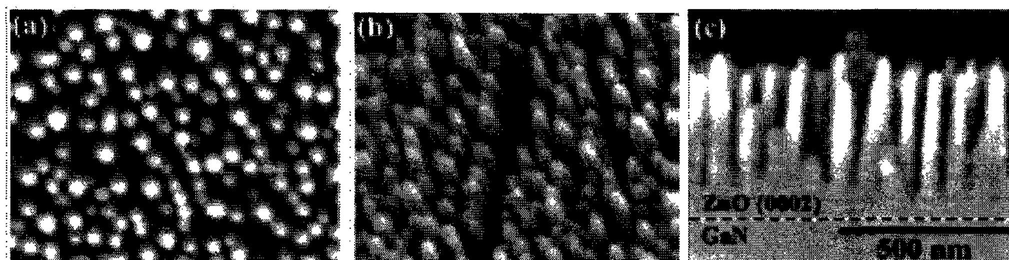


**Figure 2.17.** SEM images of ZnO on GaN. (a) top view, (b) 60 degree tilt, (c) side view[8].

### 2.3.3 Electron microprobe analysis

As part of SEM, electron microprobe analysis (EMPA) was performed on some of the samples. This technique is used to establish the composition of a small area on specimens; it uses the same beam of electrons that is used to produce SEM images to produce characteristic x-rays within a small volume of the sample. Initially, as described in the previous



Reproduced with permission of the copyright owner. Further reproduction prohibited without permission.

section, a beam electron knocks one of the inner shell electrons from a sample in a process of inner-shell ionization. After a short time ($1\times10^{-14}$ sec.), one of the outer shell electrons fills the vacancy and loses energy in the form of an x-ray photon. The characteristic x-rays and their intensities are detected at particular wavelengths. All of the elements except hydrogen, helium, and lithium can be detected in this fashion because each has a specific set of x-ray wavelengths that it emits[42].

**2.3.4 Room temperature photoluminescence**

Photoluminescence measurements were carried out using a frequency quadrupled Nd:YAG laser (266 nm, 20 Hz, 20 ns, 3.3 mJ/pulse) to optically excite the sample films. The setup for the characterization experiments is shown in Fig. 2.18. The photoluminescence signal is reflected off a collimating spherical mirror, passed through a set of filters to remove scattered light and laser radiation, and finally collected by a 400 μm diameter optical fibre that couples the light into the detector. Detection was performed with an Oceanoptics spectrometer (200-850 nm bandwidth, 8 nm resolution)[8]. Analysis of the data was done with a Matlab program by averaging samples in order to remove noise and spikes of the raw data.

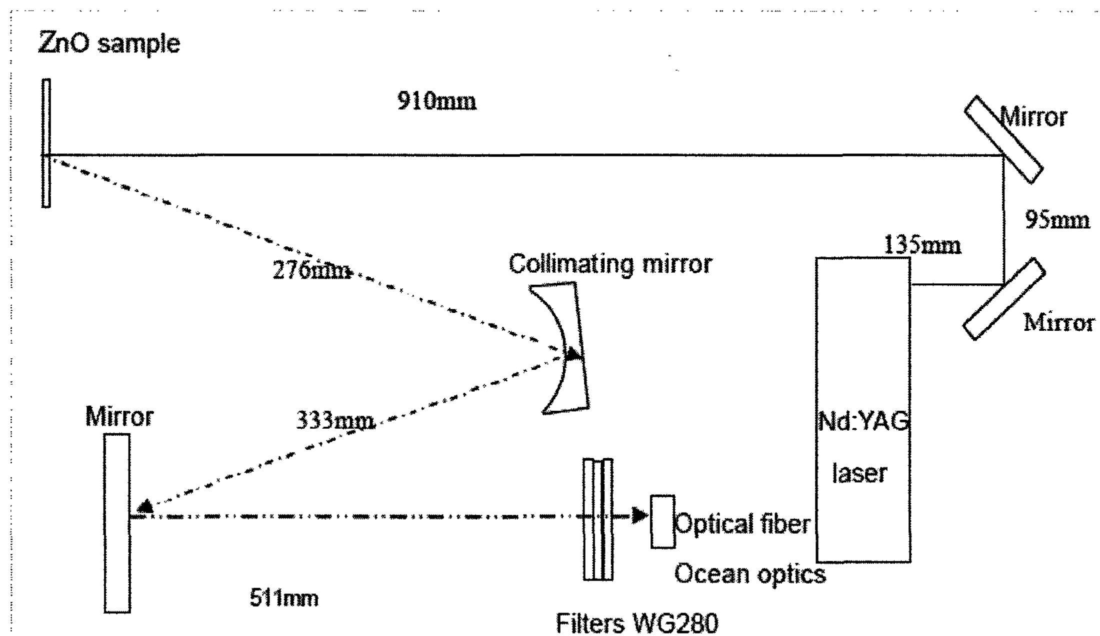




Reproduced with permission of the copyright owner. Further reproduction prohibited without permission.

**Figure 2.18.** Photoluminescence measurement setup[8].

A typical pre-processed and post-processed spectrum is shown in Fig. 2.19 and Fig. 2.20, respectively. Averaging was done with careful judgement and comparison with raw data so as not to distort the shape, peak value, and peak location.

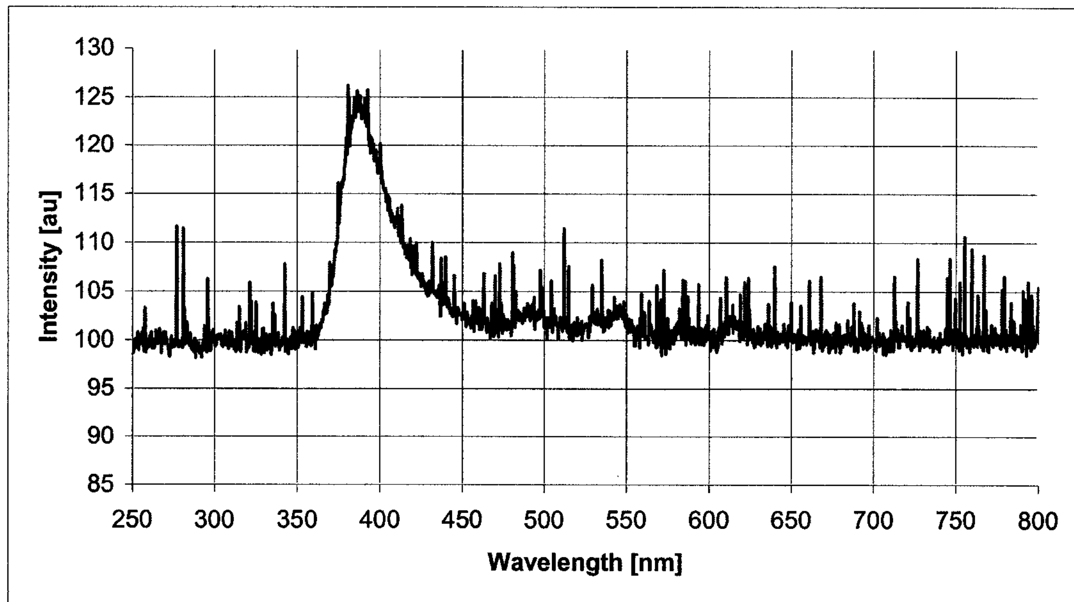


**Figure 2.19.** Photoluminescence signal raw data.



Reproduced with permission of the copyright owner. Further reproduction prohibited without permission.

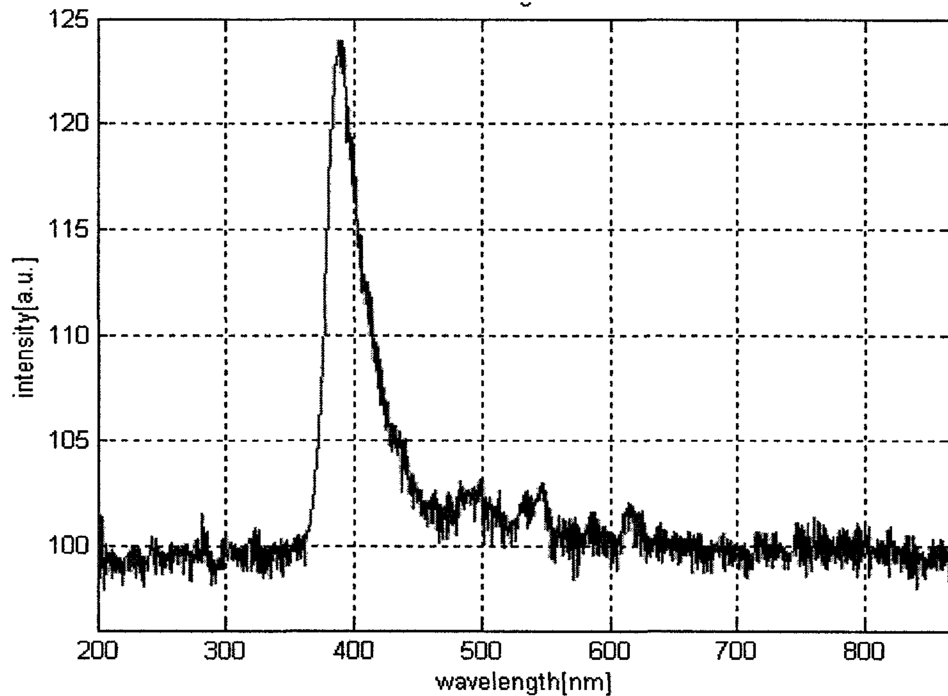


**Figure 2.20.** Post-processed photoluminescence signals.

### 2.3.5 Prism coupler measurements.

To augment the VASE measurements, film thickness and index of refraction (n) were also characterized using a prism coupling method. Fig. 2.21 shows the experimental setup for the measurements. The sample is brought into contact with the base of a coupling prism by a pneumatically-operated coupling head leaving only a small gap of air between the film and the prism. Laser light of a particular wavelength (in the present case it was 980 nm and 1550 nm solid state lasers that were used) is aimed at the substrate through the prism at different angles of incidence. Normally the beam is strongly reflected off the film surface, but at certain incident angles light couples into the film and propagates as an optically guided mode. These angles are called mode angles and they manifest themselves as sharp drops in reflected intensity as seen in Fig. 2.22.



Reproduced with permission of the copyright owner. Further reproduction prohibited without permission.

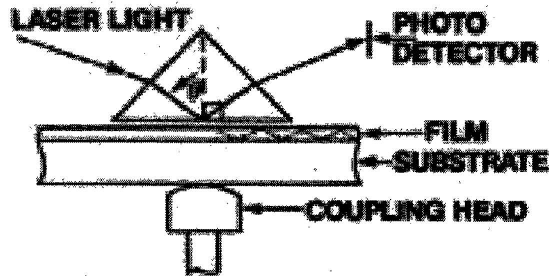


**Figure 2.21.** Metricon 2010 prism coupler measurement setup[43].

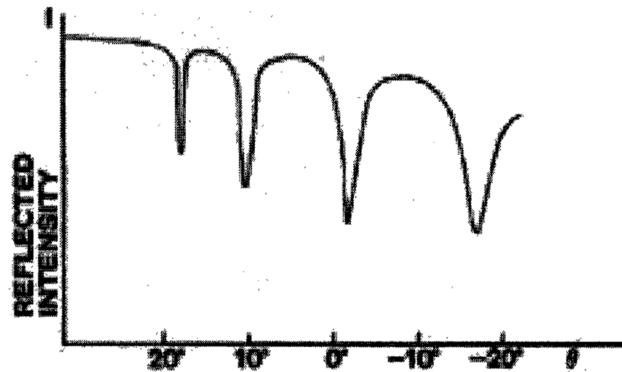


**Figure 2.22.** Intensity of reflected light vs angle of incidence[43].

Roughly speaking, the angle of incidence of a first coupled mode determines the film index, and the difference between the first and second coupled mode angles determines the film thickness. In the setup used, computer software provided by Metricon automatically scans through all possible angles in search of coupling mode angles. It uses pairs of angles and their separation to estimate index of refraction and thickness for each of the existing modes. Typically, a minimum thickness of 100-200 nm is required to support a single mode. Films with thickness on the order of a micron can support four to five modes depending on the material and the type of film[43].



Reproduced with permission of the copyright owner. Further reproduction prohibited without permission.

CHAPTER 3

# ZnO Films by PLD

PLD films were initially deposited on round (1 in. in diameter) fused silica glass substrates, and subsequently on p-type <100> Si wafers. Silicon processing is a mature technology, so that silicon has advantages as a platform for the development of thin films and microdevices. The advantage of using this particular wafer orientation is its ease of cleaving when preparing smaller samples.

## *3.1. Background on PLD technique*

Pulsed laser deposition (PLD) is a popular and flexible technique for thin film deposition. This method has been used ever since the inception of laser in the 1960's. Initially, the films grown by chemical vapour deposition and molecular beam epitaxy, among others, were still superior to those obtained using PLD. However, in 1987 Dijkkamp and Venkatsen deposited a high temperature superconductive material ($YB_2Cu_3O_7$) by PLD[44]. The quality of the material obtained using PLD was superior to that by using other methods at that time. Since then, the technology has improved due to better laser design, and due to the introduction of lasers with high repetition rates and short pulse duration. In the 1990's, PLD became popular for producing high quality crystalline films such as ceramic oxides, nitrides, metallic multilayers and various superlattices[44].



Reproduced with permission of the copyright owner. Further reproduction prohibited without permission.

### 3.1.1 Equipment

Conceptually, PLD is perhaps the simplest of all thin film deposition techniques. One of the greatest advantages of the PLD technique is the low cost of the deposition systems. To put it in perspective, a molecular beam epitaxy system (MBE) can cost 10 times as much as a PLD system. Another advantage is utilization of a single light source even when producing complex multi-layer films. This is achieved by either moving different targets in and out of the beam focal point or by using mirrors to change the beam path. Finally, the high energy component of the plume can effectively clean the substrate prior to film growth, thereby improving film adhesion. PLD has a number of disadvantages as well. The main disadvantage of PLD is its relatively low deposition rate, which leads to problems with scaling the process for mass production. Also, generation of large particulates can lead to film defects. However, use of magnetic guiding systems helps to minimize this effect[44]. A practical challenge in PLD is the need to use laser sources that align with the absorption bands of the material to be deposited[44].

A typical experimental setup consists of a target and a substrate holder that are housed in a vacuum chamber, a high power laser source that is used as an external energy source to vaporize the target materials, and some optomechanical components that will focus and/or raster the laser beam over the target surface. Film growth can be carried out in a reactive environment, in which case plasma excitation can be used to augment the growth of the film. A basic hardware setup is shown schematically in Fig. 3.1[44].



Reproduced with permission of the copyright owner. Further reproduction prohibited without permission.

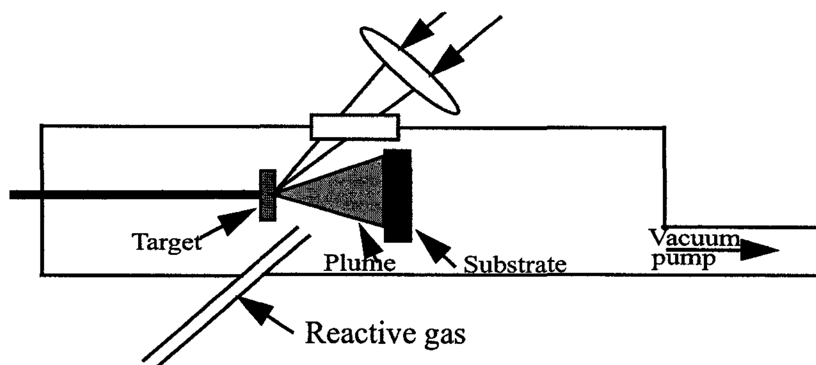


**Figure 3.1.** Schematic of a basic PLD setup[44].

The useful range of laser wavelengths for thin-film growth typically lies between 200 nm and 400 nm. Strong absorption by the Schumann-Runge bands of molecular oxygen and the inavailability of optics can make working in the part of the spectrum below 200 nm difficult[44]. One way of reducing the absorption of the light is to use nitrogen or vacuum filled tubes in the beam delivery system. This makes the experimental setup more expensive and complicated[8]. Two of the most popular high fluence sources (>1 J/cm$^2$) are neodymium yttrium aluminum garnet (Nd:YAG) and excimer lasers. Nd:YAG lasers are solid state lasers that utilize excitation of neodymium that is present as impurities in the YAG host. The garnet is optically pumped by flash lamps, and Q-switching is used to produce light pulses of about 2 J/pulse. The Nd:YAG's fundamental emission line is at 1064 nm; conversion to the wavelengths that are usable for PLD is achieved using non-linear crystals[44].

Excimer lasers are much more efficient in generating radiation useful for PLD because they emit in the desired region of the spectrum. Lasers of that category can generate pulses with energies up to 500 mJ/pulse, at repetition rates of several hundred Hertz. Table 3.1 lists types of excimer lasers and their wavelengths[44].

| Excimer | Wavelength (nm) |
|---|---|
| $F_2$ | 157 |
| ArF | 193 |
| KrCl | 222 |



Reproduced with permission of the copyright owner. Further reproduction prohibited without permission.

| Excimer | Wavelength (nm) |
|---|---|
| KrF | 248 |
| XeCl | 308 |
| XeF | 351 |

**Table 3.1.** Excimer laser types and their corresponding wavelengths[45].

Excimer lasers (excited dimer lasers) rely on compounds of two species that only exist in an excited state. The excitation is achieved through avalanche electric discharge that creates ionic and electronically excited species that react chemically and produce the excimer molecules. Typically, dimer compounds exist only for a few nanoseconds when the noble gas is in the excited state. When the noble gas atom is no longer excited, each compound molecule dissociates into its elements releasing the binding energy in the form of a photon. Fig. shows an excimer laser energy transition diagram[44].

Good quality deposition requires a homogeneous and uniform laser beam. Spikes in the profile of the beam, hot spots, and deviations from uniformity might cause problems with film stoichiometry, especially when working with multicomponent target materials. The optimal beam shape is a "top hat" profile that is rectangular when shown in cross-section. If the beam has any spikes, they will manifest themselves as areas of increased ablation on the target and will create non uniformities in the target[44]. An example of a "top hat" profile is shown in Fig. 3.2.

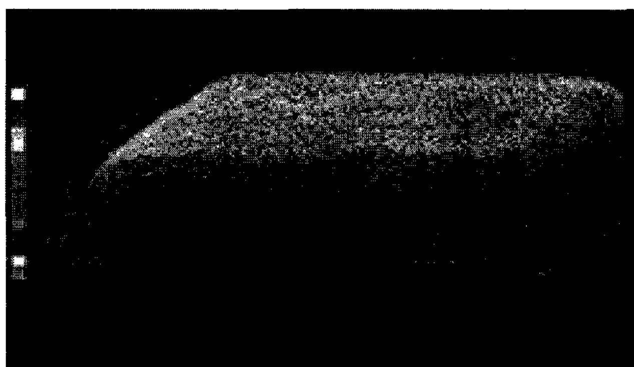

**Figure 3.2.** Beam profile of a 248 nm Atlex laser[46].



Reproduced with permission of the copyright owner. Further reproduction prohibited without permission.

The main optical components of PLD systems are reflectors, beam splitters, wedges, lenses, and various types of windows (chamber, splatter shields, etc.). In most cases, the energy density of the incoming laser beam needs to be above a threshold value determined by the target material in order to obtain the same composition in both the film and the target. Depending on the fluences and operational energies, various materials can be utilized in lens and window fabrication. Table 3.2 summarizes transmittance ranges of some of the lens and window materials that can be used in the UV to near-UV range of wavelengths. If fluence is low enough not to cause damage to the optics, fused silica is the most cost effective solution[44].

| Material | Transmittance Range (nm) |
|---|---|
| Magnesium fluoride | 140 - 7500 |
| Sapphire ($Al_2O_3$) | 150 - 5000 |
| Calcium fluoride | 150 - 8000 |
| UV-grade fused silica | 190 - 2500, 2600 - 4000 |
| Borosilicate crown glass | 315 - 2350 |
| Zinc sulphide | 400 - 12,000 |
| Zinc selenide | 550 - 16,000 |

**Table 3.2.** Transmittance ranges for various lens and window materials[44].

Most of the mirrors are made to have maximum reflectance at either 45 or 0 degrees and are designed specifically for a particular wavelength or range of wavelengths in order to make the beam delivery system as efficient as possible[44].

The final piece of the puzzle is the deposition system. Depending on the requirements, various combinations of deposition methods, pumping systems, and analysis equipment can be put together. A good and versatile foundation for a PLD system comprises a chamber, target holder(s), pump, reactive gas flow, and vacuum gauging. A number of companies offer ready-built solutions for PLD systems, but the relative simplicity of such systems, increasing availability of components, and decreasing cost of manufactured goods have enabled many laboratories to build their own PLD systems[44]. An in-house



Reproduced with permission of the copyright owner. Further reproduction prohibited without permission.

built system was used for production of films investigated during this thesis work; this system will be described in more detail in the next chapter.

### 3.1.2 Thin Film Nucleation and Growth

Three things may happen to an atom impinging on a surface: (1) it will adsorb and stick permanently to the substrate; (2) it will adsorb and re-evaporate in a finite time $\tau$; or (3) it will reflect immediately from the substrate.

Thin film growth will be favoured when the first process dominates. Those atoms that are adsorbed may in turn diffuse over the substrate, form mobile or stationary clusters when they encounter other mobile atoms, or form new clusters. This process of film growth is called Volmer-Weber nucleation[44]. In essence, small nuclei (clusters) have a very large surface-to-volume ratio and are not stable. The critical nucleus has a size above which the nucleus has a greater chance of being stable than evaporating. Therefore, in order to condense a permanent deposit, aggregates of critical size or larger must be created first. In practice, the size of a critical nucleus is larger for high vapour pressure materials and at high temperatures. For example, Cd, Zn, and Mg will require large critical nuclei due to the low boiling point of these metals; therefore, these metals will not condense easily on a substrate. Typical size of nuclei is 5 to 30 Å[47].

The first stage of the film growth is island formation, with adsorbed atoms going through formation of sub-critical size nuclei, proceeding through increase in size of nuclei to critical size, to formation of nuclei of super-critical dimensions with depletion of adatoms in the surrounding capture zones. In the coalescence stage, clusters touch and coalesce to form new islands that occupy less area than the original two islands also creating secondary nucleation on freshly exposed areas. In the next stage, large islands will grow together leaving channels or holes of exposed substrate. In the last stage, channels and holes will be filled in via secondary nucleation happening on exposed substrate areas giving way to continuous film. This stage occurs when the film is about 100-300Å thick[47].

The island formation film growth process will be enhanced by characteristics leading to a low density of nucleation sites, i.e. high substrate temperature, high vapour pressure of the



Reproduced with permission of the copyright owner. Further reproduction prohibited without permission.

film material, low deposition rate, weak bonding to substrate and clean substrate. Fig. 3.3 shows the first four stages of film growth[47].

**Figure 3.3.** First four stages of island formation. Clockwise from top left; (1) nucleation, (2) nuclei growth, (3) island formation, and (4) coalescence[48].

In the case when it is not energetically favourable for island formation, films will form in full monolayers. This is the basis for Frank-Van der Merwe growth[44], which still involves nucleation and growth of islands. However, the islands are now one monolayer thick and they grow to essentially complete coalescence before significant clusters are developed on the next film layer. In this regime, nucleation occurs in two-dimensional clusters of film atoms on the substrate; therefore, the degree to which true full-monolayer growth will happen depends on the density of nucleated clusters. High nucleation density will promote filling of complete monolayers before creation of new clusters, since vapour atoms impinging upon a small cluster will be more likely to add to the edges becoming part of a monolayer before they encounter other mobile atoms and nucleate to a new layer[44].

The last mode of film formation, called Stranski-Krastinov nucleation and growth, is a combination of the two previous methods. Film atoms initially form complete monolayers



Reproduced with permission of the copyright owner. Further reproduction prohibited without permission.

on a bare substrate, and after creation of about 1-5 monolayers, 3-dimensional clusters will start forming on top of the monolayers. This shift in growth method is caused by the stress due to mismatched lattice spacings for a higher number of monolayers. For films where nucleation starts to occur after 1-2 monolayers, it is the strong chemical bonding between the substrate and the film (which alters the surface energy of the initial layers) that could also be responsible for change in preferential growth mode[44].

The distance an average adatom (an atom that lies on a crystal surface) will diffuse across the film surface is controlled by the energy of an adatom, the deposition rate, and the binding energy for the film material. In columnar growth the diffusion length is large enough for an adatom to diffuse over some range after initial adsorption, and their range determines the size of growing columns. The resulting column is larger in diameter than the initial nucleation site. This leads to columnar film growth where the voids between the columns do not receive additional atomic flux. The shadowing affects the films growth even more as the angle of the plume becomes less normal to the film surface, as shown in Fig. 3.4[8].

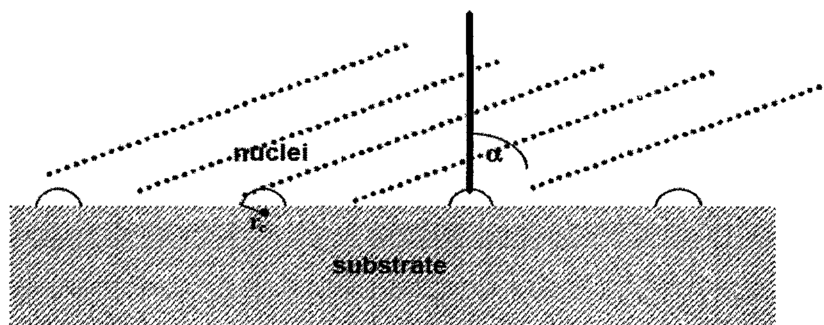


**Figure 3.4.** Diagram illustrating nucleus formation and shadowing effect[8].

Depending upon the substrate temperature, the film growth can fall into one of the three zones as shown in Fig. 3.5. In the first zone, atomic shadowing effects create highly voided dome-like structures. This happens because low substrate temperature results in low adatom mobility and very low bulk mobility. As the temperature increases, surface



Reproduced with permission of the copyright owner. Further reproduction prohibited without permission.

diffusion of adatoms overcomes the shadowing effect and the result is the slightly defected columnar grains growth seen in the second zone. High temperatures in Zone 3 create bulk diffusion and re-crystallization, leading to a fully annealed film with few defects[49].

**Figure 3.5.** Movchan-Demchishim structure zone model of thin film growth based on substrate temperature[49].

### 2.2.3 Background Gases

The use of background gases during deposition of PLD films has been shown to improve surface morphology. In the case of ZnO deposition, oxygen has been used as a reactive gas during film deposition[8].

During the ablation process, the ZnO plume may experience photon and electronic impact decomposition, resulting in production of atomic oxygen. These atoms do not necessarily recombine with Zn to produce ZnO at the substrate; they may also be devolved as oxygen molecules, resulting in oxygen deficiency of the film. The presence of an additional oxygen source will create a reactive atmosphere in the plume, thereby reducing the oxygen deficiency of the film. Adjusting the level of oxygen in the chamber also introduces the ability to tune the internal structure of ZnO by changing the defects in the film. The presence of oxygen in the plume results in an observable change of the plume as seen in Fig. 3.6 and Fig. 3.7 below[8].



Reproduced with permission of the copyright owner. Further reproduction prohibited without permission.

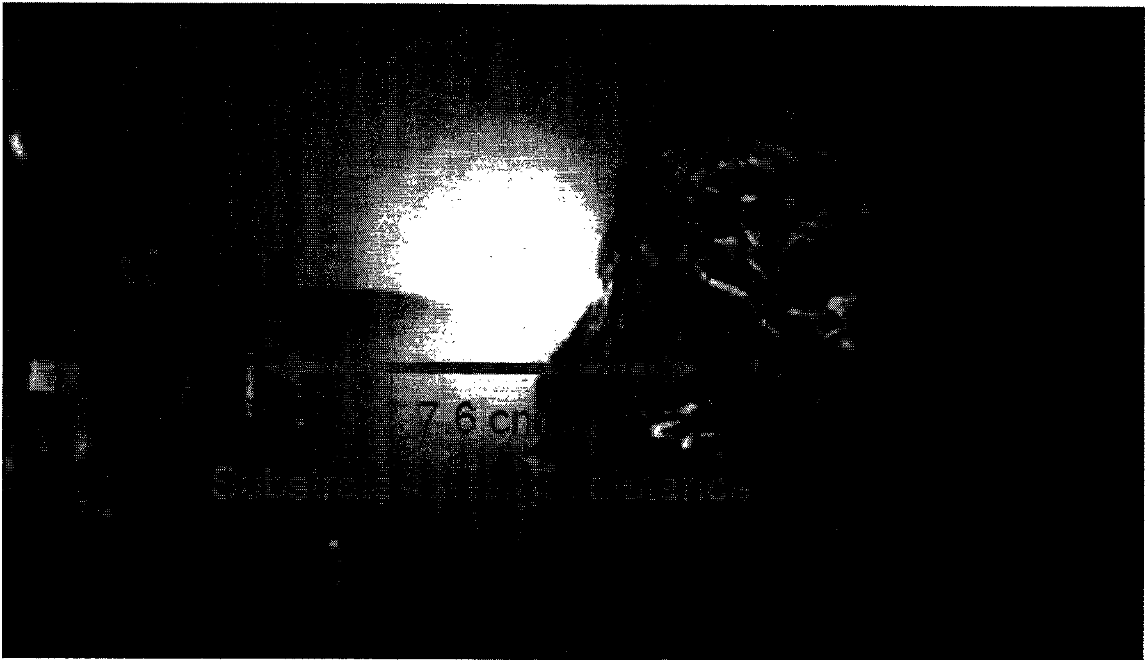


**Figure 3.6.** Plasma plume observed in 100mTorr of $O_2$ [8].

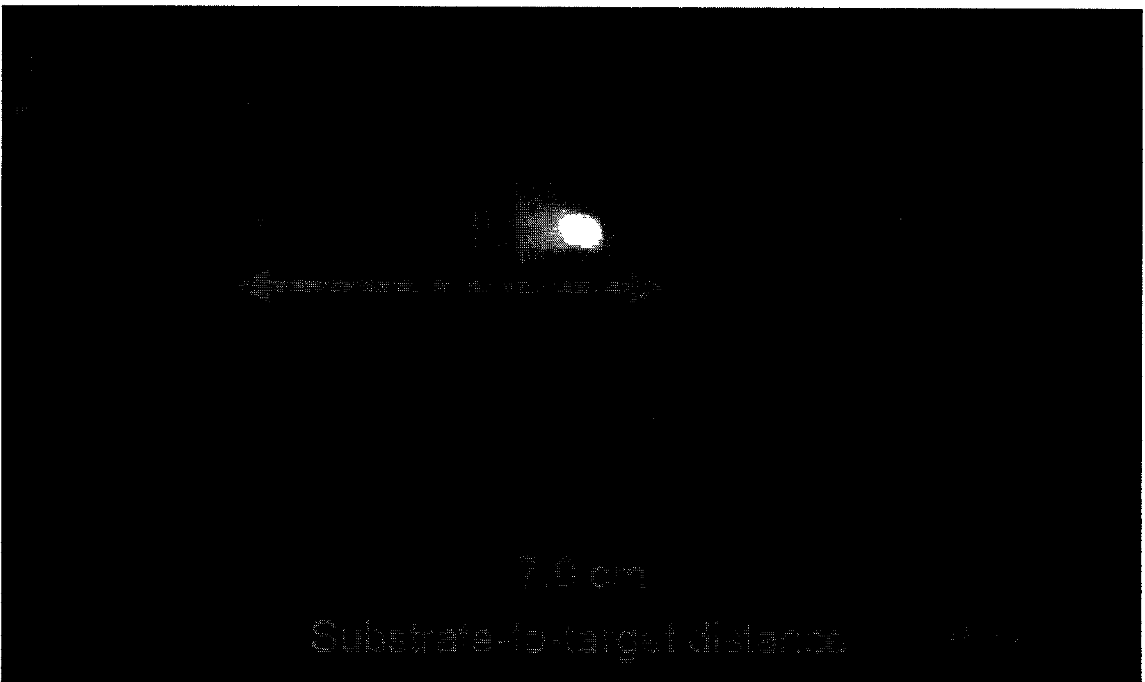


**Figure 3.7.** Plasma plume observed in vacuum[8].



Reproduced with permission of the copyright owner. Further reproduction prohibited without permission.

## 3.2. Pulsed Laser Deposition Setup

The PLD system used consists of a laser, focusing optics, and a vacuum chamber as shown in Fig. 3.8. The laser used was a 248 nm, 15ns KrF laser operating at 20Hz repetition rate. Vacuum was achieved with a combination of a mechanical pump and a diffusion pump. The system was first pumped to about $10^{-5}$ Torr base pressure and then backfilled with 66 mTorr of oxygen. The target was placed 33 cm from the lens and the substrate was placed about 4.5 cm from the target. These parameters were obtained experimentally by an M.Sc. student previously conducting experiments with the same deposition chamber[8]. Both the target and the substrate rotate. The rotation of the target prevents the creation of ablation craters and the rotation of the substrate is intended to create larger areas of uniform film thickness.



Reproduced with permission of the copyright owner. Further reproduction prohibited without permission.

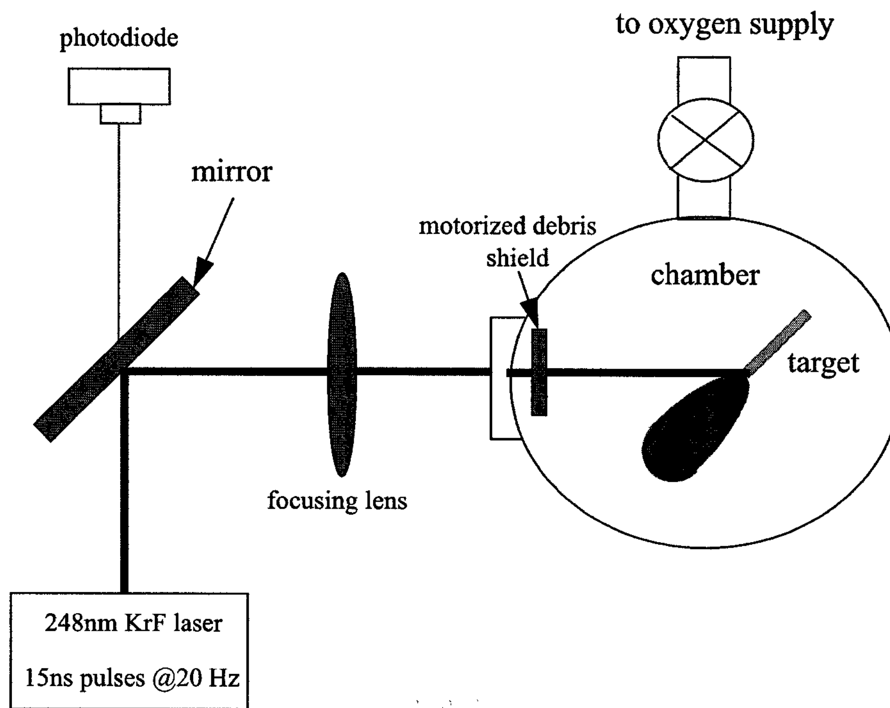


**Figure 3.8.** PLD setup during deposition

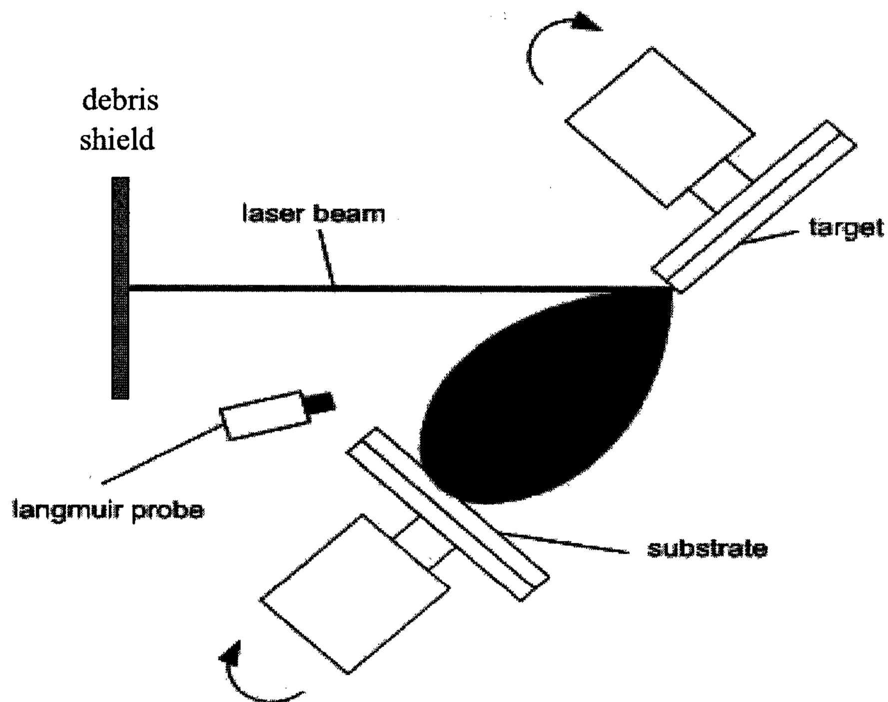


**Figure 3.9.** PLD stage setup with Langmuir probe for plasma plume characterization.



Reproduced with permission of the copyright owner. Further reproduction prohibited without permission.

### 3.1.1 Energy and plasma monitoring

The quality of both the laser beam and the plasma plume were monitored during the deposition. The laser beam was monitored using a photodiode that received the residual power transmitted through the mirror as shown in Fig. 3.8. The photodiode was calibrated using a calorimeter, in turn illuminated by 4% of the laser light by placing a wedge in the path as shown in Fig. 3.10. The KrF laser used yielded about 100 mJ per pulse during the deposition.

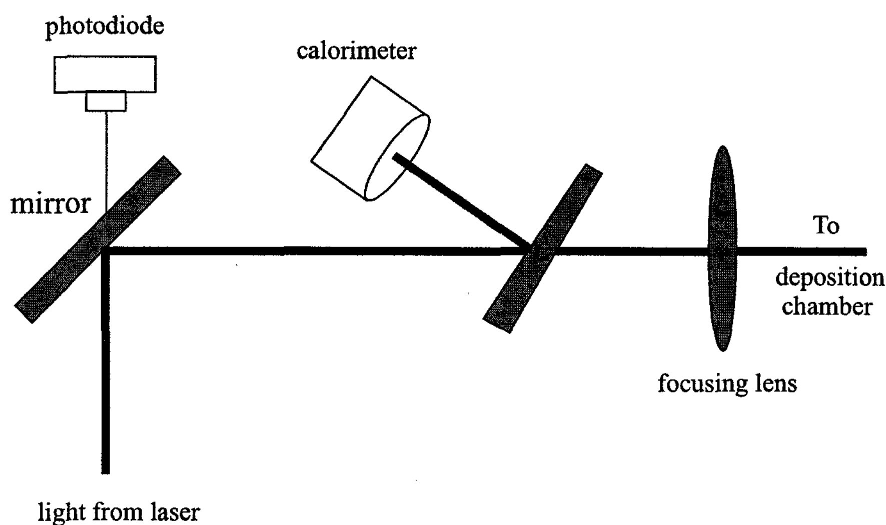


**Figure 3.10.** Energy parameter measurement setup

A rotating glass debris shield was placed inside the deposition chamber just after the chamber window. The debris shield protects the more expensive and more difficult to replace chamber window from energetic plasma particles that would otherwise coat it. The rotation mechanism spreads the build-up of film over a larger area, thereby increasing the effective transmission of the laser beam throughout the deposition. The effective transmission dropped from about 90% to about 80% during typical deposition times of 80 minutes. The debris shield was cleaned with 13% solution of ammonia bifluoride to remove deposits after each experiment.

As already discussed, during the deposition, the plasma plume can experience photon and electron decomposition and produce atomic oxygen. The atomic oxygen does not neces-



Reproduced with permission of the copyright owner. Further reproduction prohibited without permission.

sarily recombine with ZnO at the surface of the substrate, but can instead form molecular oxygen. This causes oxygen deficiency in the film leading to an increase in the number of defects in the final film. Introduction of oxygen background atmosphere mitigates this problem as well as introducing a mechanism for tuning the number of defects and the film stoichiometry[8].

The plasma plume was monitored during deposition using a Langmuir probe that was placed in the deposition chamber perpendicular to the plume as illustrated in Fig. 3.9. The probe was biased at -50 V DC to attract ions.

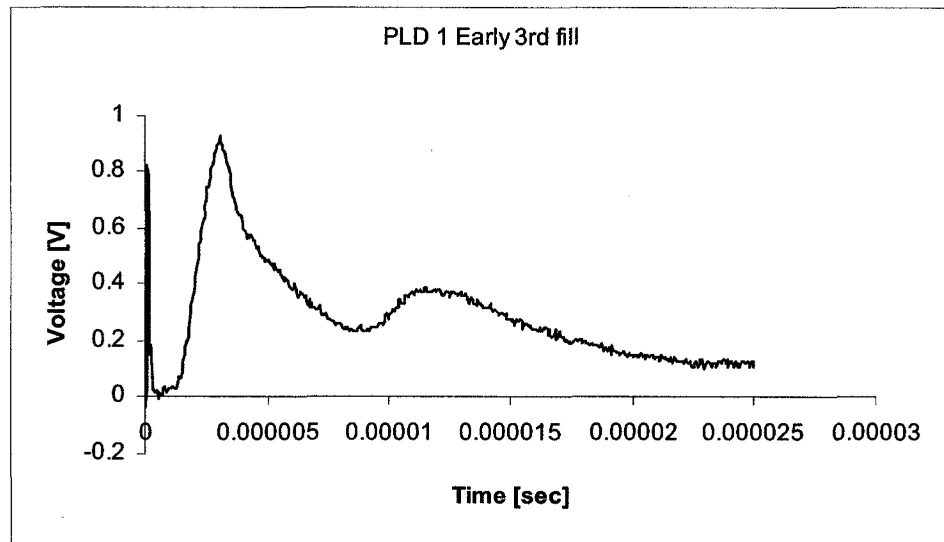


**Figure 3.11.** Typical Langmuir probe signature at the beginning of a deposition run with 100 mTorr oxygen background.



Reproduced with permission of the copyright owner. Further reproduction prohibited without permission.

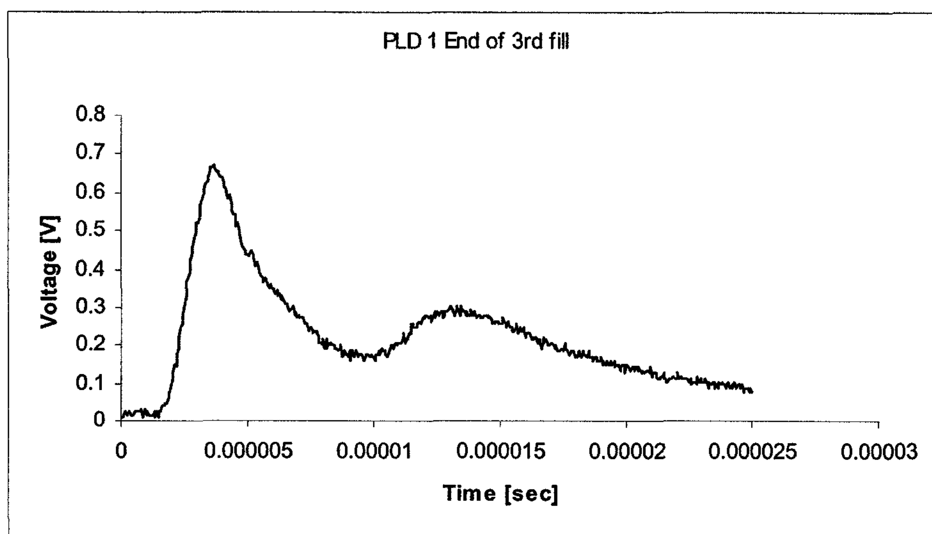


**Figure 3.12.** Typical Langmuir probe reading at the end of the deposition run with 100 mTorr oxygen background. This particular run yielded 91,200 shots in 76 minutes.

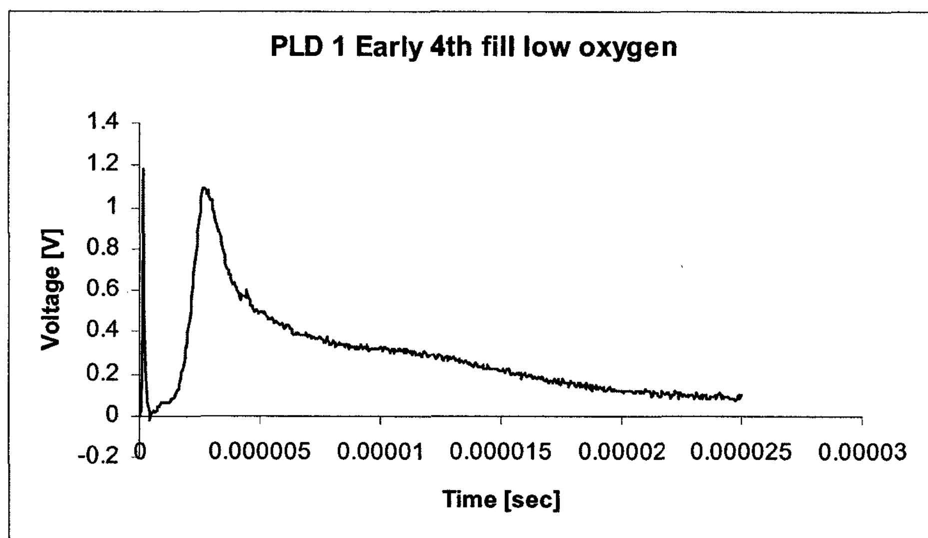


**Figure 3.13.** Langmuir probe signal corresponding to low oxygen pressure in the chamber.

As seen in Fig. 3.11, Fig. 3.12, and Fig. 3.13, the signal level is decreasing with increasing chamber pressure. This is mainly due to the larger number of molecules present at increased pressures, which leads to a larger number of collisions of plasma particles with chamber atmosphere molecules, ultimately leading to a lower number of particles arriving



Reproduced with permission of the copyright owner. Further reproduction prohibited without permission.

at the substrate (thus lower deposition rate). The substrate to target distance was held constant throughout the deposition experiments, but according to earlier research by YangWen[8], the signal level and thus number and rate of particles arriving at the substrate decreased as the distance between substrate and target increased. This is intuitive: with increased distance that the particles need to travel, there is a higher probability of collision with chamber atmosphere molecules. The signal from the Langmuir probe was also used as a diagnostic tool in ensuring constant oxygen levels were maintained within the chamber, in order to keep film stoichiometry (thus defect levels) constant.

### *3.3. PLD films on quartz.*

Initial depositions were performed on 1 inch diameter fused silica glass blanks in order to facilitate characterization of the film's optical constants, (index of refraction) and film thickness. The substrate position on the substrate holder is shown in Fig. 3.14. The substrate holder was attached to the motor at its centre. The off-centre position of the plume moves it in and out of the substrate area resulting in larger deposition area at the cost of overall film thickness (for a given deposition time).

The films in this deposition were exposed to the plasma for 81 min.



Reproduced with permission of the copyright owner. Further reproduction prohibited without permission.

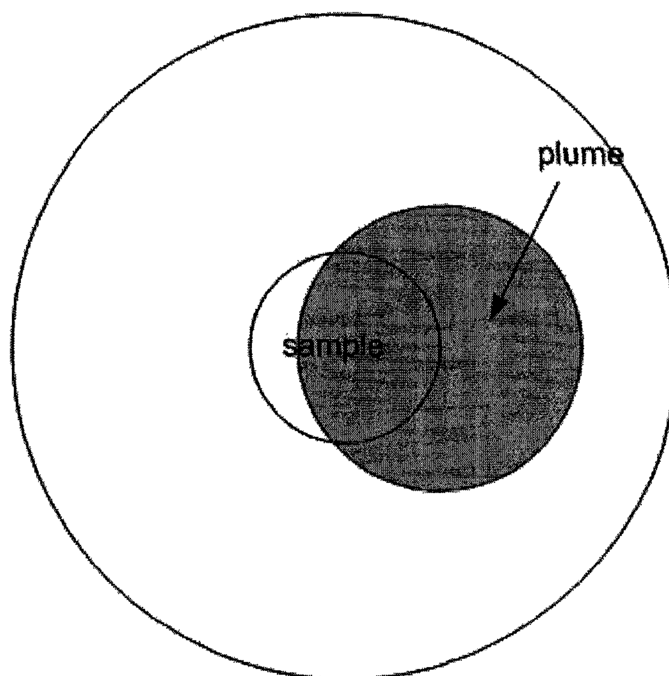


**Figure 3.14.** Plume position on the holder with respect to the substrates.

Optical constants were measured using variable angle spectroscopic ellipsometry. The comparison of experimental and modelled results is shown in Fig. 3.15. The two curves shown represent values of $\Psi$ at two different regions of the film. The values of *n* and *k* calculated from those two fits of $\Psi$ were close to each other, so only one is shown in Fig. 3.16.

As discussed in the previous chapter, the sample composition consisted of fused silica substrate, a Cauchy layer representing dense ZnO film growth, and finally, the top layer representing surface roughness as shown in Fig. 2.16. The VASE instrument extracted an estimate of 652 nm for the Cauchy layer thickness, and an estimate of 28 nm for the rough surface (air void layer). The extracted values of real and imaginary part of the index of refraction, n and k respectively, are plotted in Fig. 3.16. The comparison between the experimental indices for the ZnO film and expected indices for bulk ZnO are shown in Fig. 3.17. The values of $n_o$ and $n_e$ were obtained by using dispersion formulae available in the literature for bulk ZnO[50]. The experimentally obtained value has a lower index of



Reproduced with permission of the copyright owner. Further reproduction prohibited without permission.

refraction throughout the whole range. This is somewhat expected since the thin films are probably not as dense as bulk material.

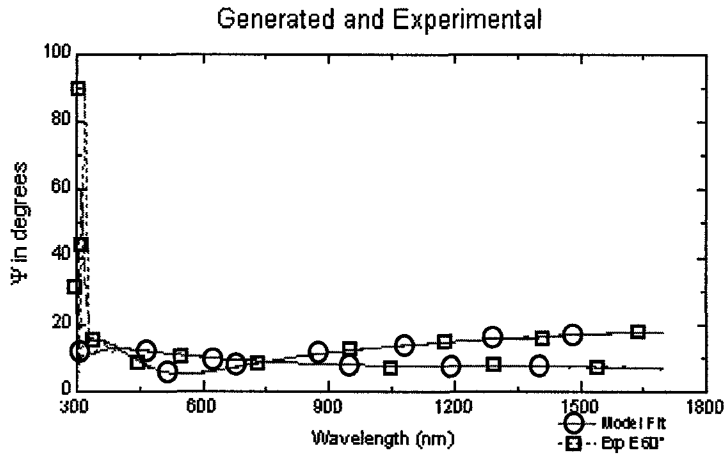


**Figure 3.15.** Fit of model to experimental values of Ψ. Note that the model agrees very well with the fit past 300 nm (they are on top of each other). The values provided here are for two runs.

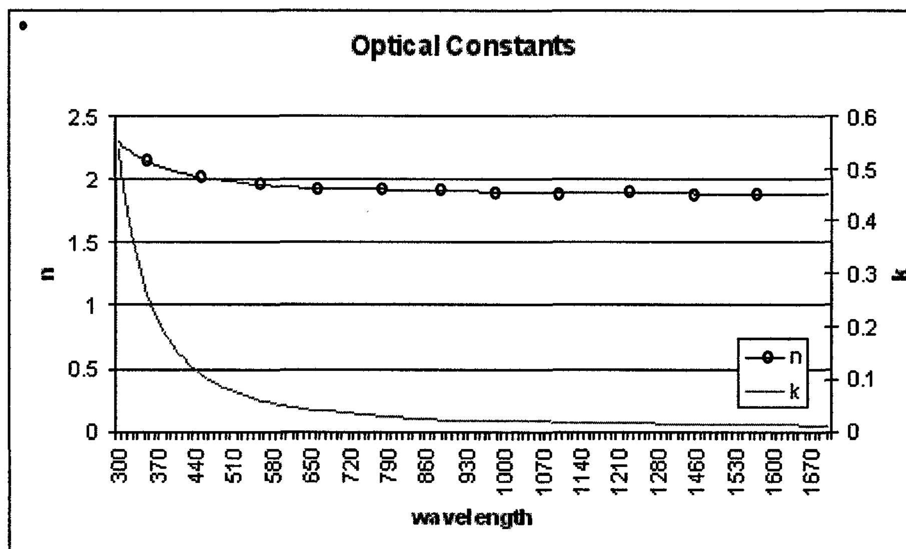


**Figure 3.16.** Experimentally extracted results for of n and k of a ZnO film on fused silica.



Reproduced with permission of the copyright owner. Further reproduction prohibited without permission.

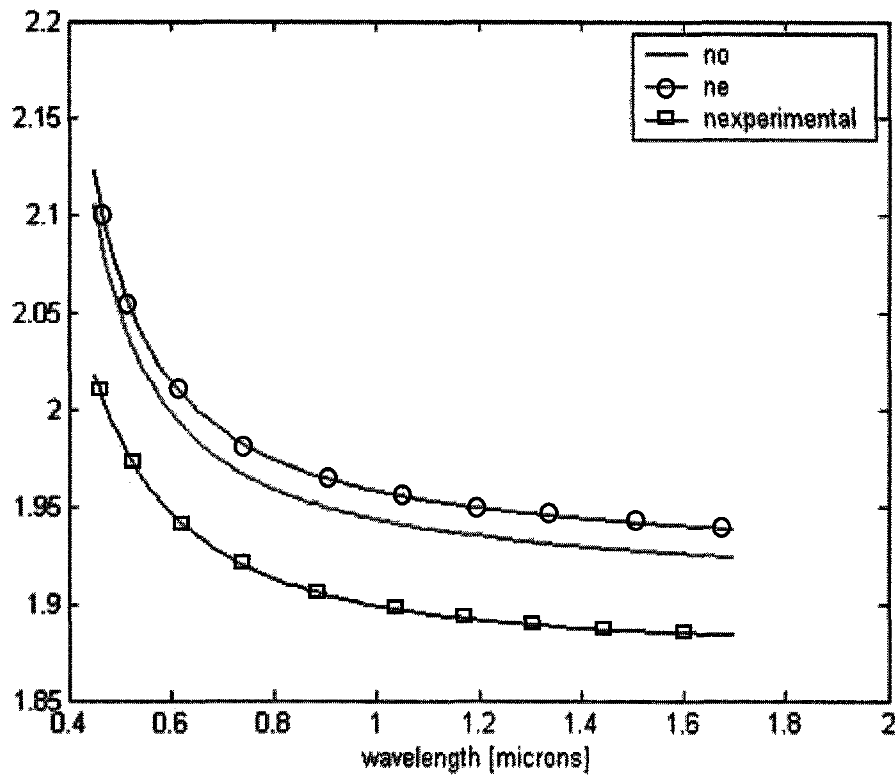


**Figure 3.17.** Comparison of experimentally obtained values of n with those calculated using dispersion formulas shown in Eq. 3.1 and Eq. 3.2.[50]

$$n_o^2 = 1 + 2.6\lambda^2/(\lambda^2 - 211.9) \quad \text{(EQ 3.1)}$$

$$n_e^2 = 1 + 2.66\lambda^2/(\lambda^2 - 214.3) \quad \text{(EQ 3.2)}$$

## *3.4. PLD films on silicon*

After exploration of deposition on fused silica substrates, the next set of depositions was carried out on p-type <100> oriented Si substrates. Two types of substrate mounting schemes were used, as shown schematically in Fig. 3.14 and Fig. 3.18. With the plume directly on the substrate, the film was expected to be thicker, but the thickness uniformity was expected to be lower than in the case of plume aimed off-centre of the substrate. Table 3.3 lists the different PLD films that were deposited along with substrate orientation



Reproduced with permission of the copyright owner. Further reproduction prohibited without permission.

on the substrate holder, laser fluence during the deposition, and film characteristics that were measured using the various methods described in previous chapters.

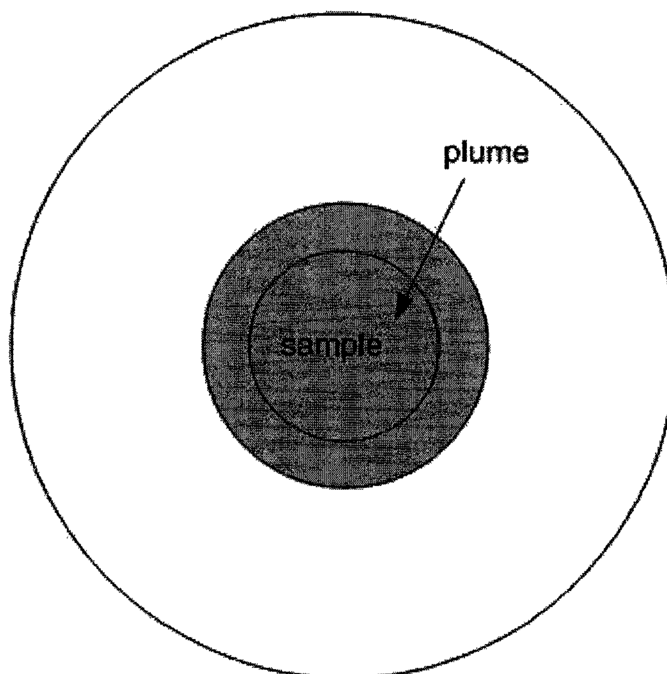


**Figure 3.18.** Plume is centered on the sample.

| Deposition | Laser Fluence | Plume position | Annealed* | Thickness | n | Dep. Time |
|---|---|---|---|---|---|---|
| PLD 1-1 | 2.41 $J/cm^2$ | Centre | Yes | 390 - 470 nm | N/A | 74 minutes |
| PLD 1-2 | 2.41 $J/cm^2$ | Centre | No | 390 - 470 nm | N/A | 74 minutes |
| PLD 2-1 | 2.37 $J/cm^2$ | Off-centre | Yes | 250 - 280 nm | N/A | 91 minutes |
| PLD 2-2 | 2.37 $J/cm^2$ | Off-centre | No | 250 - 280 nm | N/A | 91 minutes |
| PLD 3 | 5.01 $J/cm^2$ | Off-centre | Yes | 480 nm | N/A | 80 minutes |
| PLD 4 | 4.56 $J/cm^2$ | Centre | Yes | 560 - 700 nm | 1.91 | 80 minutes |
| PLD 5 | 4.5 $J/cm^2$ | Centre | Yes | 580 nm | 1.95 | 85 minutes |

**Table 3.3.** Summary of PLD films deposited on Si substrates. * See discussion below.

Films in PLD 1 were deposited with the plume on the centre of the substrate, which was mounted in the centre of the substrate holder. Films in PLD 2 were deposited with plume



Reproduced with permission of the copyright owner. Further reproduction prohibited without permission.

aimed off-centre as to obtain a larger area of uniform film. The film in PLD 1 was deposited for 74 minutes and film in PLD 2 was deposited for 91 minutes. Images below were obtained using SEM.

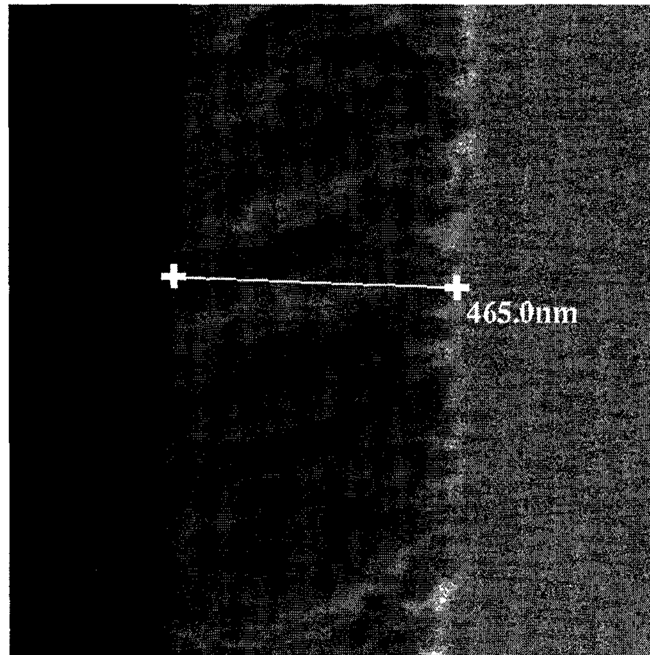


**Figure 3.19.** Side SEM image of PLD 1-1 on the thicker side of the sample.



Reproduced with permission of the copyright owner. Further reproduction prohibited without permission.

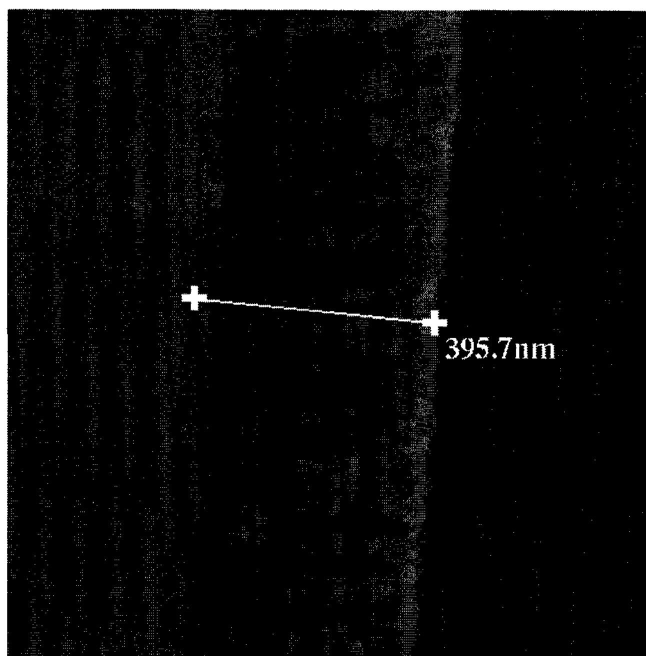


**Figure 3.20.** Side SEM image of PLD 1-1 on thinner side of the sample.

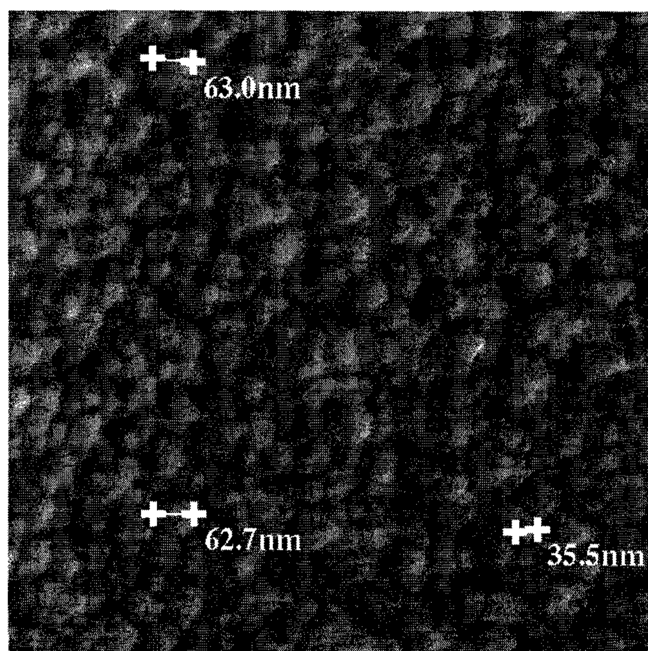


**Figure 3.21.** Angle SEM image of PLD 1-1 showing crystal sizes on the order of 60 nm.



Reproduced with permission of the copyright owner. Further reproduction prohibited without permission.

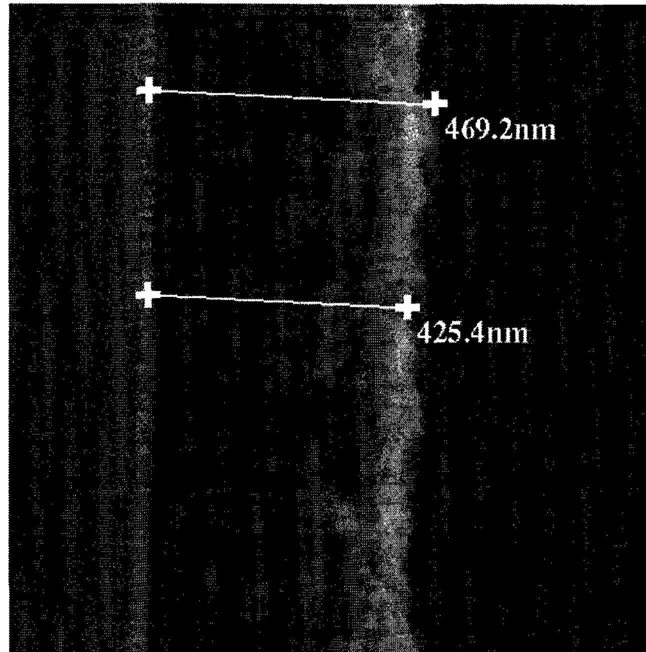


**Figure 3.22.** Side SEM image of PLD 1-2.

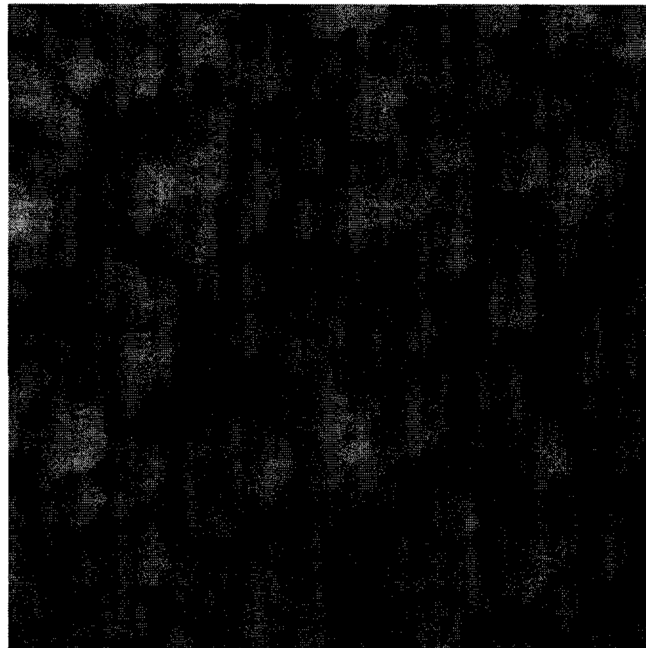

**Figure 3.23.** Top SEM image of PLD 1-2. Crystal sizes in this sample were on the order of 20-30 nm.

PLD 1 films that were annealed in air at 600° C for 2 hrs did not exhibit significant change in the size of crystals, as shown in Fig. 3.21 and Fig. 3.23. However, according to Yang-



Reproduced with permission of the copyright owner. Further reproduction prohibited without permission.

Wen,[8] annealing changes the composition of the film from separate Zn and ZnO crystals to a mostly ZnO crystal structure. In PLD 1, peeling was observed after annealing. This could be mainly attributed to surface cleanliness, as this effect was not observed for PLD 2 where Piranha solution was used to clean the substrate prior to deposition.

The subsequent sets of depositions, PLD 3 through PLD 5, were conducted with the plume either off-centre (PLD 3) or centred on the substrate holder (PLD 4, and 5).

The visual morphology of the films was very similar for all samples. Thicknesses ranged from 480 nm to just over 700 nm, as shown in Fig. 3.24 and Fig. 3.26 (depending whether the film was deposited with plume centered on the substrate or off-centre). Films produced in PLD 4 and 5 were also characterized using the prism coupler technique in order to measure the index of refraction of the films. The measurements were taken using a 980 nm light source and yielded an index of 1.91 and 1.95 for PLD 4 and PLD 5, respectively as shown in Table 3.3. The numbers compare very well with results obtained for the ZnO films deposited on fused silica substrates, discussed in the previous section. As in that case, these films presumably contain more air voids than bulk ZnO.

Room temperature photoluminescence (PL) measurements were performed on PLD 3 to PLD 5 samples, and are shown in Fig. 3.28, Fig. 3.29, and Fig. 3.30. ZnO exhibits a photoluminescence peak corresponding to the band gap emission at 380 nm (3.26 eV)[8], which is clearly visible in the above mentioned figures. However, PLD 4 and PLD 5 exhibit an additional band that is very near the main emission peak of 380 nm. This was not common to the entire film, as PL measurement on another portion of the PLD 5 sample (shown in Fig. 3.31) does not exhibit the same extra luminescence band. This additional luminescence might be attributable to film defects or zinc deficiencies in the film, but it is not completely understood[51]. The effects of the film defects on the bandgap is shown in Fig. 3.32. Both samples were annealed in air at 600° C for 2 hrs prior to the photoluminescence measurements.



Reproduced with permission of the copyright owner. Further reproduction prohibited without permission.

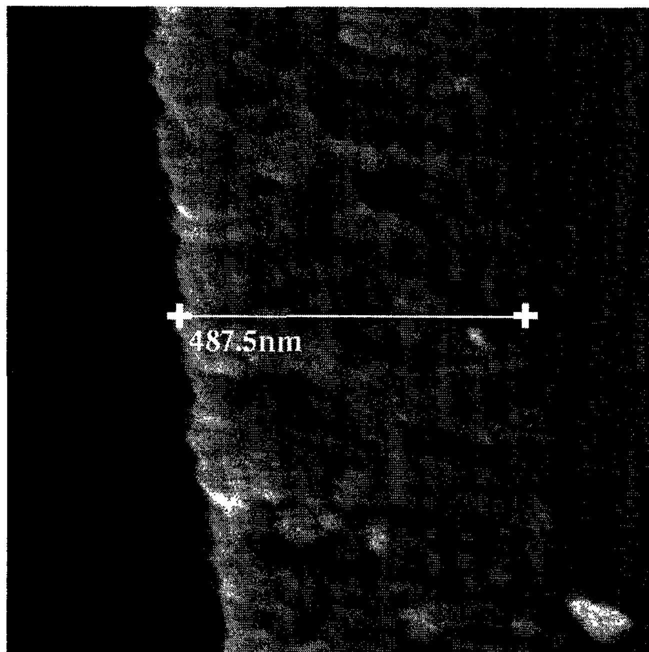


**Figure 3.24.** Side SEM image of PLD 3.

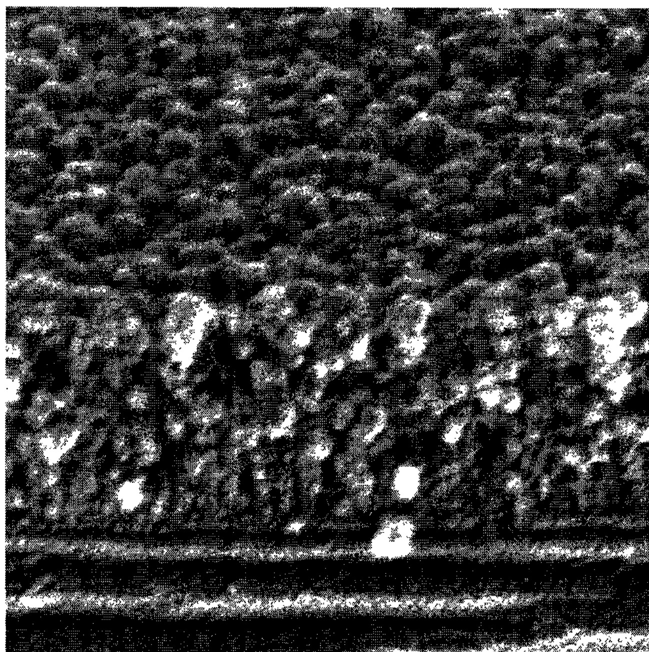

**Figure 3.25.** Angle SEM image of PLD 3 surface.



Reproduced with permission of the copyright owner. Further reproduction prohibited without permission.

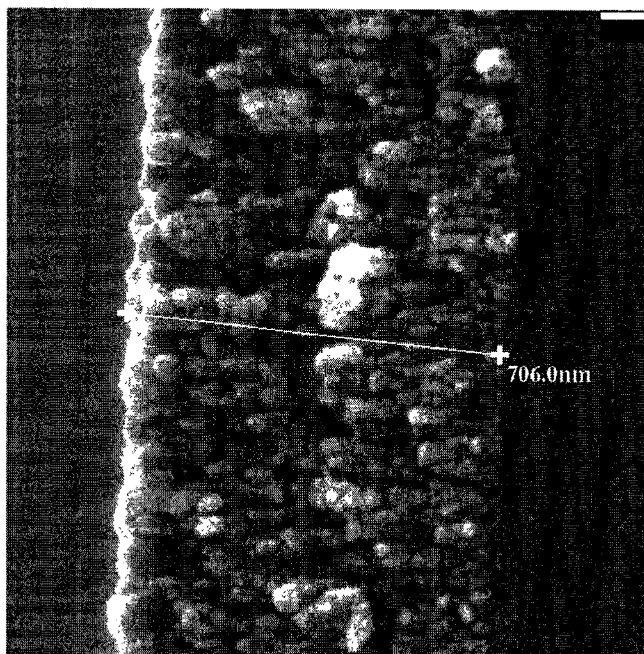


**Figure 3.26.** Side SEM image of PLD 4.

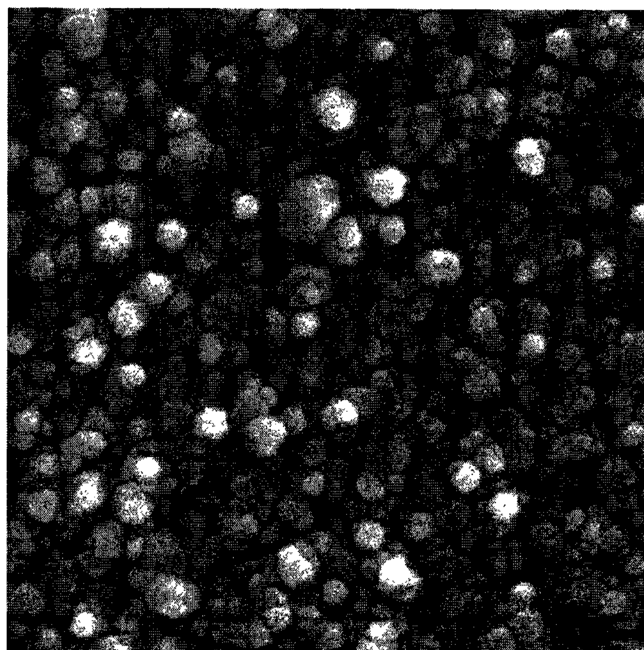

**Figure 3.27.** Top SEM image of PLD 4 surface.



Reproduced with permission of the copyright owner. Further reproduction prohibited without permission.

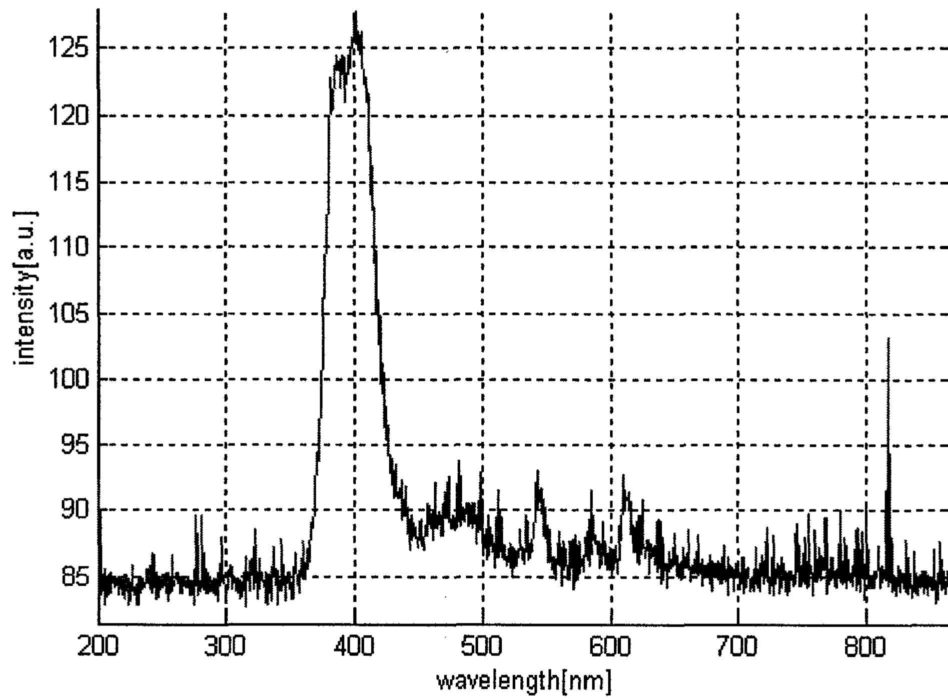


**Figure 3.28.** Room temperature PL spectrum of PLD 3.

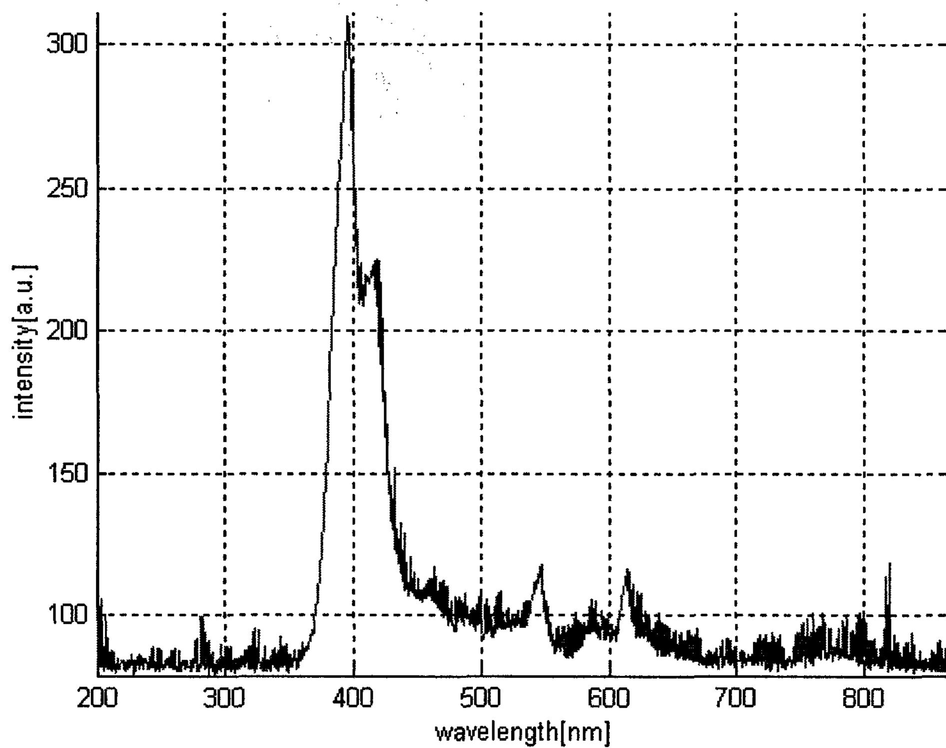


**Figure 3.29.** RT PL spectrum of PLD 4.



Reproduced with permission of the copyright owner. Further reproduction prohibited without permission.

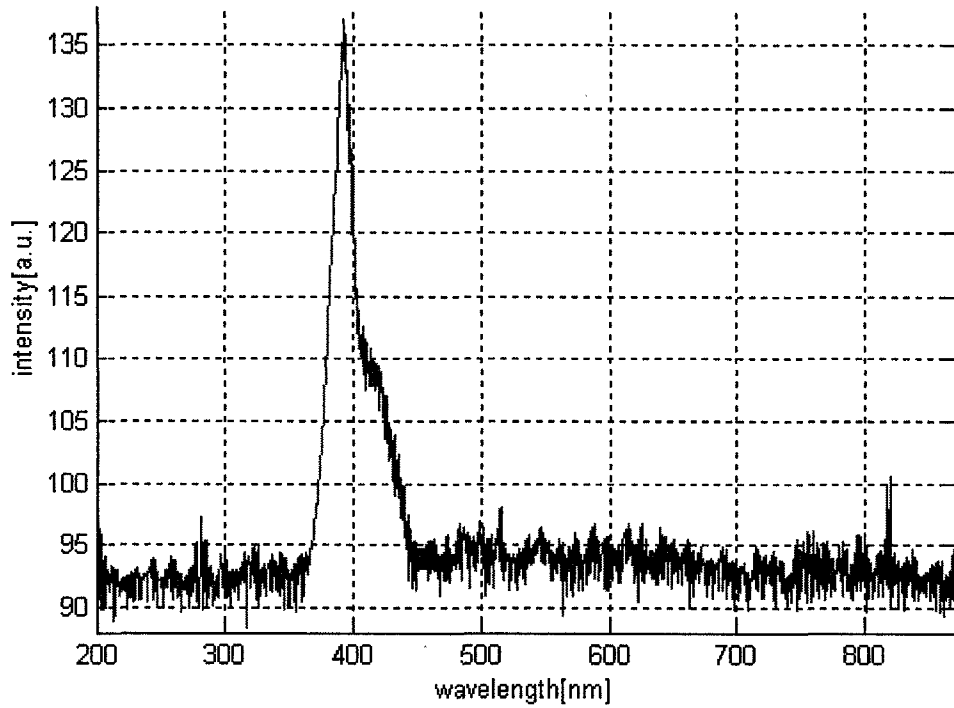


**Figure 3.30.** RT PL spectrum of PLD 5.

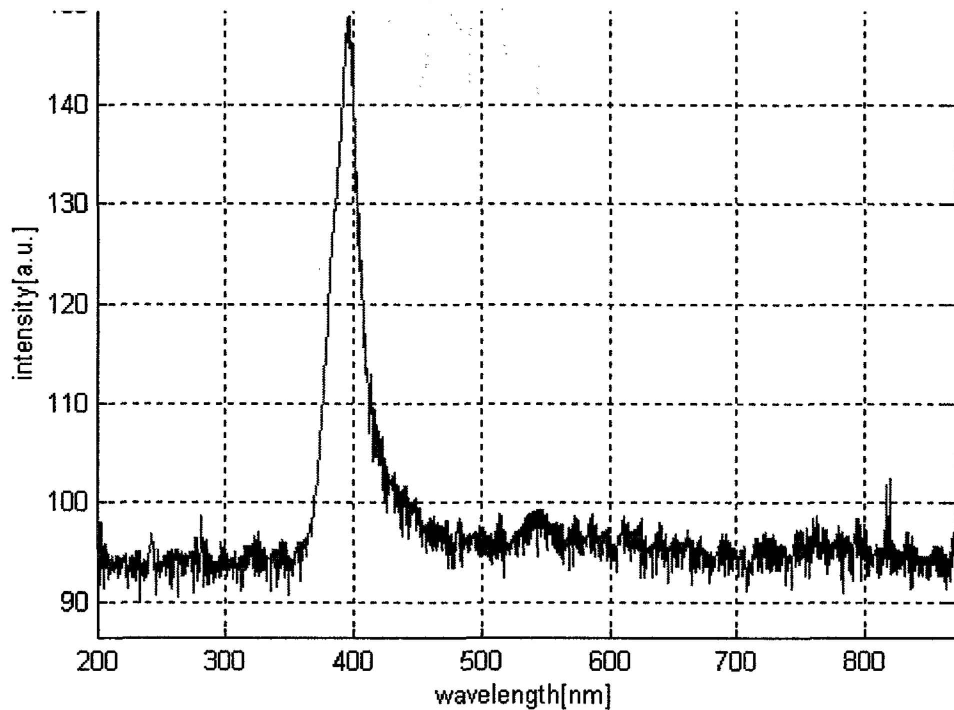


**Figure 3.31.** RT PL spectrum of another portion of PLD 5 sample.



Reproduced with permission of the copyright owner. Further reproduction prohibited without permission.

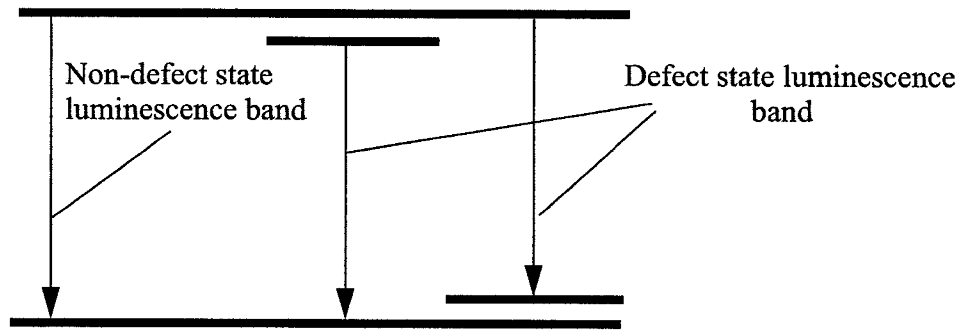


**Figure 3.32.** Depiction of the effects of film defects on RT PL spectrum.



Reproduced with permission of the copyright owner. Further reproduction prohibited without permission.

# CHAPTER 4 *ZnO Films by Sol-gel*

Sol-gel films were developed on Si, $Si/SiO_2$ and Si/ZnO substrates. The $Si/SiO_2$ substrate fabricated by thermal oxidation of Si wafers; the $SiO_2$ thickness was approximately 3 $\mu$m. Si/ZnO substrates were fabricated by depositing ZnO using the PLD process.

## *4.1. Background on Sol-gel*

The beginnings of sol-gel material deposition can be tracked to research done by Geffcken in 1939 when he patented a method of coating large panes of windows for the Schott glass company in Germany. Over the years, the research grew to more than 50,000 papers published worldwide by the 1990s[52].

The name of sol-gel process comes from the transition of a system from liquid or "colloidal sol" to solid "gel" form. The process allows for fabrication of materials with a large variety of properties, from ultra-fine powders, ceramics, glasses, membranes, thin film coatings, to aerogels[52].



Reproduced with permission of the copyright owner. Further reproduction prohibited without permission.

The sol-gel technique has been used in a wide range of fields from dental, biomedical, agrochemical, electronics, energy, space, sensors to separation technologies. However, the largest application of sol-gel is in production of thin films[53].

In sol-gel chemistry, the liquid phase is made up of solid particles suspended in a liquid. Typically, the solution undergoes a series of hydrolysis and polymerization reactions that will cause the formation of colloidal suspension. Subsequently, the particles are condensed on a substrate (by spin casting, for example) to form a gel with solid macromolecules immersed in a solvent[52]. The precursor for the preparation of the colloid consists of a metalloid or metal element surrounded by various appendages or ligands. The most widely used class of precursors in sol-gel research are alkoxides, which are organic compounds[54]. For example, a common precursor for producing zinc oxide is zinc acetate-2-methoxyethanol-monoethanolamine (MEA)[11]. This class of precursors is formed by removing a proton from the hydroxyl or from an alcohol. Table 4.1 shows commonly used alkoxy ligands. There are some problems with using MEA solution as a precursor. Preparation of a stable sol is a tedious process and reagents of metal alkoxides are very expensive. Additionally, for production of ZnO for example, dimethyl zinc and diethyl zinc are so reactive that there exists a danger they might explode in air. One solution is to use metal salt such as acetate or nitrate of metal instead of metal alkoxide. Zinc acetate dihydrate is inexpensive, easy to handle, and has been used widely in CVD, spray pyrolysis, and some atomic epitaxy methods[55].



Reproduced with permission of the copyright owner. Further reproduction prohibited without permission.

| *Alkyl* | | *Alkoxy* | |
|---|---|---|---|
| methyl | $\bullet CH_3$ | methoxy | $\bullet OCH_3$ |
| ethyl | $\bullet CH_2CH_3$ | ethoxy | $\bullet OCH_2CH_3$ |
| *n*-propyl | $\bullet CH_2CH_2CH_3$ | *n*-propoxy | $\bullet O(CH_2)_2CH_3$ |
| *iso*-propyl | $H_3C(\bullet C)HCH_3$ | *iso*-propoxy | $H_3C(\bullet O)CHCH_3$ |
| *n*-butyl | $\bullet CH_2(CH_2)_2CH_3$ | *n*-butoxy | $\bullet O(CH_2)_3CH_3$ |
| *sec*-butyl | $H_3C(\bullet C)HCH_2CH_3$ | *sec*-butoxy | $H_3C(\bullet O)CHCH_2CH_3$ |
| *iso*-butyl | $\bullet CH_2CH(CH_3)_2$ | *iso*-butoxy | $\bullet OCH_2CH(CH_3)_2$ |
| *tert*-butyl | $\bullet C(CH_3)_3$ | *tert*-butoxy | $\bullet OC(CH_3)_3$ |
| *Other* | | | |
| acetylacetonate | $H_3COC(\bullet O)CH_2(O\bullet)COCH_3$ | | |
| acetate | $\bullet OOCCH_3$ | | |

acetylacetonate:

```
 H        H        H
HC—O—C—C—C—O—CH
 H      |  H  |     H
        O     O
        •     •
```

acetate:

```
 H
HC—C—O•
 H  ‖
    O
```

**Table 4.1.** Commonly used ligands for sol-gel synthesis. Dot indicates bonding site, parenthesis indicate atom with available bond, n indicates linear chain, sec - secondary, tert - tertiary[54].

Typical film growth is shown in Fig. 4.1. The process starts with a clean substrate onto which sol is spin-coated and dried. After application of the desired number of coats, the film is annealed at higher temperature. For the process used in our research, the film was dried at 120$\circ$ C on a hot plate and annealed at 600$\circ$ C in oxygen atmosphere in an oven[56].



Reproduced with permission of the copyright owner. Further reproduction prohibited without permission.

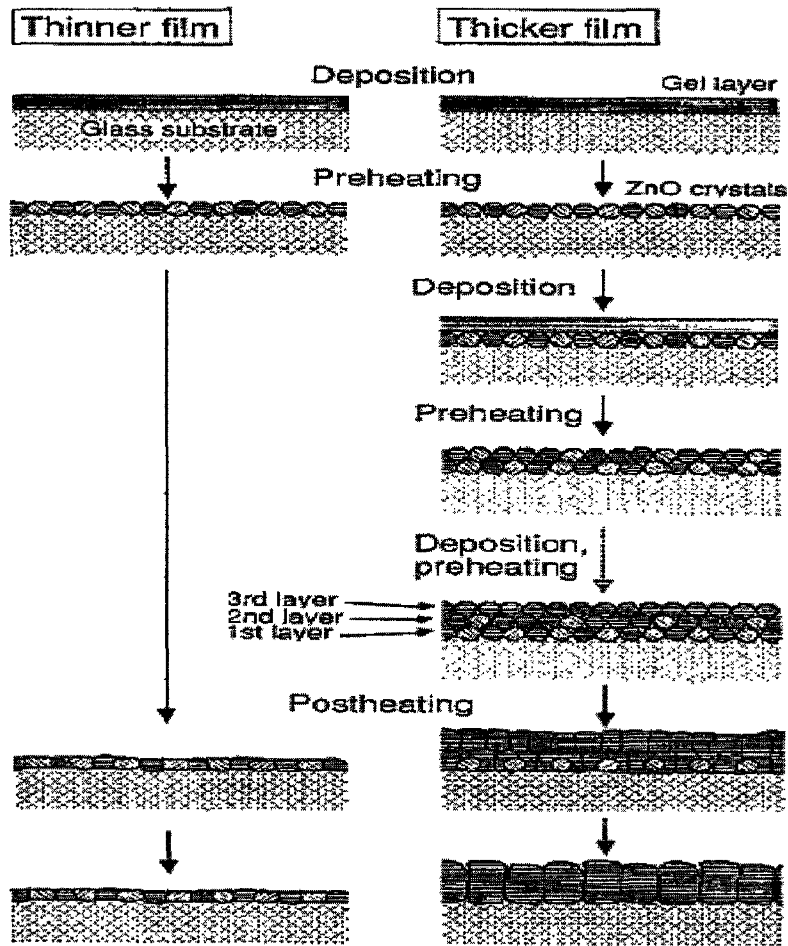


**Figure 4.1.** Typical schematic illustration of ZnO crystal growth in thinner and thicker coating films[11].

There are three processes that take place during the drying and subsequent baking of the film after the final coat of sol is applied: the vaporization of the solvents, the decomposition of the zinc acetate, and the crystallization of the zinc oxide. When the film undergoes all three processes at the same time, there is reduced chance that it will be structurally relaxed. This results in a disturbance of unidirectional crystal growth. This occurs when drying is done at temperatures in excess of 300° C[11]. When the drying occurs at lower temperatures, the gel has more time to relax structurally, resulting in the growth of denser



Reproduced with permission of the copyright owner. Further reproduction prohibited without permission.

ceramic films[11]. The postheating treatment serves a similar role as the post deposition annealing step in pulsed laser deposition, which was discussed in Chapter 3.

## *4.2. ZnO films deposited using sol-gel method.*

The basic recipe for the deposition of ZnO sol-gel films comes from experiments done by Zhang et al.[56] using aqueous sol prepared with 1.1 g of zinc acetate dihydrate, $Zn(C_2H_3O_2){\cdot}2H_2O)$ (ZAD), 1.5 g of polyvinyl alcohol (PVA) with molecular weight of 50,000-85,000, and 40 ml of de-ionized water[56]. This will be termed as the 'standard' recipe in the discussion below. These researchers used multiple spin coatings applied at 3000 rpm with 2 minutes dry time on a hot plate at 120° C in between each layer deposition and final annealing at 600° C in a furnace. Our approach was to explore recipes that used different ratios of PVA (molecular weight of 85,000 - 124,000) and zinc acetate dihydrate, different number of layers at different spinning speeds, various annealing methods and temperatures, as well as deposition on different substrates. A summary of sol-gel films produced in this work is shown in Table 4.2.

All films were dried on a hot plate at 120° C for 10 minutes after each layer was deposited. In some steps, as indicated in the discussion to follow, the samples were annealed after each layer in addition to drying. In most cases each sample was also annealed after the final sol layer. This will also be indicated when discussing each sample.

| **Film** | **Substrate** | **Sol** | **# of Layers** | **Spin speed** | **Anneal Between Sol Spins** | **600° C Final Annealed** | **Thickness** | **n** |
|---|---|---|---|---|---|---|---|---|
| Sol-gel 1 | Si | 1 | 1 | 1000 rpm | no | hot plate | 98 nm | N/A |
| Sol-gel 2 | Si | 1 | 2 | 1000 rpm | no | hot plate | 100 nm | N/A |
| Sol-gel 3 | Si | 1 | 6 | 1000 rpm | no | furnace | 48 nm | N/A |
| Sol-gel 4-1 | Si | 1 | 6 | 1000 rpm | no | no | 80 nm | N/A |
| Sol-gel 4-2 | Si | 1 | 6 | 1000 rpm | no | hot plate | 80 nm | N/A |
| Sol-gel 4-3 | Si | 1 | 6 | 1000 rpm | no | furnace | 80 nm | N/A |



Reproduced with permission of the copyright owner. Further reproduction prohibited without permission.

| Film | Substrate | Sol | # of Layers | Spin speed | Anneal Between Sol Spins | 600° C Final Annealed | Thickness | n |
|---|---|---|---|---|---|---|---|---|
| Sol-gel 5-1 | Si | 1 | 6 | 3000 rpm | no | no | 40 nm | N/A |
| Sol-gel 5-2 | Si | 1 | 6 | 3000 rpm | no | hot plate | 40 nm | N/A |
| Sol-gel 5-3 | Si | 1 | 6 | 3000 rpm | no | furnace | 40 nm | N/A |
| Sol-gel 6-1 | Si | 2 | 1 | 1000 rpm | furnace | furnace | 274 nm | 1.56 |
| Sol-gel 6-2 | Si | 2 | 2 | 1000 rpm | furnace | furnace | 800 nm | 1.56 |
| Sol-gel 6-3 | Si | 2 | 3 | 1000 rpm | furnace | furnace | unknown | N/A |
| PLD 6-1 | Si | 4 | 1 | 1000 rpm | no | furnace | 176 nm | 1.95 |
| PLD 6-2 | Si | 3 | 1 | 1000 rpm | no | furnace | 175 nm | 2.002 |
| Sol-gel 7-1 | Si | 3 | 1 | 1000 rpm | no | furnace | 80 nm | N/A |
| Sol-gel 7-2 | Si | 3 | 3 | 1000 rpm | no | furnace | 40 nm | N/A |
| Sol-gel 8 | Si/$SiO_2$ | 2 | 1 | 1000 rpm | no | furnace | 666 nm | 1.61 |

**Table 4.2.** Summary of sol-gel deposited. '1' in "Sol" column refers to the 'standard' ratio of PVA and zinc acetate dihydrate used as per Zhang *et al.*, '2' to double ratios of PVA and zinc acetate dihydrate while keeping amount of distilled water the same as in '1'. '3' refers to recipes where amount of PVA in the solution was adjusted to reflect the fact that PVA used for work in this thesis was of higher molecular weight than that used by Zhang *et al.*[56] '4' refers to even further reduction of PVA concentration as per suggestions from Dr. Zhang. Under column "Annealed Between Sol Spins" and "Final Annealed", hot plate refers to annealing done on the same hot plate as drying in between layer applications, furnace to the air furnace that was used to anneal PLD films.

The first three sol-gel films were developed in order to study the feasibility of multiple layer applications. Sol-gels 1-3 were deposited using the 'standard' recipe provided by Zhang *et al.* as described above. Sol-gel 1 film was a single layer resulting in a thickness of about 98 nm, as shown in Fig. 4.2. Sol-gel 2 was deposited with 2 layers of sol, but the thickness was just over 110 nm, as shown in Fig. 4.3. These two films were annealed on the hot plate, after the final layer, at 550° C for 30 min and 60 min, respectively. When 6 layers of sol were deposited in Sol-gel 3, the layers dissolved into each other forming film that was much thinner than a single layer deposition. The surface morphology of the first two films was very similar to each other, as shown in Fig. 4.4. The photoluminescence peak for both sol-gel 1 and sol-gel 2 was located near 390 nm, as shown for Sol-gel 2 in Fig. 4.5.



Reproduced with permission of the copyright owner. Further reproduction prohibited without permission.

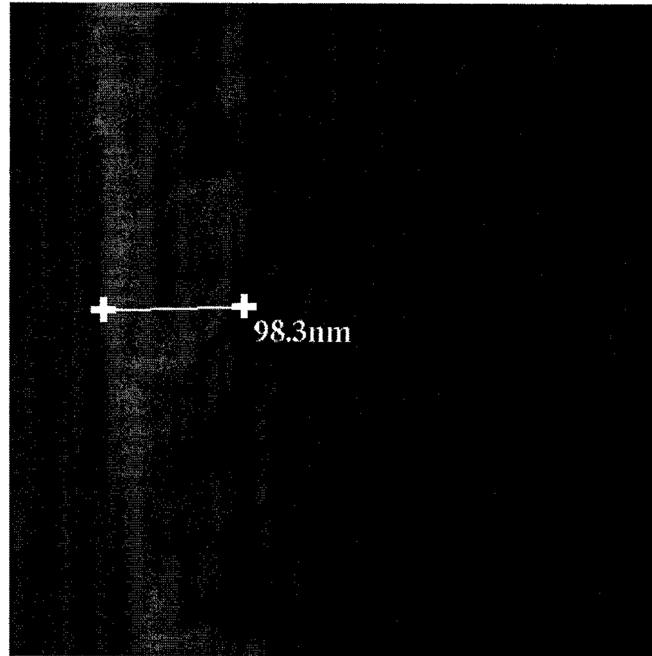


**Figure 4.2.** Edge SEM of sol-gel 1.

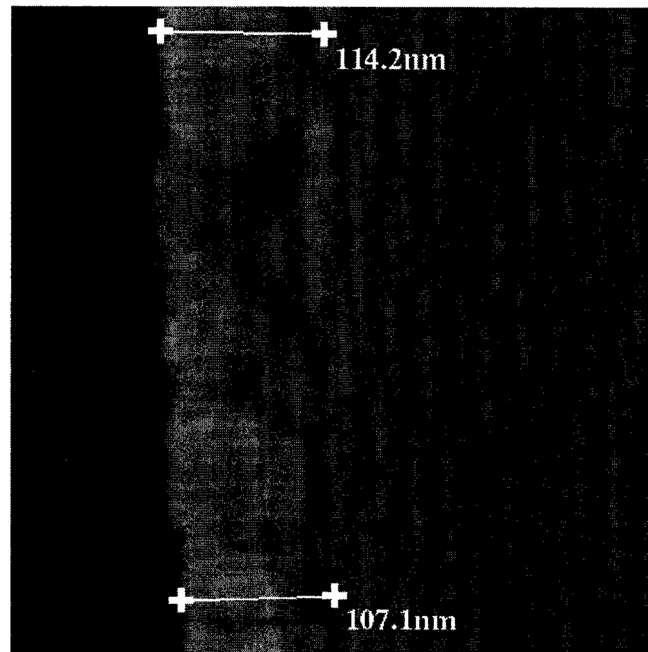


**Figure 4.3.** Edge SEM of sol-gel 2.



Reproduced with permission of the copyright owner. Further reproduction prohibited without permission.

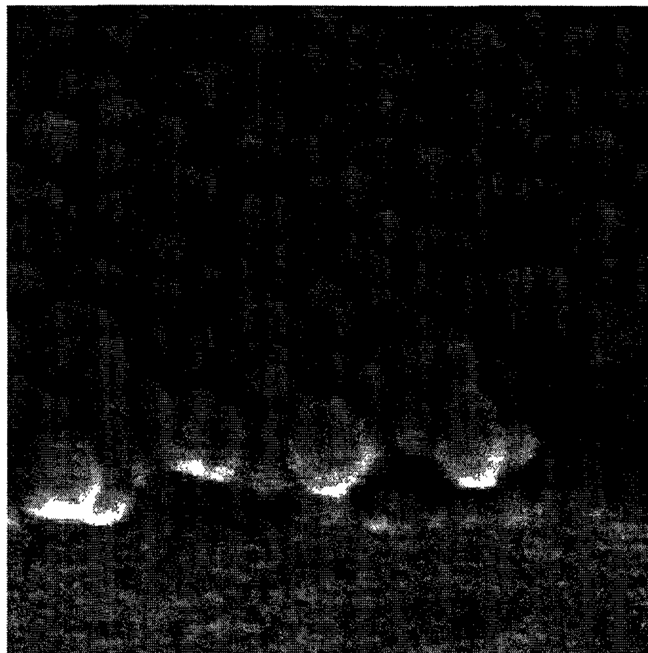

**Figure 4.4.** Angle SEM image of sol-gel 2.

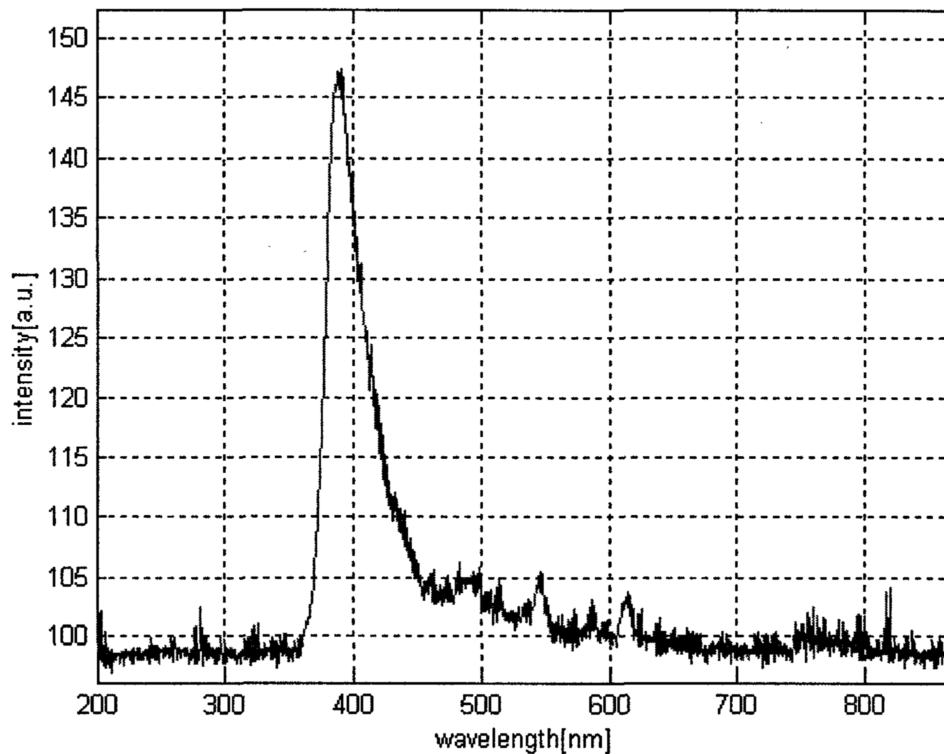


**Figure 4.5.** RT PL spectrum of sol-gel 2 with very distinct peak at about 390 nm.



Reproduced with permission of the copyright owner. Further reproduction prohibited without permission.

There is a distinguishable boundary visible in Fig. 4.3, apparently demarking the boundary between the two spin steps. This image seems to indicate that the material from the first spin step was mostly washed away during the second spin step. This would explain why the double spun film (sol-gel 2) were only slightly thicker than the single-spun film (sol-gel 1). This hypothesis was supported by similar results for a 6-spin deposition that was subsequently attempted. All samples annealed on the hot plate showed very similar results as far as crystal sizes visible on the SEM images and photoluminescence peak location.

These first samples were too thin to provide any conclusive measurements of index of refraction using the prism coupler technique.

The next set of film depositions, sol-gel 4 and sol-gel 5, were performed to shed more light on the effects of the two annealing methods that were used (i.e. hot plate and furnace). They were also intended to confirm the results from the previous depositions regarding multiple layers of sol. As above, a 10 minute bake on the hot plate was applied in between each of the sol depositions. Sol-gel 4 layers were spun at 1000 rpm, whereas sol-gel 5 layers were spun at 3000 rpm. Each of the wafers was then diced into 3 samples. One sample was annealed on the hot plate at 550° C for 90 minutes, one sample was annealed at 600° C for 30 minutes in the furnace, and one sample was not annealed. The results of a 6 layer deposition is shown in Fig. 4.6 for sol-gel 4 and in Fig. 4.7 for sol-gel 5. Both films were about 80 nm thick and there were no significant differences between the film deposited at 1000 rpm and that deposited at 3000 rpm. As in the previous depositions, each sol deposition presumably washed away most of the ZnO material from the previous sol deposition. There was no difference in film morphology for the two different annealing methods. However, some differences were observed in photoluminescence measurements. Annealed samples were very similar to sol-gel 1-2 with a main peak at 390 nm, as shown in Fig. 4.8 and Fig. 4.9. The non-annealed samples have more pronounced peaks in the green band at 505 nm, as shown in Fig. 4.10. This was also observed by Yang-Wen for PLD deposited films that were not annealed[8]. The peaks at 505 nm can be attributed to defects, which are related to deep level emissions such as Zn interstitials



Reproduced with permission of the copyright owner. Further reproduction prohibited without permission.

and oxygen vacancies[8]. Once again, the films produced in these depositions were too thin to perform measurements of refractive index with prism coupler setup.

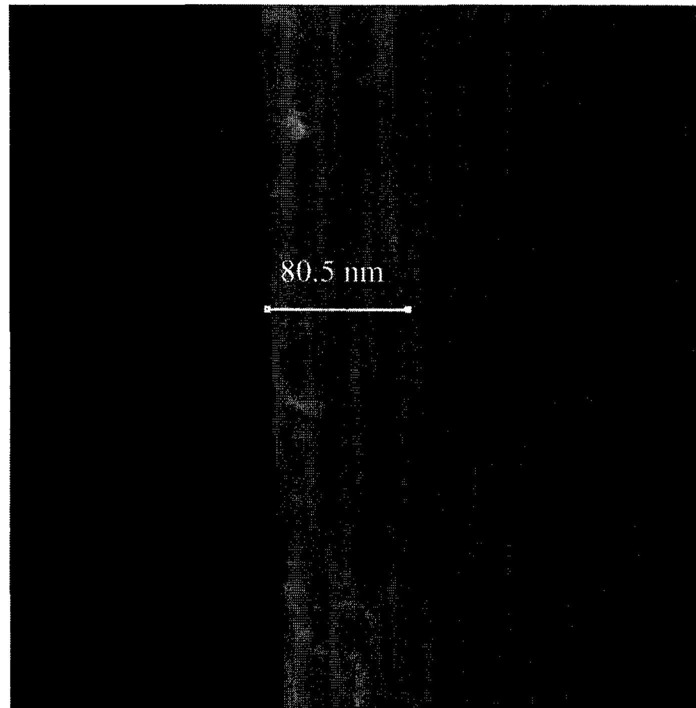


**Figure 4.6.** Edge SEM image of sol-gel 4 sample annealed in a furnace.



Reproduced with permission of the copyright owner. Further reproduction prohibited without permission.

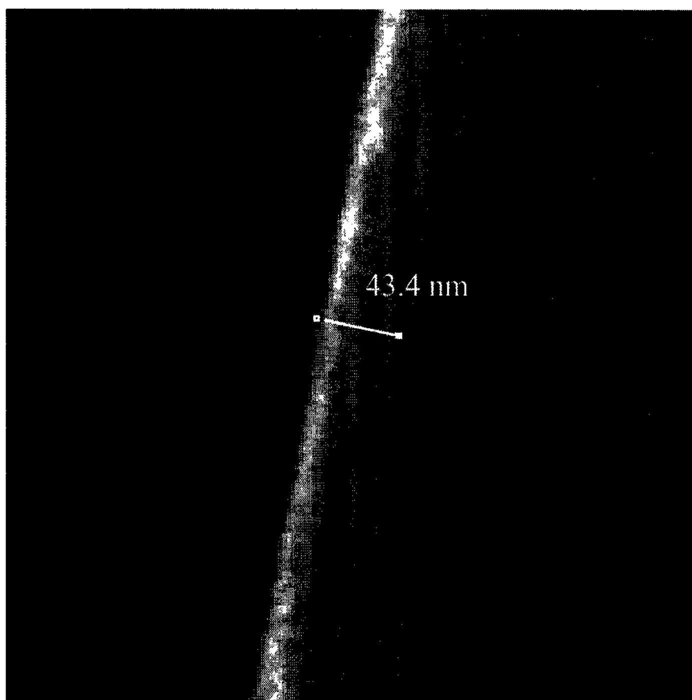


**Figure 4.7.** Edge SEM image of sol-gel 5 sample annealed in a furnace.

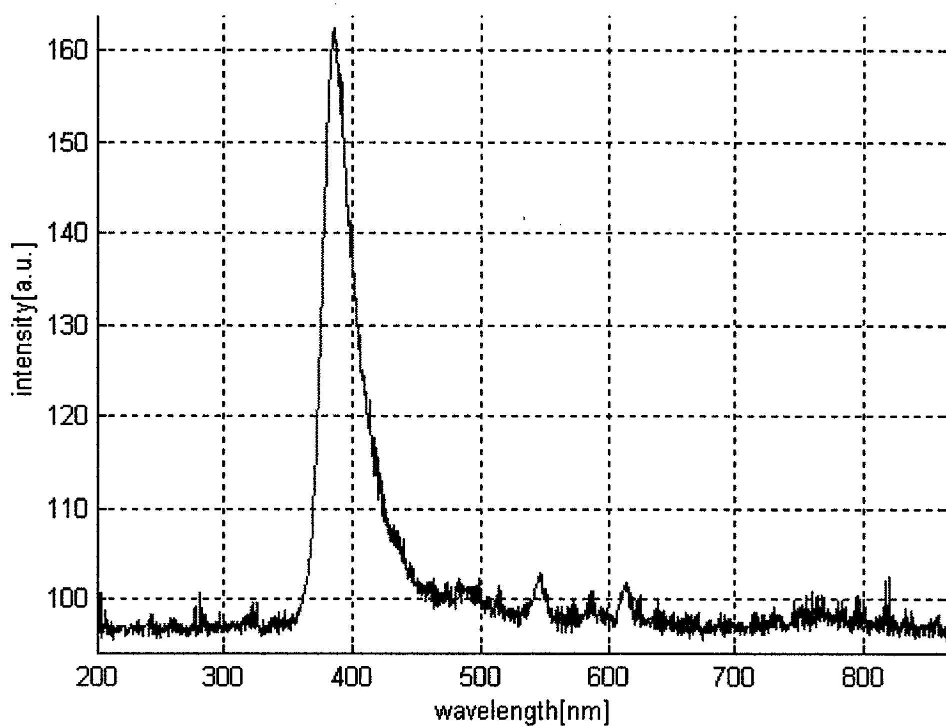


**Figure 4.8.** RT PL spectrum for sol-gel 4-2.



Reproduced with permission of the copyright owner. Further reproduction prohibited without permission.

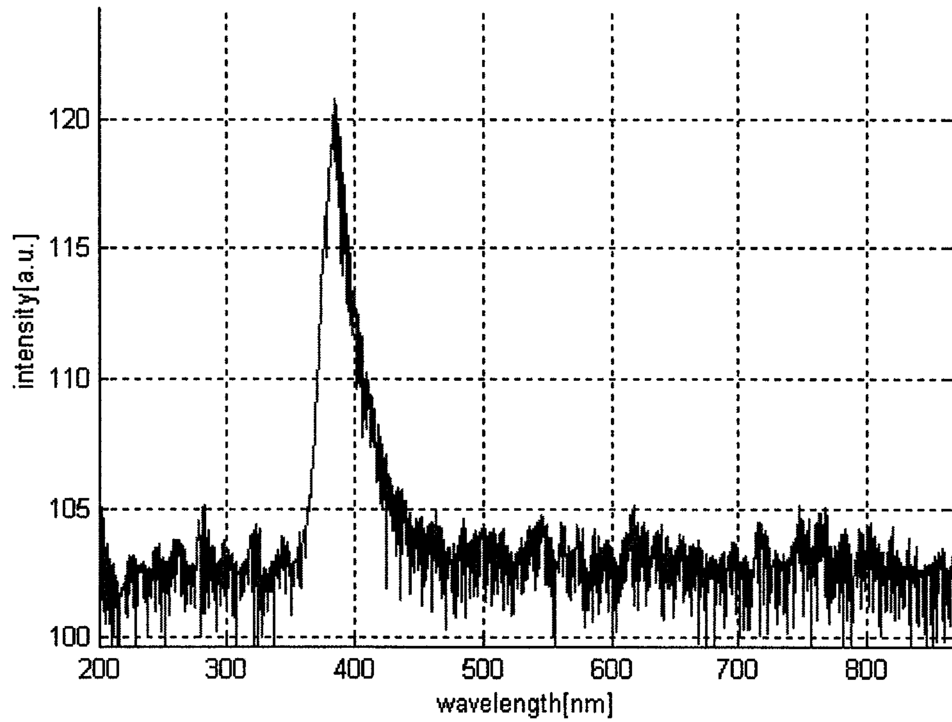


**Figure 4.9.** RT PL spectrum of sol-gel 5-2.

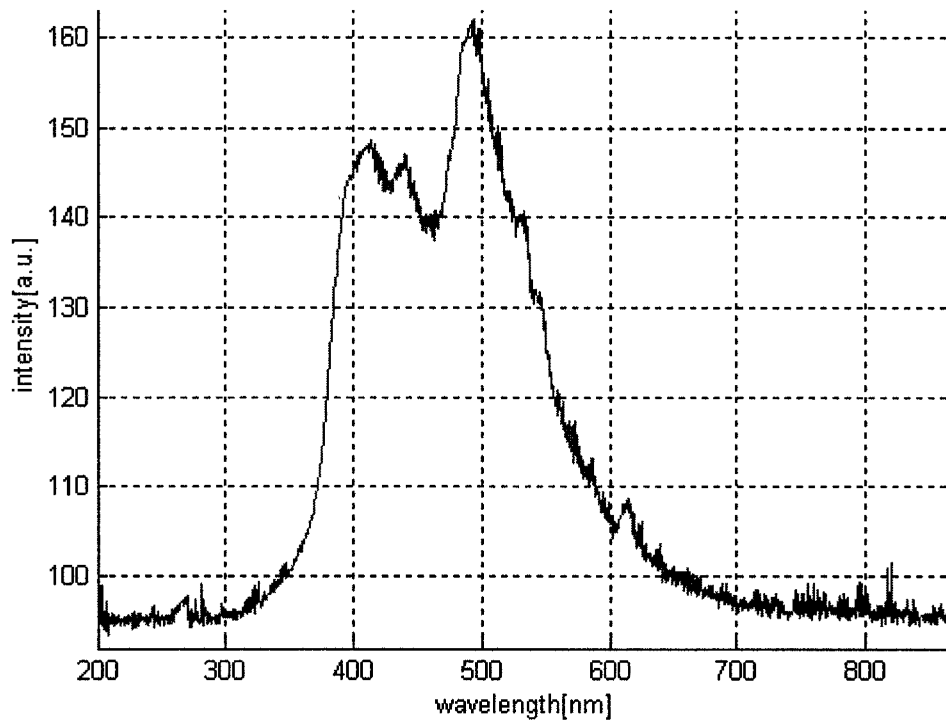


**Figure 4.10.** RT PL spectrum of sol-gel 4-1 with visible additional luminescence peaks.



Reproduced with permission of the copyright owner. Further reproduction prohibited without permission.

Lessons from the previously described depositions led to two preliminary conclusions:

1. With baking the samples on a hot plate for 10 minutes at 120° C in between the depositions, it is not possible to obtain a thick film by repeated spinning of the sol.

2. To increase the thickness of the films, it might be necessary to increase the concentration of PVA and/or ZAD while keeping the volume of water the same as in the recipe referred to as 'standard' in Table 4.2 and described in the beginning of this section.

Sol-gel 6 films were prepared to test both of these preliminary conclusions, by doubling the concentration of PVA and ZAD and varying the baking procedure between sol spin steps. Sol-gel 6-1 was deposited at 1000 rpm, baked on the hot plate at 120° C For 10 minutes and then annealed in a furnace for 30 minutes at 600° C. The sample was then cleaved into 3 smaller samples, and the sol deposition process was repeated on two of the samples (sol-gel 6-2 samples). Both of the sol-gel 6-2 samples were annealed again in the furnace at 600° C for 30 minutes and one sample from this deposition was used as a base for a third sol deposition (sol-gel 6-3). Sol-gel 6-1 and 6-2 resulted in films of good visual quality. However, sol-gel 6-3 cracked and peeled in the last annealing step, most likely due to the stresses created between the film and substrate (i.e. the film would have been well over a micron thick, judging from the results for both sol-gel 6-1 and sol-gel 6-2). Film thickness for sol-gel 6-1 was approximately 274 nm, as shown in Fig. 4.11. Film thickness for sol-gel 6-2 was approximately 800 nm, as shown in Fig. 4.12. The surface of the film was very similar to previous sol-gel depositions, but the film apparently has more air voids. This would explain why both films showed an index of refraction of about 1.56, much lower than the value of approximately 2 expected for bulk ZnO.

The photoluminescence results were consistent with the previously described results for annealed films, with a peak at about 390 nm for both sol-gel 6-1 and 6-2. PL result for sol-gel 6-1 is shown in Fig. 4.13. The PL result for sol-gel 6-2 was almost identical to that of sol-gel 6-1.



Reproduced with permission of the copyright owner. Further reproduction prohibited without permission.

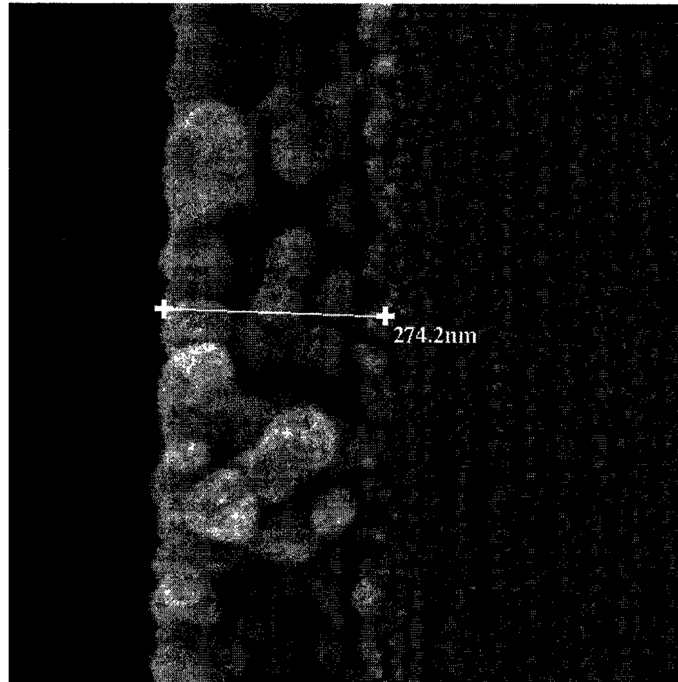


**Figure 4.11.** Edge SEM image of sol-gel 6-1.

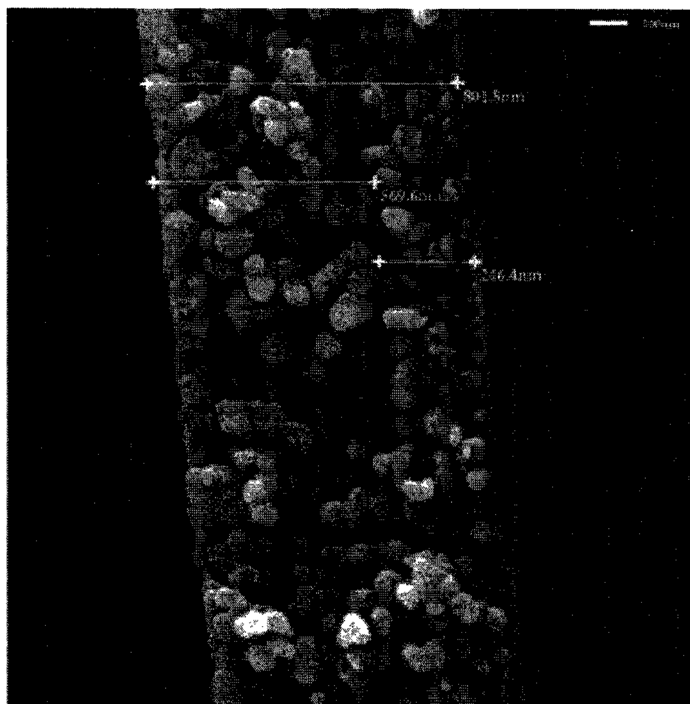

**Figure 4.12.** Edge SEM image of sol-gel 6-2 with distinct boundary between the two layers associated with the 2 sol spinning steps.



Reproduced with permission of the copyright owner. Further reproduction prohibited without permission.

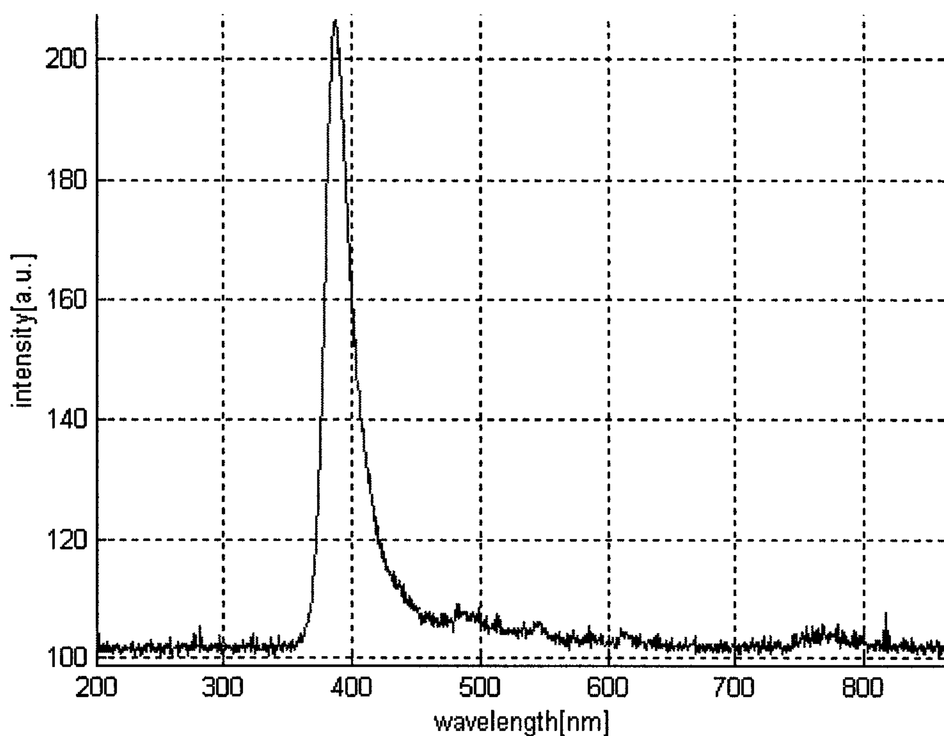


**Figure 4.13.** RT PL spectrum of sol-gel 6-1.

For the subsequent sol-gel deposition, a ZnO seed layer was first grown on a Si substrate by PLD. The seed layer was deposited under the conditions described in previous chapter for 25 minutes, and then annealed at 600° C in a furnace for 2 hrs prior to sol-gel deposition. The PLD sample was diced in 2 pieces. As mentioned, the PVA used by Zhang *et al.*[57] was of a lower molecular weight than the one used in our research. Taking this into account, PLD 6-2 was deposited with a sol recipe comprising 2.2g of ZAD, 2.11g of PVA, and 80 ml of distilled water. Sample PLD 6-1 was deposited using sol with concentrations corresponding to the following recipe: 5.26g of ZAD, 0.24g of PVA, and 80ml of distilled water[58]. The deposition conditions for this batch of films was the same as for the previous batch: only single layer of sol was spun at 1000 rpm for 30 seconds, and the samples were annealed in the furnace at 600° C for 30 minutes. Both substrates had 1 layer of sol deposited on them. Both samples yielded similar film thicknesses, surface morphology, and photoluminescence spectra. PLD 6-1 SEM images are shown in Fig. 4.14 and Fig. 4.15, and its photoluminescence spectrum as shown in Fig. 4.16.



Reproduced with permission of the copyright owner. Further reproduction prohibited without permission.

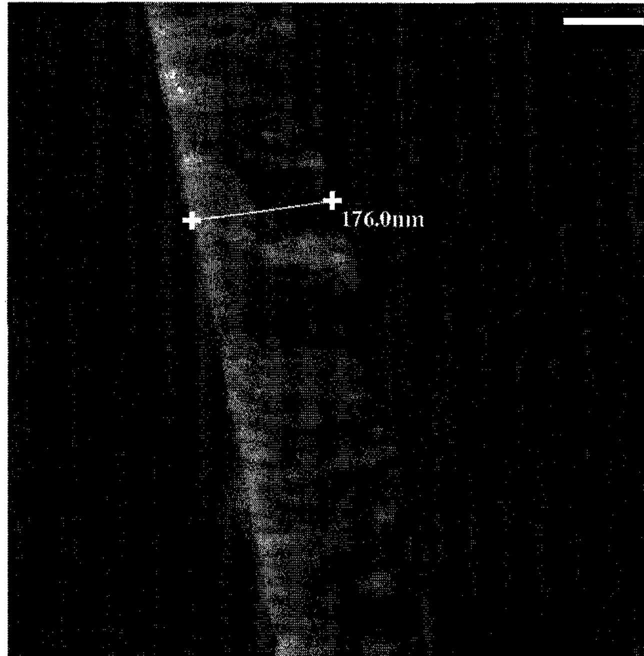


**Figure 4.14.** Edge SEM image of PLD 6-1.

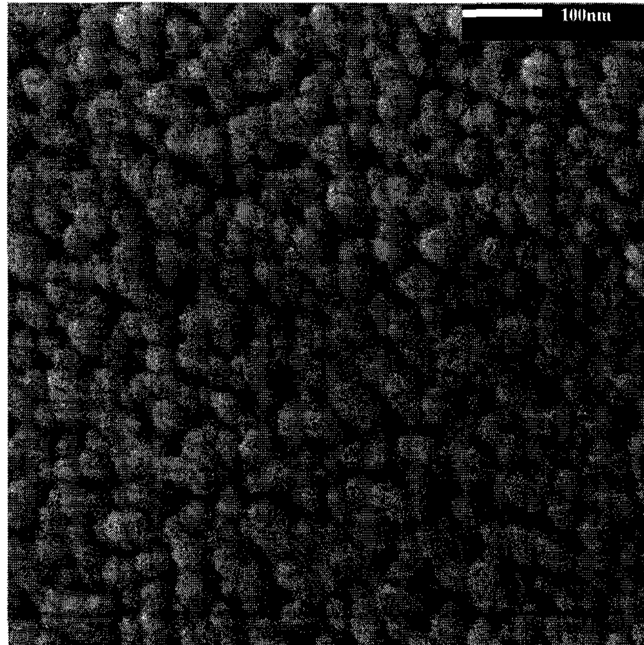


**Figure 4.15.** Top SEM surface image of PLD 6-1.



Reproduced with permission of the copyright owner. Further reproduction prohibited without permission.

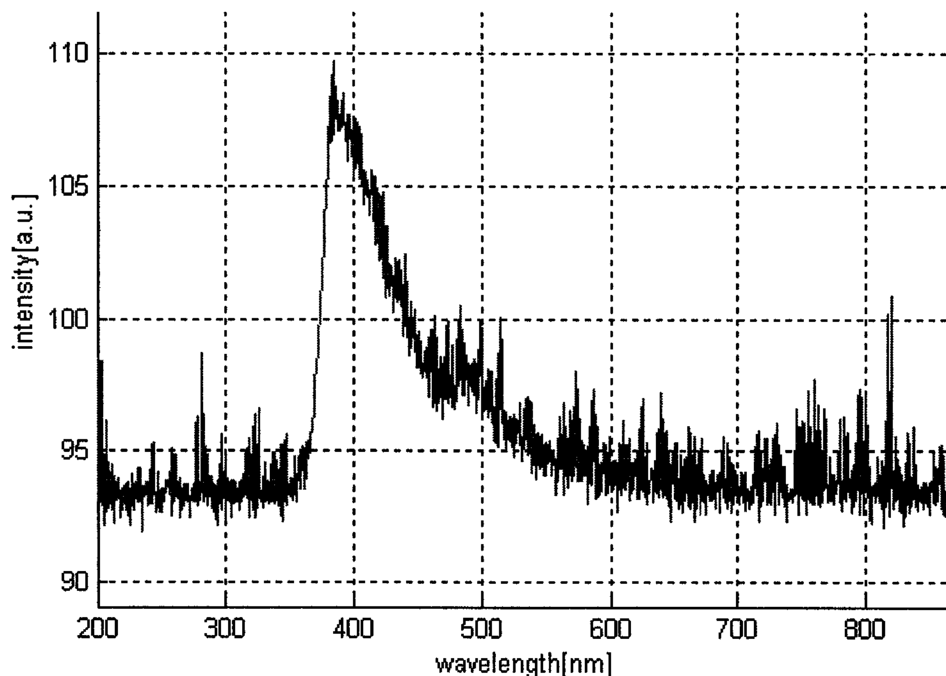


**Figure 4.16.** RT PL spectrum of PLD 6-1.

Films produced in these experiments (with the PLD seed layer) were visually much more dense than the films produced using double concentration sol depositions. Partial confirmation of the film density came from the prism coupler measurements of the index of refraction and thickness measurements. PLD 6-1 was estimated to have approximately an index of 1.95 with thickness of 192 nm. The seed films produced using the PLD method had large variation of thickness throughout the film surface, so the discrepancy between the SEM and prism coupler thickness estimates can be attributed to the thickness variation of the initial substrate that sol was laid on. PLD 6-2 had an index of refraction value of approximately 2 with thickness of 175 nm; this thickness was in good agreement with the estimate from an SEM image. Furthermore, the value of n in this case was in good agreement with the value for bulk ZnO. Further reduction of the PVA concentration in PLD 6-1 didn't result in films of increased density than those obtained in PLD 6-2 and even PLD 6-2 didn't yield films that were much denser than those obtained using 'standard' recipe.

Given the results from the depositions of sol-gel 5 and PLD 6, single concentration sol ('standard' recipe) yielded good quality, dense films with optical constants similar to bulk



Reproduced with permission of the copyright owner. Further reproduction prohibited without permission.

ZnO values. Furthermore, photoluminescence yields were comparable with those for thick, double concentration porous films. Learning from that experience, the next attempt was to produce and characterize films using single concentration sol (but with adjusted amounts of PVA to account for difference in concentration in PVA discussed above) and deposition of multiple layers of sol to form thicker films. Films produced in sol-gel 7-1 and 7-2 were deposited using the same concentration as PLD 6-2, i.e. 2.11g of PVA and 2.2g of ZAD for 80ml amount of distilled water. Sol-gel 7-1 was deposited with 1 layer of sol, sol-gel 7-2 was deposited with 3 layers of sol. Drying between layer deposition was done on a hot plate at 120° C for 10 minutes and each of the films was annealed in a furnace after the deposition. Sol-gel 7-1 acted as a control sample to ensure the deposition yielded the same results for single layer depositions as in the previous experiments.

Sol-gel 7-1 behaved much like the other single layer depositions (both with initial concentrations and the adjusted PVA amounts) yielding a film approximately 80nm thick. Sol-gel 7-2 was about 40nm thick as seen in Fig. 4.17. This multi-layer film was thinner than single layer film. Possible explanation is as in the case of other multiple layer films that were deposited in sol-gel 4 and sol-gel 5, the layers morphed into each other since there was no annealing step between each layer application as opposed to the films in sol-gel 6, where each of the substrates was annealed after each layer application. Surface morphology was very similar to that of the other single layer deposition experiments, as shown in Fig. 4.18. Both samples had a similar photoluminescence reading with peak at about 380 nm, as shown in Fig. 4.19 for sol-gel 7-2. Prism coupler results were inconclusive, due to the insufficient thickness of the films.



Reproduced with permission of the copyright owner. Further reproduction prohibited without permission.

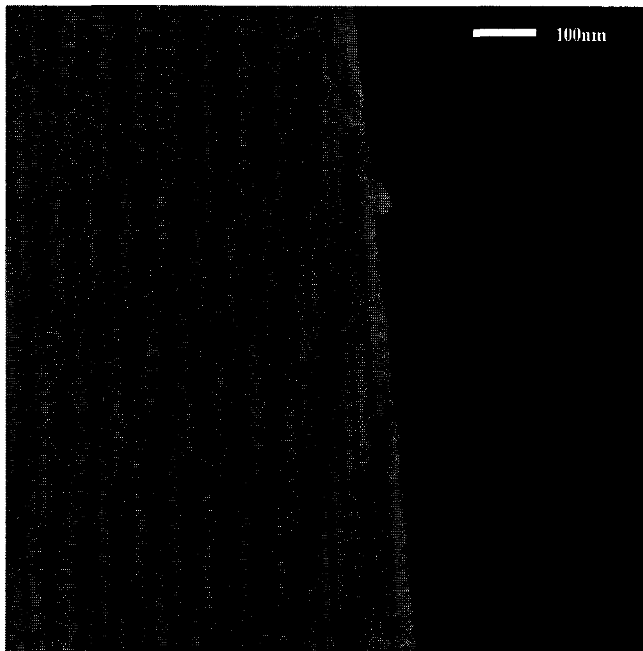


**Figure 4.17.** Edge SEM image of sol-gel 7-2.

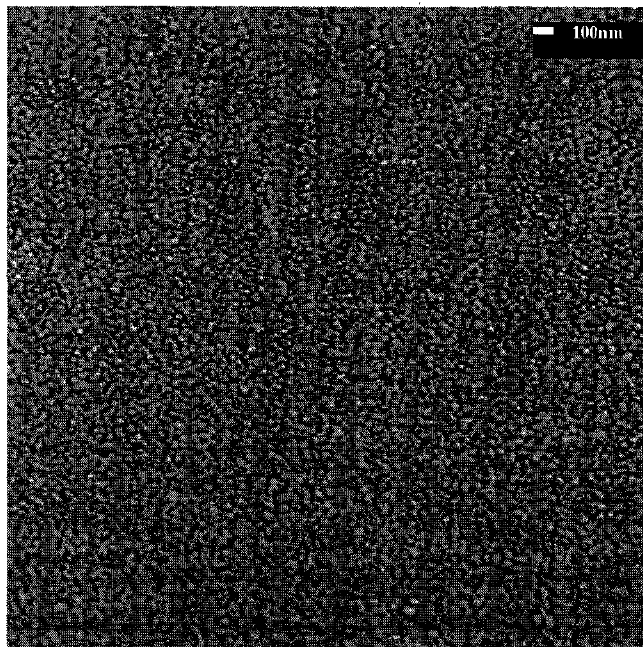


**Figure 4.18.** Top SEM image of the surface of sol-gel 7-2.



Reproduced with permission of the copyright owner. Further reproduction prohibited without permission.

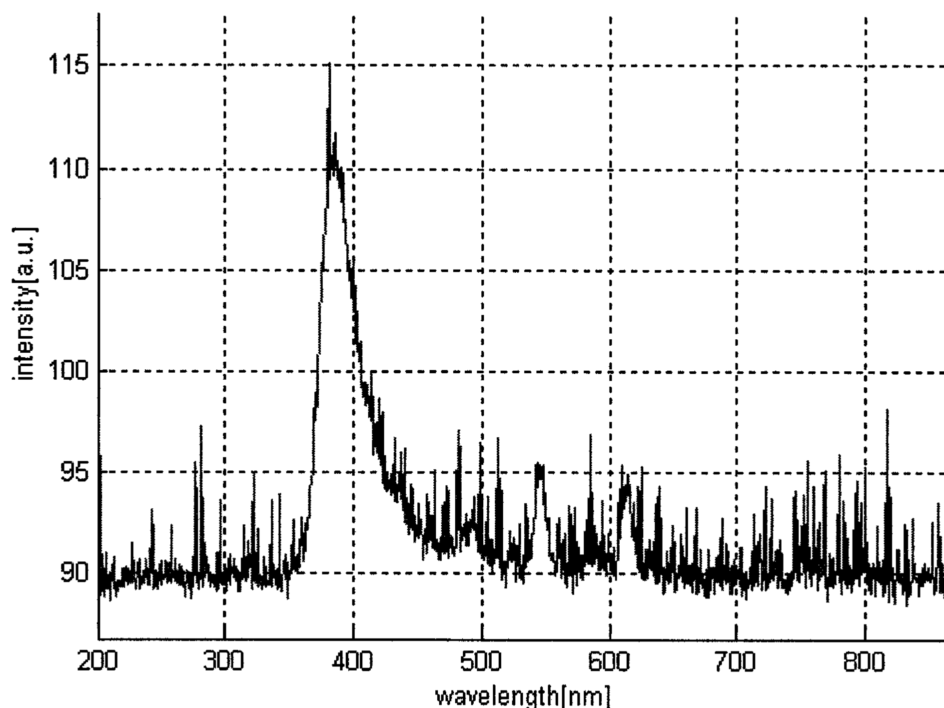


**Figure 4.19.** RT PL spectrum of sol-gel 7-2.

The final experiment performed was a deposition similar to the experiment in PLD 6. In this case, a substrate composed of $Si/SiO_2$ with a 3 $\mu$m layer of $SiO_2$ was used as a base for sol-gel deposition. The concentration of sol used was double the 'standard' recipe (much like in sol-gel 6), as were the deposition details including spin speed (1000 rpm) and annealing method and temperature (30 minutes on a hot plate at 560° C). The resulting film was very similar to that of sol-gel 6; the film was thick (~ 600 nm) and very porous as visible in Fig. 4.20 and Fig. 4.21. The photoluminescence was similar to that for thick films deposited previously, with peak around 380nm as shown in Fig. 4.22. The prism coupler measurement indicated an index of refraction of 1.61, which is in agreement with earlier results for sol-gel depositions with doubled PVA concentration. Presumably the lower index is due to increased porosity of the resulting film.



Reproduced with permission of the copyright owner. Further reproduction prohibited without permission.

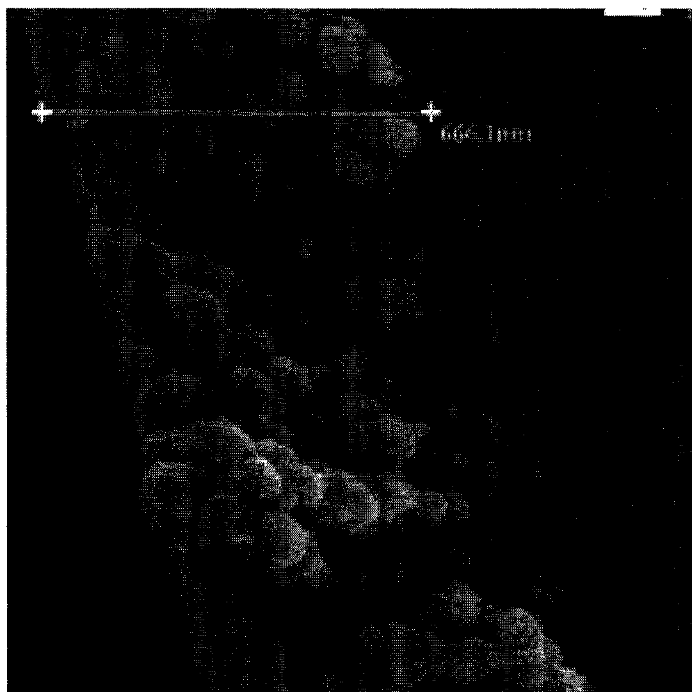

**Figure 4.20.** Edge SEM image of sol-gel 8.

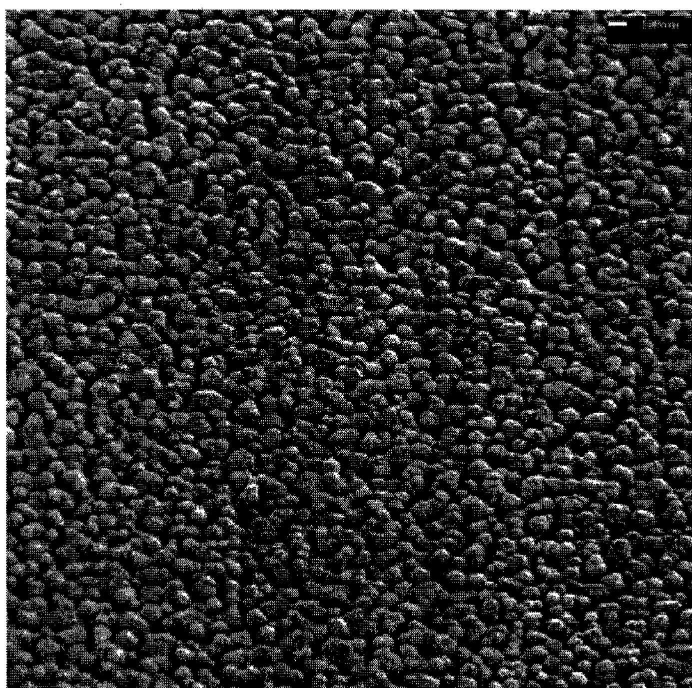

**Figure 4.21.** Surface SEM image of sol-gel 8.



Reproduced with permission of the copyright owner. Further reproduction prohibited without permission.

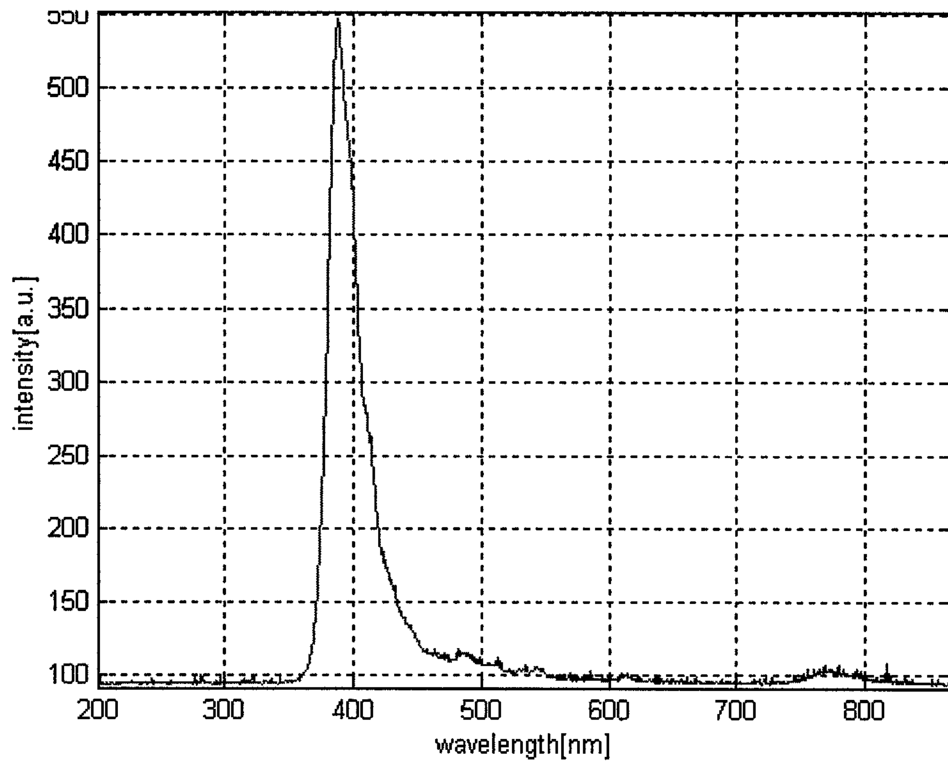


**Figure 4.22.** RT PL spectrum of sol-gel 8.



Reproduced with permission of the copyright owner. Further reproduction prohibited without permission.

CHAPTER 5

# Summary, Conclusion, and Future Work

Two fabrication methods were studied in search of a quality ZnO thin film deposition method with applications to acousto-optic devices in the integrated optics field. Approximately 1 $\mu m$ thick c-axis oriented films were fabricated using pulsed laser deposition in $O_2$ background atmosphere and also using sol-gel technique. Both methods produced films with strong UV emissions after annealing in air. Variations in film morphology, thickness, and optical constants were studied for both pulsed laser deposited and sol-gel deposited films. An initial attempt at a SAW IDT filter device built on a well known and characterized substrate (quartz) was also studied.

The SAW filter had some inadequacies when compared to a commercially available device (shift in operating frequency due to fabrication tolerances and lower signal to noise characteristics).

*PLD deposited films*

PLD films were deposited in a 66mTorr $O_2$ background atmosphere, using 248 nm wavelength, 15 ns pulses at 20 Hz repetition rate from a KrF laser. Two deposition schemes were investigated, one favouring faster film growth and the other favouring better thickness uniformity. Some of the PLD films were annealed at 600° C for 2 hrs in an air-atmosphere furnace.



Reproduced with permission of the copyright owner. Further reproduction prohibited without permission.

All films that were annealed showed strong UV emission in the 390 nm band. Some of the films had an additional band in the red end of the spectrum, most likely arising from film defects.

PLD films were deposited on both fused silica and silicon substrates. As far as the properties that were measured as part of this thesis work, there was no visible change from one type of substrate to another.

*Sol-gel deposited films*

Sol-gel films were deposited using a sol prepared with zinc acetate dihydrate, polyvinyl alcohol and distilled water; the sol was spun at different speeds and resulting films were annealed using different methods.

All sol-gel films were annealed in air. Films were either annealed at 600$^\circ$C for 120 minutes in the furnace or on the hot plate at 560$^\circ$C for 120 minutes. All films that were annealed (using any of the methods described) showed strong UV emission in the 390 nm band. The non-annealed samples of sol-gel deposited films showed additional bands of emission due to film defects such as oxygen vacancies and zinc interstitials.

Sol-gel depositions were done initially using sols comprising 1.1 g of zinc acetate dihydrate, 1.5 g of polyvinyl alcohol, and 40 ml of distilled water. Depositions were also done using double amounts of both PVA and ZAD while keeping the same amount of water, and final depositions were done with lower concentration of PVA. Single concentration films were very similar to those fabricated using the PLD method, with respect to surface morphology, emission spectra, and index of refraction. Double concentration films produced films that were much thicker, but much more porous and with an index of refraction much lower than that of bulk material. However, they had similar emission spectra as for the single concentration films. The films produced with adjusted PVA concentrations had very similar characteristics to the depositions made with single concentration sols.



Reproduced with permission of the copyright owner. Further reproduction prohibited without permission.

Sol-gel films were deposited on silicon, Si/$SiO_2$, and Si/ZnO (deposited by PLD) substrates. All films showed similar characteristics as far as surface morphology, optical constant measurements, and photoluminescence emission spectra.

Sol-gel films of single and multiple sol layers were deposited. Single layer films had similar properties to the films produced by the PLD method. When only the drying process between sol spins was done on the hot plate for 10 minutes at 120° C, the multiple spin depositions produced very thin films. When the same multi-layer films were annealed for 30 minutes using either hot plate or furnace between each sol spin in addition to drying, the additional layers adhered to the previous layer instead of washing them out and the overall result was a much thicker ZnO film.

The spin speed had little effect on the film deposition. Initial spin speed was 1000 rpm, but it was increased in some depositions to 3000 rpm. Both methods yielded films with similar morphology, thickness, optical constants, and emission spectra.

*Future work*

Further studies are required for more complete understanding of methods for producing ZnO thin films. The candidate for an optimal recipe for obtaining a thick, dense, and optically good quality film would involve a standard concentration of ZAD and PVA, i.e. 1.1 g of ZAD, 1.5 g of PVA, and 40 ml of distilled water deposited at 1000 rpm, dried at 120° C on the hot plate. Each subsequent layer, in addition to being dried, would be annealed in a furnace for 30 minutes at 600° C or on the hot plate for 30 minutes at 560° C. The same annealing method, but for 2 hrs, should be utilized after a final layer of sol is deposited and dried. A suitable substrate would be either Si or Si/ZnO combination prepared by PLD.

In the long term, the characteristics of the films produced will be very useful in applications for both acousto-optic applications in the integrated optics field and in production of gas sensors based on porous metal oxide films produced by both PLD and sol-gel. These applications are currently being pursued by both Dr. DeCorby's and Dr. Tsui's groups.



Reproduced with permission of the copyright owner. Further reproduction prohibited without permission.

# *References*

[1] S.J. Pearton, D.P. Norton, K.Ip, Y.W. Heo, T. Steiner, Elsevier 2003, "Recent Progress In Processing and Properties of ZnO," pp. 1-30.
[2] B. Kim, D. Hwang, C. Cho, N. Park, G. Y. Sung, Seong-ju Park, "Electrical and Optical Properties of Silicon Quantum Dots Light-emitting Diode by Using Highly Doped ZnO, " 1st IEEE International Conference on Group IV Photonics Proceedings, pp. 80-82.
[3] A.V. Singh, R.M. Mehra, A. Wakahara, A. Yoshida, "Optimization and Characterization of Highly Conductive and Transparent Al-doped ZnO Films for Solar Cell Applications," Photovoltaic Energy Conversion Conference Records, 2003.
[4] P. Verardi, M. Dinescu, "Characteristics of ZnO Thin Film Transducers Deposited by Pulsed Laser Deposition, " IEEE Ultrasonics Symposium Proceedings, 1995.
[5] C. Baratto, G. Faglia, M. Ferroni, G. Sberveglieri, M.Z. Atashbar, E. Hrehorova, "Investigation on Novel Poly(3-hexylthiophene)-ZnO Nanocomposite Thin Film Gas Sensors, " IEEE Conference on Sensors, 2006.
[6] R.E.I. Schropp, C.E. Matovich, P.K. Bhat, A. Madan, "Transparent and Conductive Thin Films of ZnO for Photovoltaic Applications Prepared by RF Magnetron Sputtering, " J. Vac. Technology. A 15(3), May/June 1997, pp. 1063-1068.
[7] E.S.P. Leong, M.K. Chong, S.F. Yu, K. Pita, "Sol-gel ZnO-SiO/sub2/ Composite Waveguide Ultraviolet Lasers, " IEEE Photonics Technolody Letters, Vol. 16, Issue 11, Nov. 2004, pp. 2418-2420.
[8] S. Yang-Wen, "Dense and Porous ZnO Thin Films Produced by Pulsed Laser Depostition, " University of Alberta 2005.
[9] http://en.wikipedia.org/wiki/Thermochromism
[10] N. Chubachi, "ZnO Films for Surface Acoustic Devices on Nonpiezoelectric Substrates, " Proceedings of the IEEE, Vol. 64, No. 5, May 1976, pp. 772-774.
[11] M. Ohyama, H. Kozuka, T. Yoko, "Sol-gel Preparation of ZnO Films With Extremely Preferred Orientation Along (002) Plane From Zinc Acetate Solution, " Thin Film Solids 306, 1997, pp. 78-85.
[12] http://en.wikipedia.org/wiki/Zincite
[13] http://en.wikipedia.org/wiki/ZnO



Reproduced with permission of the copyright owner. Further reproduction prohibited without permission.

[14] O. Yamazaki, T. Mitsuyu, K. Wasa, "ZnO Thin-Film SAW Devices," IEEE Transactions on Sonics and Ultrasonics, SU-27, 1980, pp. 369-379.
[15] http://en.wikipedia.org/wiki/MOCVD
[16] T. Maruyama, J. Shionoya, "Zinc Oxide Thin Films Prepared by Chemical Vapour Deposition From Zinc Acetate", Journal of Materials Science Letters 11, 1992, pp. 170-172.
[17] J. W. Gardner, V. K. Varadan, O. O. Awadelkarim, "Microsensors, MEMS, and Smart Devices," Wiley 2001.
[18] http://www.geo.uib.no/jordskjelv/index.php?topic=earthquakes&lang=en
[19] http://www.rtxtech.com/product/image/saw%20filter%20_image002.gif
[20] C.Campbell, "Surface Acoustic Wave Devices and Their Signal Processing Applications," Academic Press Inc 1989.
[21] D.P. Morgan, "Surface acoustic wave devices and applications 1. Introductory review," Ultrasonics May 1983, pp.121-131.
[22] W.R. Smith, H.M.Gerard, J.H. Collins, T.M. Reeder, H.J. Shaw, "Design of surface wave delay lines with interdigital transducers," IEEE Trans Microwave Theory and Techniques MTT-17 November 1969, pp. 865-873.
[23] W.R. Smith, H.M.Gerard, J.H. Collins, T.M. Reeder, H.J. Shaw, "Analysis of interdigital surface wave transducers by use of an equivalent circuit model," IEEE Trans. Microwave and Theory and Techniques MTT-17, No. 11, November 1969 pp. 856-864.
[24] Silicon Valley Microelectronics Inc.
[25] N. W. Emanetoglu, "ZnO and $Mg_xZn_{1-x}O$ Based Multilayer Structures for Tunable Surface Acoustic Wave Devices," Graduate School-New Brunswick Rutgers, The State University of New Jersey, May 2003.
[26] M. Kadota, C. Kondoh, "Influence of Step-like Portions on the Surface of ZnO/glass SAW filters on Their Frequency Characteristics," IEEE Transactions on Ultrasonics, Ferroelectrics, and Frequency Control, Vol. 44, No. 3, May 1997, pp. 658-665.
[27] P. Osbond, C.M. Beck, C.J. Brierley, M.R. Cox, S.P. Marsh, N.M. Schorrocks, Marconi Materials Technology, Caswell, Towcester, Northants, "The Influence of ZnO and Electrode Thickness on the Performance of Thin Film Bulk Acoustic Wave Resonators,' 1999 IEEE Ultrasonics Symposium, pp. 911-914.
[28] A.L. Nalamwar, M. Epstein, "Immitance Characterization of Acoustic Wave Transducers," Proc. IEEE 60 (1972), p. 336-336.
[29] Y. Chin Lim, R. A. Moore, "Properties of Alternatively Charged Coplanar Parallel Strips by Conformal Mappings," IEEE Transactions on Electron Devices, Vol. ED-15, No. 3, March 1968, pp. 173-180.
[30] W. Hilberg, "From Approximations to Exact Relations for Characteristic Impedances," IEEE Transactions on Microwave Theory and Techniques, Vol. MTT-17, No. 5, May 1969, p. 259-265.
[31] http://snf.stanford.edu/Process/Lithography/liftoff.html
[32] http://www.ggbindustries.com/
[33] Amnon Yariv, Pochi Yeg, "Optical Waves in Crystals," Wiley, 1983.
[34] D. Ciplys, R. Rimeika, "On Definition of Acoustooptic Figure of Merit for Interaction Between Surface Acoustic and Guided Optical Waves," Ultragarsas, 2000, pp. 17-19.



Reproduced with permission of the copyright owner. Further reproduction prohibited without permission.

[35] H. Nishihara, M. Haruna, T. Sugara, "Optical Integrated Circuits, " McGraw-Hill, 1987.
[36] H. Sasaki, K. Tsubouchi, N. Chubachi, N. Mikoshiba, "Photoelastic Effect in Piezoelectric Semiconductor:ZnO, " Journal of Applied Physics, Vol. 47, No. 5, May 1976, pp. 2046-2049.
[37] http://www.uta.edu/optics/research/ellipsometry/ellipsometry.htm
[38] Herzinger et.al. J. Applied Physics, v. 83, p. 3323 (1998).
[39] Y.W. Sun, J. Gospodyn, P. Kursa, J. Sit, R.G. DeCorby, Y.Y. Tsui, "Dense and Porous ZnO Thin Films Produced by Pulsed Laser Deposition, " International Conference on Photo-Excited Process and Applications 2004.
[40] http://www.dur.ac.uk/pmi/facilities/ellipsometry/ellipsometry.htm
[41] http://en.wikipedia.org/wiki/Scanning_electron_microscope
[42] http://probelab.geo.umn.edu/electron_microprobe.html
[43] http://www.metricon.com/basic.htm
[44] Edited by D. B. Chrisey, Graham K. Hubler, "Pulsed Laser Deposition of Thin Films, " Wiley 1994.
[45] http://www.mrl.columbia.edu/ntm/level1/ch05/html/l1c05s05.html
[46] http://www.lightmachinery.com/ATL-excimer-lasers.html
[47] Edited by L. I. Maissel and R. Glang, "Handbook of Thin Film Technology, " McGraw-Hill 1970.
[48] http://www-staff.lboro.ac.uk/~masdk/film_growth.html
[49] http://www.cerac.com/pubs/cmn/cmn10_3.htm
[50] http://www.onr.navy.mil/sci_tech/31/312/ncsr/materials/zno.asp
[51] M.T. Taschuk, Y.W. Sun, Y.Y. Tsui, "Angularly Resolved Photoluminescent Emission from Pulsed-laser Deposited ZnO Films with Different Microstructures, " submitted to Applied Physics A.
[52] http://en.wikipedia.org/wiki/Sol_gel
[53] J. D. Wright, Nico A.J.M. Sommerdijk, Sol-Gel Materials: Chemistry and Applications, " CRC 2000.
[54] C. Jeffrey Brinker, George W. Scherer, "Sol-Gel Science: The Physics and Chemistry of Sol-Gel Processing, " Academic Press, Inc. 1990.
[55] D. Bao, H. Gu, A. Kuang, "Sol-gel Derived c-axis Oriented ZnO Thin Films, " Thin Film Solids 312, 1998, pp. 37-39.
[56] Y. Zhang, B. Lin, X. Sun, Z. Fu, "Strong Ultraviolet Emission and Rectifying Behavior of Nanocrystalline ZnO Films, " Optical Materials 28 (2006), pp. 1192-1196.
[57] Y. Zhang, B. Lin, X. Sun, Z. Fu, "Temperature-dependent Photoluminescence of Nanocrystalline ZnO Thin Films Grown on Si (100) Substrates By The Sol-gel Process, ". Applied Physics Letters 86 (2005).
[58] personal correspondence with Dr. Zhang



Reproduced with permission of the copyright owner. Further reproduction prohibited without permission.